temperature where the particles bind together. The chemistry of hydration involves the production of hydrous calcium silicates and aluminates via the following reactions:

$$2(\text{DCS}) + 4H_2O \longrightarrow 3CaO{\cdot}2SiO_2{\cdot}3H_2O + Ca(OH)_2$$

$$2(\text{TCS}) + 6H_2O \longrightarrow 3CaO{\cdot}2SiO_2{\cdot}3H_2O + 3Ca(OH)_2$$

$$\text{TCAF} + 10H_2O + 2Ca(OH)_2 \longrightarrow 6CaO{\cdot}Al_2O_3{\cdot}Fe_2O_3{\cdot}12H_2O$$

$$\text{TCA} + 12H_2O + Ca(OH)_2 \longrightarrow 3CaO{\cdot}Al_2O_3{\cdot}Ca(OH)_2{\cdot}12H_2O$$

$$\text{TCA} + 26H_2O + 3(CaSO_4{\cdot}2H_2O) \longrightarrow 6CaO{\cdot}Al_2O_3{\cdot}3SO_3{\cdot}32H_2O$$

$$6CaO{\cdot}Al_2O_3{\cdot}3SO_3{\cdot}32H_2O + 2(\text{TCA}) + 4H_2O \longrightarrow 3(4CaO{\cdot}Al_2O_3{\cdot}3SO_3{\cdot}12H_2O)$$

The reagent particles, consisting of the hydrated species, typically have sizes in the range 1 to 50 μm and are bound together (flocculated) by polar bonds. The processes above proceed by ionic reactions in water. Calcium hydroxide [$Ca(OH)_2$] nucleates and grows as crystallites ranging in size from 10 to 500 μm, whereas the hydrated calcium silicate or aluminate forms a porous network of bonded colloidal particles. The porosity is determined by the water-to-cement ratio (w/c). If the porosity exceeds 18%, a connected network of pores percolate and permeates the sample. If it reaches 30%, more than 80% of the pores are interconnected. The behavior is typical of a percolating network. For high w/c ratios, it takes more hydration to close off the pore space. If w/c is sufficiently high ($> 60\%$) the pore space is never closed off by hydration.

The flow (rheology) of cement before hardening is described approximately by the viscoelastic equation

$$\sigma = \sigma_B + \eta_{\text{p1}} \frac{d\varepsilon}{dt}, \tag{W13.4}$$

where σ is the applied stress, ε the strain, η_{p1} the plastic viscosity, and σ_B called the Bingham yield stress. The last two parameters depend sensitively on the microstructure of the cement and increase as finer particles are used. Typical values for η_{p1} are between 0.01 and 1 Pa · s, and for σ_B range between 5 and 50 Pa. To get the cement to flow, the hydrogen bonds must be broken, and this accounts for the term σ_B. Viscoelasticity is also seen to be important in the discussion of polymers in Chapter 14.

The strength of cements and concrete is largely a function of how much contact area there is between the respective particles. This is illustrated in Fig. W13.12, where three packing geometries are compared. Figure W13.12*a* symbolizes a close-packed monodisperse (homogeneous in size) set of spherical grains. Figure W13.12*b* shows that by densifying with smaller particles, a higher contact area may be achieved, thereby strengthening the network. Figure W13.12*c* shows that an improper assortment of sizes can weaken the network.

One of the main limitations of cement is its brittleness. Crack propagation is partially limited by the pores and other flaws in the material. It has been found that by embedding small fibers, crack propagation can be largely arrested and the cement may be toughened considerably.

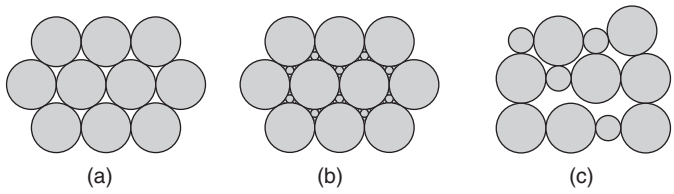

Figure W13.12. Comparison of three packing geometries for spherical particles.

Appendix W13A: Radius Ratios and Polyhedral Coordination

The relationship between the radius ratio and the polyhedral coordination may be derived by examining typical bonding configurations. In Fig. W13A.1 a planar arrangement of four ions is shown. The smaller ion is the cation, with radius r_c, and the larger ion is the anion, with radius r_a. In all cases the cation-to-anion distance will be given by $a = r_c + r_a$, since the cation and anion are in contact. The anion-to-anion distance will be denoted by d. Note that for all cases to be considered, $d \geq 2r_a$, since it is assumed that the anions cannot overlap. From Fig. W13A.1, since the angle between any two a-vectors is 120°, it follows that $d = a\sqrt{3}$. The condition for triangular bonding thus becomes

$$(r_c + r_a)\sqrt{3} \geq 2r_a, \tag{W13A.1}$$

which translates into a lower bound for the radius ratio:

$$R = \frac{r_c}{r_a} \geq \frac{2}{\sqrt{3}} - 1 \approx 0.1547. \tag{W13A.2}$$

For a cation in the center of a tetrahedron, the anion-to-anion distance is given by $d = a\sqrt{8/3}$. Thus the lower bound for tetrahedral coordination is

$$R \geq \sqrt{\frac{3}{2}} - 1 \approx 0.2247. \tag{W13A.3}$$

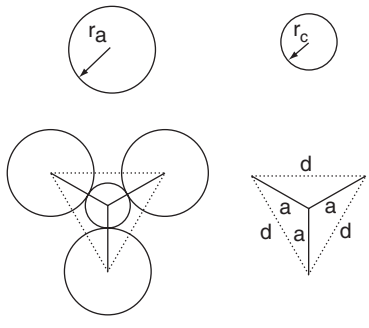

Figure W13A.1. Anions, of radius r_a, surrounding, and in contact with, a cation of radius r_c, forming a planar triangular configuration.

In the sixfold octahedral coordination, $d = a\sqrt{2}$, so it follows that

$$R \geq \sqrt{2} - 1 \approx 0.4142. \tag{W13A.4}$$

In the eightfold cubic coordination, $d = 2a/\sqrt{3}$, so

$$R \geq \sqrt{3} - 1 \approx 0.7321. \tag{W13A.5}$$

REFERENCES

Ternary Phase Diagrams

Hummel, F. A., *Introduction to Phase Equilibria in Ceramics*, Marcel Dekker, New York, 1984.

Silicates

Jaffe, H. W., *Crystal Chemistry and Refractivity*, Dover, Mineola, N.Y., 1996.

Clay

Grimshaw, R. W., *The Chemistry and Physics of Clays and Allied Ceramic Materials*, 4th ed., Wiley-Interscience, New York, 1971.

Cement

Young, Francis, J. ed., Research on cement-based materials, *Mater. Res. Soc. Bull.*, Mar. 1993, p. 33.

PROBLEMS

W13.1 Prove the relations given in Eq. (W13.1) for the ternary phase diagram.

W13.2 Prove the relations given in Eq. (W13.2) for the ternary phase diagram.

W13.3 Referring to Fig. W13.1, prove that $b = c = \frac{1}{2}$ for a material represented by a point midway on the line between components B and C.

W13.4 Referring to Fig. 13.6, show that

$$f_\alpha{:}f_\beta{:}f_\gamma = A(\Delta(O\beta\gamma)){:}A(\Delta(O\gamma\alpha)){:}A(\Delta(O\alpha\beta)),$$

where A is the area of the appropriate triangle.

W13.5 A quaternary phase diagram may be represented as a regular tetrahedron. The four phases are represented by the vertices A, B, C, and D. Show that the composition $A_aB_bC_cD_d$ (with $a + b + c + d = 1$) may be represented by the point O, which is at a perpendicular distance a, b, c, and d from faces BCD, ACD, ABD, and ABC, respectively. Find the length of the edge of the tetrahedron. Can this procedure be generalized to a higher number of components? If so, how?

CHAPTER W14

Polymers

W14.1 Structure of Ideal Linear Polymers

The first quantity characterizing the polymer is the molecular weight. If M_1 is the mass of a monomer unit, the mass of the polymer molecule is

$$M_{N+1} = (N+1)M_1. \tag{W14.1}$$

Often, there will be a distribution of values of N in a macroscopic sample, so there will be a distribution of masses. We return to this point later.

If one were to travel along the polymer from end to end, one would travel a distance Na, where a is the length of a monomer unit. The end-to-end distance in space, however, would be shorter than this, due to the contorted shape of the polymer. The mean-square end-to-end distance $\langle r_N^2 \rangle$ of a polymer with N intermonomer bonds may be calculated. Figure W14.1 shows a chain in which the monomer units are labeled $0, 1, 2, \ldots, N$. One endpoint is at 0 and the other is at N. The vector from monomer 0 to monomer n is denoted by $\mathbf{r}_n$. Thus $\mathbf{r}_0 = \mathbf{0}$, the null vector, whereas $\mathbf{r}_N$ is the end-to-end vector. The vector from monomer m to monomer $m+1$ is denoted by $a\hat{u}_{m+1}$, where $\{\hat{u}_j,\ j = 1, 2, \ldots, N\}$ are a set of unit vectors.

In the ideal polymer it will be assumed that these unit vectors are uncorrelated with each other, so that if an ensemble average were performed,

$$\langle \hat{u}_j \rangle = 0 \quad \text{and} \quad \langle \hat{u}_j \cdot \hat{u}_k \rangle = \delta_{j,k}, \tag{W14.2}$$

where $\delta_{j,k} = 0$ or 1, depending on whether $j \neq k$ or $j = k$, respectively. It follows that

$$\mathbf{r}_N = \sum_{n=1}^{N} a\hat{u}_n, \tag{W14.3}$$

$$r_N^2 = a^2 \sum_{n=1}^{N} \sum_{m=1}^{N} \hat{u}_m \cdot \hat{u}_n. \tag{W14.4}$$

Performing an ensemble average yields

$$\langle \mathbf{r}_N \rangle = 0, \tag{W14.5}$$

$$\langle r_N^2 \rangle = a^2 \sum_{n=1}^{N} \sum_{m=1}^{N} \langle \hat{u}_m \cdot \hat{u}_n \rangle = a^2 \sum_{n=1}^{N} \sum_{m=1}^{N} \delta_{m,n} = a^2 \sum_{n=1}^{N} 1 = Na^2. \tag{W14.6}$$

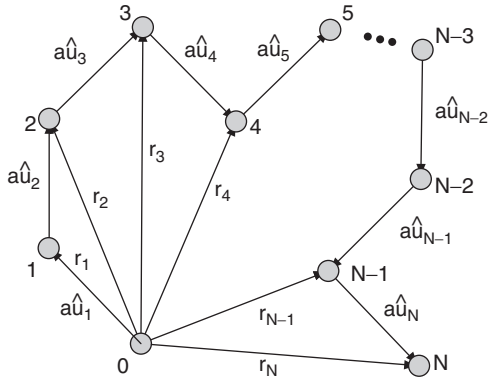

Figure W14.1. Structure of an ideal linear polymer chain.

One may also look at the shadows of the vector $\mathbf{r}_N$ on the yz, xz, and xy planes. Denote these by x_N, y_N, and z_N, respectively. It follows that

$$\langle x_N \rangle = \langle y_N \rangle = \langle z_N \rangle = 0. \tag{W14.7}$$

Due to the isotropy of space, it also follows that the mean-square end-to-end shadow distances (ETESDs) are

$$\langle x_N^2 \rangle = \langle y_N^2 \rangle = \langle z_N^2 \rangle = \tfrac{1}{3}\langle x_N^2 + y_N^2 + z_N^2 \rangle = \tfrac{1}{3}\langle r_N^2 \rangle = \tfrac{1}{3}Na^2. \tag{W14.8}$$

For an ensemble of polymers there will be a distribution of end-to-end distances. This distribution may be found from a simple symmetry argument. Let $F_N(x_N^2)dx_N$ be the probability for finding the ETESD within a bin of size dx_N at $x = x_N$. This may be written as an even function of x_N since there is nothing to distinguish right from left in the problem. The probability for finding the vector $\mathbf{r}_N$ in volume element $dV = dx_N\, dy_N\, dz_N$ is

$$dP = F(x_N^2)F(y_N^2)F(z_N^2)\, dV = G(r_N^2)\, dV, \tag{W14.9}$$

where, by the isotropy of space, dP can depend only on the magnitude of r_N. Here $G_N(r_N^2)\, dV$ gives the probability for finding the end-to-end distance in volume element dV. If the relation above is differentiated with respect to x_N^2, the result is

$$F'(x_N^2)F(y_N^2)F(z_N^2) = G'(r_N^2). \tag{W14.10}$$

Dividing this by

$$F(x_N^2)F(y_N^2)F(z_N^2) = G(r_N^2) \tag{W14.11}$$

results in

$$\frac{F'(x_N^2)}{F(x_N^2)} = \frac{G'(r_N^2)}{G(r_N^2)}. \tag{W14.12}$$

Since r_N may be varied independently of x_N (e.g., by varying y_N), both sides of this equation must be equal to a constant. Call this constant $-\alpha_N$. Integrating the resulting first-order differential equation produces

$$F_N(x_N^2) = A_N e^{-\alpha_N x_N^2}. \tag{W14.13}$$

Since this represents a probability it must be normalized to 1, that is,

$$1 = \int_{-\infty}^{\infty} F_N(x_N^2)\, dx_N = \int_{-\infty}^{\infty} A_N e^{-\alpha_N x_N^2}\, dx_N = A_N \sqrt{\frac{\pi}{\alpha_N}}, \tag{W14.14}$$

so $A_N = (\alpha_N/\pi)^{1/2}$.

Use this probability distribution, F_N, to compute $\langle x_N^2 \rangle$:

$$\langle x_N^2 \rangle = \int_{-\infty}^{\infty} \sqrt{\frac{\alpha_N}{\pi}} x_N^2 e^{-\alpha_N x_N^2}\, dx_N = \frac{1}{2\alpha_N} = \frac{Na^2}{3}, \tag{W14.15}$$

where the last equality follows from Eq. (W14.8). Thus

$$F_N(x_N^2) = \left(\frac{3}{2\pi N a^2}\right)^{1/2} e^{-3x_N^2/2Na^2}, \tag{W14.16}$$

$$G_N(r_N^2) = \left(\frac{3}{2\pi N a^2}\right)^{3/2} e^{-3r_N^2/2Na^2}. \tag{W14.17}$$

A plot of the end-to-end distance probability distribution function as a function of $\rho = r/a\sqrt{N}$ is given in Fig. W14.2. In this graph the volume element has been written as $4\pi r_N^2\, dr_N$. Note that the most probable value of r is $a(2N/3)^{1/2}$, as may be verified by finding the extremum of the curve. This $N^{1/2}$ dependence is characteristic of processes involving a random walk of N steps.

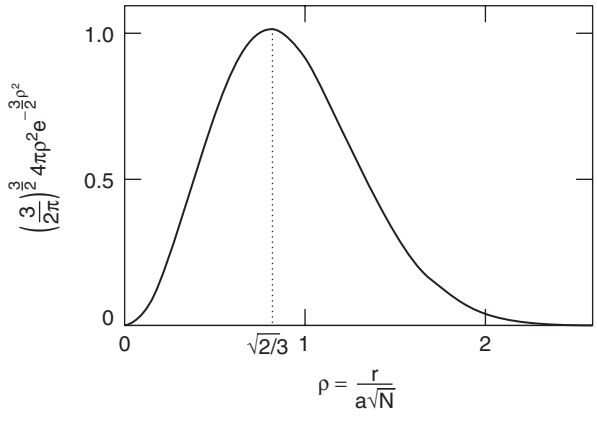

Figure W14.2. End-to-end distance probability distribution $G_N(R_N^2)$ for the ideal linear polymer.

The center of mass of the polymer is defined (approximately, by neglecting end-group corrections) by

$$\mathbf{R} = \frac{1}{N+1}\sum_{n=0}^{N} \mathbf{r}_n. \tag{W14.18}$$

Let $\mathbf{s}_n$ be the location of the nth monomer relative to the center of mass:

$$\mathbf{s}_n = \mathbf{r}_n - \mathbf{R}. \tag{W14.19}$$

Define a quantity s^2 that is the mean square of s_n:

$$s^2 \equiv \frac{1}{N+1}\sum_{n=0}^{N} \langle s_n^2 \rangle. \tag{W14.20}$$

In the polymer literature the parameter s is referred to as the *radius of gyration*, although its definition conflicts with that used in the mechanics of rigid bodies. Thus

$$\sum_{n=0}^{N} \langle s_n^2 \rangle = \sum_{n=0}^{N} \langle (\mathbf{r}_n - \mathbf{R})^2 \rangle = \sum_{n=0}^{N} \langle r_n^2 \rangle - (N+1)\langle R^2 \rangle. \tag{W14.21}$$

Note that

$$\sum_{n=0}^{N} \langle r_n^2 \rangle = \sum_{n=0}^{N} na^2 = \frac{N(N+1)}{2}a^2. \tag{W14.22}$$

Also

$$\langle R^2 \rangle = \left(\frac{1}{N+1}\right)^2 \sum_{m=1}^{N}\sum_{n=1}^{N} \langle \mathbf{r}_n \cdot \mathbf{r}_m \rangle. \tag{W14.23}$$

Note that

$$\langle \mathbf{r_n} \cdot \mathbf{r_m} \rangle = a^2 \sum_{j=1}^{n}\sum_{k=1}^{m} \langle \hat{u}_j \cdot \hat{u}_k \rangle = a^2 \sum_{j=1}^{n}\sum_{k=1}^{m} \delta_{j,k} = a^2 \min(m, n), \tag{W14.24}$$

where $\min(m, n) = m$ when $m < n$, and vice versa. It follows that

$$\langle R^2 \rangle = \frac{1}{(N+1)^2}\sum_{n=1}^{N}\sum_{m=1}^{N} a^2 \min(m, n) = \left(\frac{a}{N+1}\right)^2 \sum_{n=1}^{N}\left(\sum_{m=1}^{n} m + \sum_{m=n+1}^{N} n\right)$$

$$= \left(\frac{1}{N+1}\right)^2 \sum_{n=1}^{N}\left[\frac{n(n+1)}{2} + n(N-n)\right]$$

$$= \left(\frac{a}{N+1}\right)^2 \frac{N}{6}(2N^2 + 3N + 1) = \frac{a^2}{6}\frac{N}{N+1}(2N+1). \tag{W14.25}$$

For large N this approaches

$$\langle R^2 \rangle \approx \frac{Na^2}{3}. \tag{W14.26}$$

By coincidence, this is the same as the expression given in Eq. (W14.15). An expression for the square of the radius of gyration is finally obtained:

$$s^2 = \frac{a^2}{6}\frac{N(N+2)}{N+1} \longrightarrow N\frac{a^2}{6}. \tag{W14.27}$$

It is also possible to obtain a formula for the mean-square distance of a given monomer to the center of mass:

$$\langle s_n^2 \rangle = \langle r_n^2 \rangle - 2\langle \mathbf{R} \cdot \mathbf{r}_n \rangle + \langle R^2 \rangle. \tag{W14.28}$$

Using

$$\langle \mathbf{R} \cdot \mathbf{r}_n \rangle = \frac{a^2}{N+1}\left(\sum_{m=1}^{n} m + \sum_{m=n+1}^{N} n\right) = \frac{a^2}{N+1}\left[-\frac{n^2}{2} + n\left(N + \frac{1}{2}\right)\right] \tag{W14.29}$$

results in

$$\langle s_n^2 \rangle = \frac{N^2a^2}{N+1}\left\{\frac{1}{3}[w^3 + (1-w)^3] + \frac{1}{6N}\right\} \longrightarrow N\frac{a^2}{3}[w^3 + (1-w)^3], \tag{W14.30}$$

where $w = n/N$.

Finally, the symmetry argument employed previously may be used to obtain an expression for the probability distribution function, $P(s_n)$, for the distances s_n. Isotropy of space leads to a Gaussian functional form for P:

$$P(s_n) = Ae^{-\gamma s_n^2}. \tag{W14.31}$$

Using this to evaluate $\langle s_n^2 \rangle$ leads to the expression

$$\langle s_n^2 \rangle = \frac{\int d^3s_n s_n^2 \exp(-\gamma s_n^2)}{\int d^3s_n \exp(-\gamma s_n^2)} = \frac{3}{2\gamma} = N\frac{a^2}{3}\left[\left(\frac{n}{N}\right)^3 + \left(1 - \frac{n}{N}\right)^3\right], \tag{W14.32}$$

so

$$\gamma = \frac{9}{2}\left(\frac{N}{a}\right)^2 \frac{1}{n^3 + (N-n)^3}, \tag{W14.33}$$

$$A = \left(\frac{\gamma}{\pi}\right)^{3/2}. \tag{W14.34}$$

W14.2 Self-Avoiding Walks

There are two constraints that a linear-chain polymer must obey: each monomer must be attached to the previous monomer in the chain, and no monomer can cross another monomer. The case of a single molecule is considered first, followed by a dense collection of molecules. If only the first constraint is imposed, the result has already been derived: the end-to-end distance grows as $\sqrt{N}$, just as in a random walk. It will be seen that the effect of the second constraint is to transform this to $r_N \propto N^{\nu}$, where $\nu = 0.588 \pm 0.001$. The fact that the distance grows as a power of N greater than that for the overlapping chain model is expected. After all, since certain back-bending configurations are omitted because they lead to self-overlap, it is expected that the chain will form a looser, more-spread-out structure. The precise value of the exponent depends on the results of a more detailed calculation.

In Table W14.1, results are presented for a random walk on a simple cubic lattice. For a walk of N steps, starting at the origin, there are 6^N possible paths. The 6 comes from the fact that at each node there are six possible directions to go: north, south, east, west, up, or down. The table presents the number of self-avoiding walks and also the mean end-to-end distance. The exponent may be estimated by a simple argument. At the simplest level ($N = 2$) the effect of nonoverlap is to eliminate one of the six possible directions for the second step (Fig. W14.3). The mean end-to-end distance is therefore $(2 + 4\sqrt{2})/5 = 1.531371\ldots$. For a polymer of length N, imagine that it really consists of two polymers of length $N/2$. These two half-polymers are assumed to combine with the same composition rule as the two one-step segments above did. Assuming the scaling formula $r_N = AN^{\nu}$, one obtains

$$AN^{\nu} = A\left(\frac{N}{2}\right)^{\nu} \frac{2 + 4\sqrt{2}}{5}, \tag{W14.35}$$

which leads to $\nu = 0.6148237\ldots$. Successive refinements of the exponent are obtained by applying the scaling prescription above to the entries in Table W14.1. Acceleration of the convergence of the exponent is obtained by averaging successive values of the exponents.

TABLE W14.1 Self-Avoiding Walks on a Cubic Lattice

Number of Steps N	Number of Possible Paths n (paths)	Number of Self-Avoiding Paths of Length N n (SAW paths)	Mean End-to-End Distance $\langle s \rangle$
1	6	6	1.00000
2	36	30	1.53137
3	216	150	1.90757
4	1,296	726	2.27575
5	7,776	3,534	2.57738
6	46,656	16,926	2.88450
7	279,936	81,390	3.14932
8	1,679,616	387,966	3.42245
9	10,077,696	1,853,886	3.62907
10	60,466,176	8,809,878	3.89778

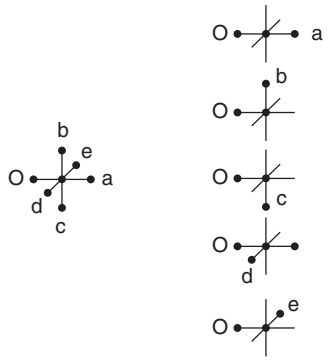

Figure W14.3. A polymer "path" starts at O and after two steps ends up at positions a, b, c, d, or e. Path $O-a$ has length 2; the other paths have length $\sqrt{2}$.

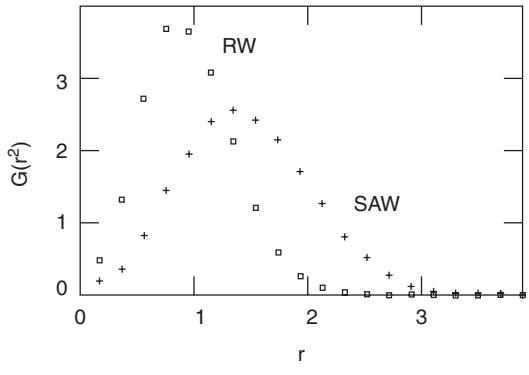

Figure W14.4. Comparison of the end-to-end distance distributions $G(r^2)$ for the random walk (RW) and the self-avoiding walk (SAW). The units are arbitrary.

In Fig. W14.4 the distribution of end-to-end distances for the random walk (RW) is compared to the distribution of distances for the self-avoiding walk (SAW). The curves were generated by constructing a chain of 100 spheres, with each successive sphere touching the previous one at a random location. An ensemble average of 10,000 random chains was made. One verifies that the SAW distribution is more extended than the RW distribution.

Next consider a dense polymer. Each monomer is surrounded by other monomers, some belonging to its own chain and some belonging to others. The no-crossing rule applies to all other monomers. By extending the chain to larger sizes, the chain will avoid itself, but it will more likely overlap other chains. Thus there is nothing to gain by having a more extended structure. The net result is that there is a cancellation effect, and the chain retains the shape of a random walk. Thus in the dense polymer the mean end-to-end distance grows as $\sqrt{N}$.

W14.3 Persistence Length

On a large-enough length scale, a long polymer molecule will look like a random curve. On a short-enough length scale, however, a segment of the polymer may look straight.

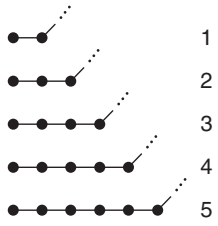

Figure W14.5. Various possible bend locations in a polymer.

The question is at what length scale the transition occurs. The characteristic distance is called the *persistence length*, L_p. A simple statistical argument provides an estimate of this length. Refer to Fig. W14.5 to see the enumeration of bending configurations.

Select a monomer at random and look at its NN and subsequent neighbors down the chain. Let p be the probability that two neighboring bonds are not parallel to each other and $q = 1 - p$ be the probability that they are parallel to each other. The probability of forming a bend after moving one monomer down the chain is $P_1 = p$. The probability of forming the first bend after traversing two bonds is $P_2 = qp$. Similarly, the probability of traversing n bonds before the bend is

$$P_n = q^{n-1}p. \tag{W14.36}$$

Note that the probability is properly normalized, since

$$\sum_{n=1}^{\infty} P_n = \sum_{n=1}^{\infty} (1-p)^{n-1}p = \frac{p}{1-(1-p)} = 1. \tag{W14.37}$$

The mean number of parallel bonds before a bend occurs is

$$\langle n \rangle = \sum_{n=1}^{\infty} P_n n = \frac{p}{q}\sum_{n=1}^{\infty} nq^n = p\frac{\partial}{\partial q}\frac{1}{1-q} = \frac{1}{p}. \tag{W14.38}$$

The persistence length is obtained by multiplying this by the bond length, a:

$$L_p = \frac{a}{p}. \tag{W14.39}$$

Suppose that the bend formation requires an activation energy E_b and that there are g possible ways of making the bend. Then

$$p = \frac{ge^{-\beta E_b}}{1 + ge^{-\beta E_b}} \approx ge^{-\beta E_b}, \tag{W14.40}$$

where it is assumed that $E_b \gg k_B T$. Thus

$$L_p = \frac{a}{g}e^{\beta E_b}. \tag{W14.41}$$

At low temperatures the persistence length of an isolated polymer will be long. At high temperatures L_p becomes shorter. This assumes, of course, that there are no obstacles in the way to prevent coiling and uncoiling of the polymer. In a dense polymer melt, however, the steric hindrance due to the presence of the other molecules prevents this coiling–uncoiling from occurring.

W14.4 Free-Volume Theory

The concept of packing fraction has already been encountered when analyzing crystalline order and the random packing of hard spheres. The same concept carries over to the case of polymers. When the polymer is below the melting temperature, T_m, and is cooled, it contracts by an amount determined by the volume coefficient of thermal expansion, β. Consistent with a given volume there are many possible configurations that a polymer molecule may assume. As the temperature is lowered closer to the glass-transition temperature, T_g, the volume shrinks further and the number of possible configurations is reduced. Concurrent with the decrease of volume and reduction in the number of configurations is a rapid increase in the viscosity of the polymer. These trends may be related by introducing the free-volume theory, or the closely related configurational-entropy approach.

Free volume is defined as the difference in the volume that a sample has and the volume it would have had if all diffusion processes were to cease. Recall that at $T = 0$ K all thermal motion ceases. For low temperatures, atomic vibrational motion occurs, but the atoms retain their mean center-of-mass positions. Below the Kauzmann temperature, T_K, all atoms on a polymer chain are sterically hindered by other atoms and there can be no diffusion of the individual atoms on the polymer chain. At a temperature above the Kauzmann temperature there can be some diffusion of the atoms comprising the polymer, but the polymer as a whole still cannot move, since some of its atoms are pinned by the steric hindrance of other atoms. It is not until a temperature $T_g > T_K$ is reached that the molecule as a whole may begin to move. This motion usually involves the concerted motion of a group of atoms. For the group of atoms to diffuse, there must be a space for it to move into. The free volume is a measure of that space. It is important to distinguish free volume from void space. In both the crystalline state and the random close-packed structure there is void space but no free volume. If PF is the packing fraction, $1 - \text{PF}$ is a measure of that void space. Free volume begins to form when the volume constraint on the system is relaxed and the atoms are permitted some "breathing room." The packing fraction when there is free volume is $f < \text{PF}$. Free volume plays the same role in amorphous polymers as vacancies play in crystals.

Imagine that the polymers are partitioned into molecular groups (i.e., groups of atoms on the polymer chain that are free to diffuse above T_K). It will be assumed that this distribution costs no energy, the partitioning being based just on probabilities. Let V_f be the total free volume available to a system of N such molecular groups. The average free volume per molecular group is

$$v_f = \frac{V_f}{N}. \tag{W14.42}$$

Imagine that the free volume available to a molecular group comes in various sizes, which will be labeled v_i. Let N_i be the number of groups assigned the volume v_i. Then

there are two constraints:

$$\sum_i N_i = N \tag{W14.43}$$

and (neglecting possible overlaps of free volume)

$$\sum_i N_i v_i = V_f. \tag{W14.44}$$

The number of ways to partition N molecular groups into classes with N_1 in the first class, N_2 in the second class, and so on, is given by the multinomial coefficient W:

$$W = \frac{N!}{N_1!\,N_2!\cdots} = \frac{N!}{\prod_i N_i!}. \tag{W14.45}$$

The most probable distribution is sought [i.e., the one with the maximum configurational entropy, $S = k_B \ln(W)$]. This involves maximizing W subject to the two prior constraints. First use Stirling's approximation, $\ln(N!) \approx N\ln(N) - N$, to write

$$\ln(W) = N\ln(N) - N - \sum_i [N_i \ln(N_i) - N_i]. \tag{W14.46}$$

When $\ln(W)$ is maximized with respect to the N_i, W will also be maximized. Introduce Lagrange multipliers γ and λ to maintain these constraints and vary the quantity $\ln(W) - \gamma\left(\sum N_i - N\right) - \lambda\left(\sum N_i v_i - V_f\right)$ with respect to the variables N_i, to obtain

$$\frac{\partial}{\partial N_i}\left\{N\ln(N) - N - \sum_i [N_i \ln(N_i) - N_i] - \gamma\left(\sum_i N_i - N\right)\right.$$
$$\left. -\lambda\left(\sum_i N_i v_i - V_f\right)\right\} = 0, \tag{W14.47}$$

so

$$-\ln(N_i) - \gamma - \lambda v_i = 0. \tag{W14.48}$$

Solving this for the probability of obtaining a given volume yields

$$p_i = \frac{\exp(-\lambda v_i)}{\sum_i \exp(-\lambda v_i)}. \tag{W14.49}$$

The value of λ is fixed by the constraint

$$v_f = \sum_i p_i v_i = -\frac{\partial}{\partial \lambda} \ln \sum_i \exp(-\lambda v_i). \tag{W14.50}$$

A further approximation is called for. Introduce a volume density of states

$$\rho(v) = \sum_i \delta(v - v_i) \tag{W14.51}$$

and write

$$\sum_i \exp(-\lambda v_i) = \int \rho(v) \exp(-\lambda v)\, dv. \tag{W14.52}$$

It will be assumed that the volume density of states may be approximated by a constant, although other possible variations may be imagined. Then

$$\sum_i \exp(-\lambda v_i) = \int_0^\infty \rho_0 \exp(-\lambda v)\, dv = \frac{\rho_0}{\lambda}, \tag{W14.53}$$

and $v_f = 1/\lambda$.

The next assumption involves arguing that motion of a molecular group cannot occur until a minimum amount of free volume, v^*, is assigned to it. The probability for having $v > v^*$ is

$$p^* = \sum_i p_i \Theta(v_i - v^*) = \frac{\displaystyle\int_{v^*}^\infty \rho(v) \exp(-v/v_f)\, dv}{\displaystyle\int_0^\infty \rho(v) \exp\left(-\frac{v}{v_f}\right) dv} = \exp\left(-\frac{v^*}{v_f}\right). \tag{W14.54}$$

Recall from elementary physics that a hole in a solid expands when the solid expands. This concept applies to the free volume as well, so

$$\frac{dv_f}{dT} = \beta(v_f + v_K), \tag{W14.55}$$

where β is the volume thermal-expansion coefficient and v_K is the volume per molecular group at the Kauzmann temperature, T_K. Integrating this, and assuming for simplicity's sake that β is constant, leads to

$$v_f(T) = v_K(e^{\beta(T-T_K)} - 1) \approx v_K \beta (T - T_K), \tag{W14.56}$$

where it is assumed that the exponent is small enough to be linearized. Thus

$$p^* = \exp\left[-\frac{v^*}{v_K \beta (T - T_K)}\right]. \tag{W14.57}$$

By assumption, the viscosity η varies inversely as p^*. Normalize it to the value η_g, the viscosity at temperature T_g:

$$\frac{\eta(T)}{\eta_g} = \exp\left[\frac{v^*}{v_K \beta}\left(\frac{1}{T - T_K} - \frac{1}{T_g - T_K}\right)\right]. \tag{W14.58}$$

This leads to the Williams–Landel–Ferry (WLF) equation

$$\log_{10} \frac{\eta(T)}{\eta_g} = -\frac{C_1(T - T_g)}{C_2 + T - T_g}. \tag{W14.59}$$

Empirically, it is found that $C_1 = 17.4$ and $C_2 = T_g - T_K = 51.6$ K are the average values for many polymers. This means that the glass-transition temperature is on the average about 51.6 K above the Kauzmann temperature. Also, the free volume at the glass-transition temperature amounts to 2.5% of the critical volume for diffusion:

$$v_{f,g} = v_k \beta (T_g - T_K) = \frac{v^*}{C_1} \log_{10} e = 0.025\ v^*. \tag{W14.60}$$

The time–temperature superposition principle presupposes the existence of a universal connection between viscosity and temperature. The WLF formula shows that this supposition is, in fact, warranted. The free-volume theory also predicts that diffusion of gases through the polymer should increase considerably above T_K and should increase further above T_g. It also predicts that the application of pressure, which compresses the material and hence removes free volume, should serve to increase the viscosity. This prediction is consistent with experiment.

One may measure the free volume by relating it to the thermal expansion of the solid. Write the total volume of a sample at temperature T as the sum of three terms, $V(T) = V_p + V_v + V_f$, where V_p is the volume occupied by the polymer atoms, V_v is the void space, and $V_f(T)$ is the free volume. At $T = T_g$, $V_f(T_g) = 0$ and $V(T_g) = V_p + V_v \equiv V_g$. For $T > T_g$, $V(T) = V_g[1 + \beta(T - T_g)]$. Then $V_f(T) = V_g \beta (T - T_g)$. In practice one takes for β the difference in the values of the volume coefficient of thermal expansion above and below T_g.

Note that the distinction between T_K and T_g really exists only for macromolecules such as polymers. For small molecules the movement of individual atoms is tantamount to the motion of the molecule as a whole.

It is now believed that free-volume theory was a useful milestone in the approach to a full understanding of the glass transition but is not the ultimate explanation. Modern advances in what is known as mode-coupling theory provide a more fundamental approach toward this understanding.

W14.5 Polymeric Foams

Foams constructed from polymers offer a variety of uses, including filters, supports for catalysts and enzymes, and possible applications as electrodes in rechargeable batteries. Examples range from polyurethane cushions to polystyrene coffee cups. Here the focus is on one example of such a foam made of cross-linked polystyrene. Most of this material consists of empty space, with the void volume typically occupying more than 90% of the total. There is a fully interconnected network of empty chambers connected by holes whose size can vary between 2 and 100 μm in diameter, with a fairly uniform size distribution (±20%). The density is typically in the range 20 to 250 kg/m^3.

The foam is created by an emulsion technique that combines water, oil (containing styrene), and an emulsifier, followed by vigorous agitatation of the mixture. The emulsifier keeps the small oil droplets formed from recombining into larger droplets. The water droplets can be made to occupy more than the 74% needed to form a close-packed structure of uniform spheres by including additional smaller droplets. The emulsion resembles soap bubbles, but with the air being replaced by water (Fig. W14.6). Persulfates are present as an initiator for the polymerization and divinylbenzene serves as the cross-linker as in the vulcanization process discussed

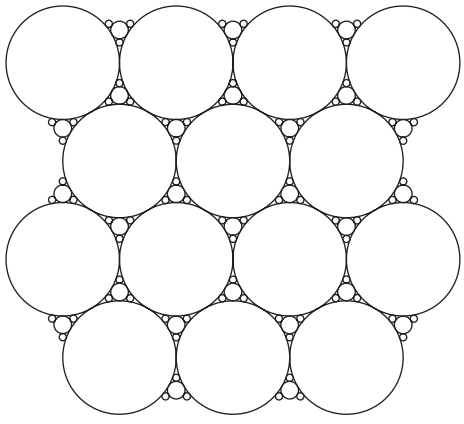

Figure W14.6. Two-dimensional representation of a foam. The region between the circles (spheres) is the portion occupied by the polymer. The spheres are empty.

in Section 14.1. The process of initiation is discussed in Chapter 21 of the textbook.[†] The cross-linked matrix is rigid. Once the polymer foam has formed, there is a need to remove the water and clean out the residual chemicals. The resulting material may be sliced into useful shapes.

Other polymers may be used to create carbon foams. For example, a foam made from polymethacrylonitrile (PMAN) with divinylbenzene serving as the cross-linker may be pyrolyzed to leave behind a carbon shell in the form of the original foam.

Interest has now expanded to low-density microcellular materials (LDMMs) composed of low-atomic-weight elements (e.g., C or Si polymers). They are porous and have uniform cell size, typically in the range 0.1 to 30 μm. They exhibit very low density, and because of the uniform cell size, the mechanical properties are homogeneous. An example is ultralow-density silica gel, which can have a density of 4 kg/m^3 — only three times that of air! These materials are both transparent and structurally self-supporting. They have promising applications as thermal or acoustical insulators.

W14.6 Porous Films

The sports world is enriched by the existence of garments made of breathable microporous films. These materials permit gases such as air and water vapor to pass through them readily while offering protection against water droplets. An example of such a porous film has the brand name Gore-tex, a Teflon-based material. Here the pores are generated by heat-casting a film sheet and stretching it, thereby expanding the preexisting defects until they form a connected network of pores. The pore sizes are typically 0.2 μm long and 0.02 μm wide. Water droplets cannot pass through the network because this would involve greatly expanding the droplets' surface area, and consequently the surface energy. Porosity levels of 40% are achievable.

[†] The material on this home page is supplemental to *The Physics and Chemistry of Materials* by Joel I. Gersten and Frederick W. Smith. Cross-references to material herein are prefixed by a "W"; cross-references to material in the textbook appear without the "W."

Recently, it was found that polypropylene contains two crystalline phases, an α-phase (monoclinic) and a β-phase (hexagonal), in addition to the amorphous phase.[†] The lower-density β-form (see Table 14.1) is less stable than the α-form and has a lower melting temperature. By applying stress to the material, it is possible to transform β to α. When this occurs there is a volume change, and void spaces are produced next to where the converted β-phase was. These voids percolate to form a network of pores. By adding fillers and rubbers into the pores and stretching the material it is possible to enlarge the pores to the optimal size.

Another way of preparing porous films is to irradiate the polymer film with high-energy ions. The ions create radiation damage as they penetrate the material, resulting in the breaking of polymer bonds along their tracks. By etching with acid or base, the damaged regions may be removed, leaving behind pores. Pore diameters as small as 20 nm may be produced by this technique.

W14.7 Electrical Conductivity of Polymers

It has been found experimentally that some polymers possess very high electrical conductivities when doped with small amounts of impurities. The electrical conductivities can approach those of copper [$\sigma_{Cu} = 58.8 \times 10^6 (\Omega \cdot m)^{-1}$ at $T = 295$ K; see Table 7.1]. An example of such a polymer is *trans*-polyacetylene doped with Na or Hg (n-doping) or I (p-doping). Other highly conducting polymers are polypyrrole $(C_4H_2NH)_n$, polythiophene $(C_4H_2S)_n$, polyaniline $(C_6H_4NH)_n$, and TTF-TCNQ (tetrathiafulvalene-tetracyanoquinodimethane). The conductivity tends to be highly anisotropic, with conductivity parallel to the polymer backbone strand being typically 1000 times larger than conductivity perpendicular to the strand. The precise origin of this high conductivity has been the subject of considerable debate.

Observe that strands of polyacetylene make almost perfect one-dimensional solids, with the molecule being typically 100,000 monomers in length. Furthermore, the covalent bonds comprising the polymer are energetically highly stable. Any doping of the sample proceeds by having donors or acceptor ions contribute carriers, without these ions actually entering the strands themselves. Since shielding is absent in a one-dimensional solid, these ions can be expected to interact with whatever mobile carriers may be present in the string via a long-range Coulomb force. As will be seen later, this is ineffective in backscattering the carriers, making the resistance of the polymer very small.

In Fig. W14.7, two bonding configurations are presented for the *trans* state of polyacetylene and also the *cis* configuration. Unlike the case of the benzene molecule, where a resonance structure is formed by taking a linear combination of the two bonding configurations, in long polymers each configuration maintains its distinct character. In benzene, the energy gap between the bonding and antibonding states is sufficiently large that the system relaxes into the bonding state. In polyacetylene the gap is very small. It is known that the carbon–carbon bond distances are different for the various bonding states: 0.12 nm for the triple bond (e.g., acetylene), 0.134 nm for the double bond (e.g., ethylene), and 0.153 nm for the single bond (e.g., ethane). By way of comparison, benzene has 0.140 nm, intermediate between the single- and double-bond values.

[†] P. Jacoby and C. W. Bauer, U.S. patent 4,975,469, Dec. 4,1990.

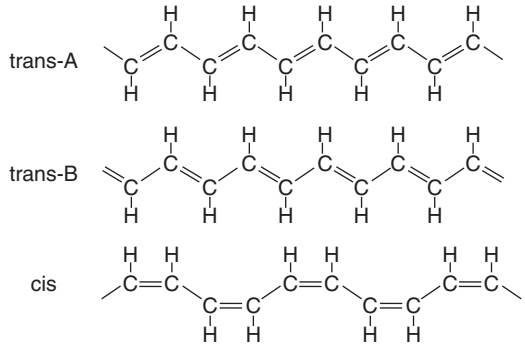

Figure W14.7. Two arrangements of the alternating single and double carbon–carbon bonds in polyacetylene, *trans*-A and *trans*-B. Also shown is the *cis* configuration.

The polyacetylene polymer may be modeled as a one-dimensional tight-binding dimerized chain with two carbon atoms (labeled A and B) per unit cell and unit cell length a. The amplitudes for having an electron reside on the nth A-atom site and the nth B-atom site will be denoted by A_n and B_n, respectively. The NN hopping integrals will be denoted by t and t' for the single- and double-bond distances, respectively. The details of the tight-binding equations are similar to those presented in Section 7.8, but extended here to the case of two atoms per unit cell. Thus

$$t'A_{n+1} + tA_n = \epsilon B_n, \tag{W14.61a}$$

$$tB_n + t'B_{n-1} = \epsilon A_n. \tag{W14.61b}$$

These equations may be simplified with the substitutions $A_n = \alpha \exp(inka)$ and $B_n = \beta \exp(inka)$, leading to

$$\epsilon\beta = (t + t'e^{ika})\alpha, \tag{W14.62a}$$

$$\epsilon\alpha = (t + t'e^{-ika})\beta. \tag{W14.62b}$$

This leads to the solution for the energy eigenvalues

$$\epsilon_\lambda(k) = \pm\sqrt{t^2 + t'^2 + 2tt'\cos(ka)}, \tag{W14.63}$$

where $\lambda = \pm$ and with the first Brillouin zone extending from $-\pi/a$ to π/a. There are two allowed energy bands separated by a gap. The allowed bands extend from $-|t + t'|$ to $-|t - t'|$ and from $|t - t'|$ to $|t + t'|$, respectively. The gap is from $-|t - t'|$ to $|t - t'|$. In virgin polyacetylene the lower band is filled and the upper band is empty. The material is a semiconductor, with a bandgap of 1.4 eV.

To describe the doping by an impurity atom (taken to be a donor, for the sake of definiteness), assume that the donor atom has an ionization energy E_d. The Hamiltonian for the chain-impurity system is

$$H = E_d|I\rangle\langle I| + \sum_{k,\lambda}[\epsilon_\lambda(k)|k, \lambda\rangle\langle k, \lambda| + V_\lambda(k)(|k, \lambda\rangle\langle I| + |I\rangle\langle k, \lambda|)], \tag{W14.64}$$

where $V_\lambda(k)$ governs the hopping back and forth between the donor ion and the polymer chain. The Schrödinger equation $H|\psi\rangle = \epsilon|\psi\rangle$ may be solved with a state of the form

$$|\psi\rangle = g|I\rangle + \sum_{k,\lambda} c_\lambda(k)|k, \lambda\rangle, \tag{W14.65}$$

and with the simplifying assumptions $\langle I|k, \lambda\rangle = 0$, $\langle I|I\rangle = 1$ and $\langle k'\lambda'|k\lambda\rangle = \delta_{\lambda,\lambda'}\delta_{k,k'}$. This leads to

$$E_d g + \sum_{k,\lambda} V_\lambda(k)c_\lambda(k) = \epsilon g, \tag{W14.66}$$

$$\epsilon_\lambda(k)c_\lambda(k) + gV_\lambda(k) = \epsilon c_\lambda(k). \tag{W14.67}$$

Solving the second equation for $c_\lambda(k)$ and inserting it into the first equation results in the eigenvalue equation

$$E_d + \sum_{k,\lambda} \frac{V_\lambda^2(k)}{\epsilon - \epsilon_\lambda(k)} = \epsilon. \tag{W14.68}$$

Assume that $V_\lambda(k) = V$ (independent of λ, k) and replace the sum over k states by an integral over the first Brillouin zone. Then

$$\begin{aligned} \epsilon - E_d &= \frac{V^2}{2\pi}\int_{-\pi/a}^{\pi/a} dk \frac{2\epsilon}{\epsilon^2 - t^2 - t'^2 - 2tt'\cos ka} \\ &= \frac{2V^2}{a}\frac{\epsilon}{\sqrt{(\epsilon^2 - t^2 - t'^2)^2 - 4t^2t'^2}}. \end{aligned} \tag{W14.69}$$

A graphical solution of the resulting sextic equation,

$$(\epsilon - E_d)^2[(\epsilon^2 - t^2 - t'^2)^2 - 4t^2t'^2] = \frac{4V^4\epsilon^2}{a^2}, \tag{W14.70}$$

shows that (at least) one discrete eigenstate will reside within the gap, irrespective of the location of E_d. This will be referred to as the *impurity level*. At $T = 0$ K this level is occupied.

For $T > 0$ K, electrons are donated to the polymer conduction band. (A similar description applies to holes contributed by acceptor dopants.) Resistance is brought about by the backscattering of these carriers by the charged impurity ions. Imagine that the electrons move along the z direction, the direction of alignment of the polymers. The distance of the impurity from the chain is denoted by D. The Coulomb potential presented by an ion at $z = 0$ is then $V(z) = -e/4\pi\epsilon_0\sqrt{z^2 + D^2}$. The matrix element for backscattering is, for $kD \gg 1$,

$$M = \langle\psi_f|V|\psi_i\rangle = -\frac{e^2}{4\pi\epsilon_0}\int_{-\infty}^{\infty}\frac{e^{2ikz}}{\sqrt{D^2 + z^2}}\,dz \longrightarrow -2\frac{e^2}{4\pi\epsilon_0}\sqrt{\frac{\pi}{4kD}}e^{-2kD}, \tag{W14.71}$$

which is seen to fall off rapidly for large values of kD. Thus the high mobility may be due, in part, to the small probability for backscattering events.

However, if the conduction in polyacetlyene is really one-dimensional, and electron–electron interactions are neglected, random scattering will serve to localize the electrons. The net result will be that it will be an insulator. More realistically, the electron–electron interaction is not negligible but is important. The electron–electron interaction serves to keep the electrons apart due to their Coulomb repulsion and lack of screening. This introduces strong correlations in the electronic motions and may override the tendency for localization.

Another approach to explaining the high conductivity of polyacetylene has to do with bond domain walls, called *solitons*. Imagine that one portion of the polymer chain is *trans*-A phase and a neighboring part is *trans*-B phase. This is illustrated in Fig. W14.8, which depicts the domain wall as an abrupt change in bonding configuration, a situation that is not energetically favorable. A lower-energy solution allows for the transition to take place more gradually, on a length scale on the order of 10 lattice constants. In a sense, one must introduce the concept of a partial chemical bond, making a transition from a single to a double bond over an extended distance. A more complete model, put forth by Su et al.[†] includes the elastic and kinetic energy of the lattice as well as the tight-binding Hamiltonian and a coupling between the phonons and the electrons. It may be shown that the undimerized chain (i.e., where there is only one atom per unit cell) is not the state of lowest energy, and a Peierls transition to the dimerized state occurs. This opens a gap at the Fermi level, as in the previous discussion, and makes the polymer a semiconductor rather than a metal. The spatial structure encompassing the foregoing transition from *trans*-A to *trans*-B, called a soliton, appears as a midgap discrete state. It is electrically neutral (i.e., the polymer is able to make the transition from *trans*-A to *trans*-B without the need to bring up or reject additional charge). However, it may be populated by donor electrons, as illustrated in Fig. W14.8.

The charged solitons may propagate along the chain and are difficult to scatter. Since the charge is spread out over an extended distance, it couples weakly to Coulomb scattering centers. The solitons consist of a correlated motion of the electron and the lattice and are similar in some ways to the polarons, familiar from three-dimensional solids. On the downside, however, the solitons may be trapped by defects and this can block their propagation. It is probably a fair statement to say that the final word on the mechanism responsible for the high conductivity of polyacetylene has not been fully decided upon.

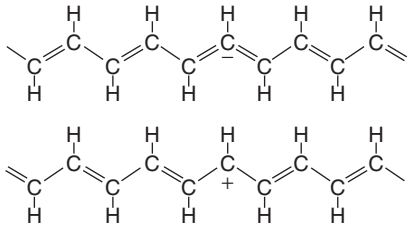

Figure W14.8. Domain walls between A and B phases of *trans*-polyacetylene.

[†] W. P. Su, J. R. Schrieffer, and A. J. Heeger, Solitons in Polyacetylene *Phys. Rev. Lett.*, **42**, 1698 (1979).

In some ways the situation in polyacetylene parallels that of the high mobility found for the modulation doping of GaAs–GaAlAs quantum-well structures (see Section W11.8). In the latter case the interface can be made nearly perfect, with electrons confined to move along the quantum well by the confining walls of the neighboring layers. Since the impurities do not reside in the wells, the Coulomb interaction is weaker and spread out over a large region of space. The impurities are not effective in scattering carriers, hence contributing to the high mobility.

W14.8 Polymers as Nonlinear Optical Materials

Optoelectronic devices are often based on nonlinear optical materials. As seen in Section 8.9, such a material is one in which the polarization vector (electric-dipole moment per unit volume) is a nonlinear function of the electric field of the light. One may make a power series expansion in the electric field(s) and write (employing the summation convention)

$$P_i(\omega) = \epsilon_0 \chi^{(1)}_{i,j}(\omega) E_j(\omega) + \epsilon_0 d^{(2)}_{i,j,k}(\omega; \omega_1, \omega_2) E_j(\omega_1) E_k(\omega_2) + \epsilon_0 d^{(3)}_{i,j,k,l}(\omega; \omega_1, \omega_2, \omega_3) E_j(\omega_1) E_k(\omega_2) E_l(\omega_3) + \cdots, \quad \text{(W14.72)}$$

where $d^{(2)}$ and $d^{(3)}$ are the second- and third-order nonlinear optical coefficients, respectively [see Eq. (8.46)]. For the case where $\omega_1 = \omega_2 = \omega/2$, the quantity $d^{(2)}$ determines the strength of second-harmonic generation (SHG), in which two photons of frequency $\omega/2$ may be combined to form a single photon of frequency ω. Similarly, when $\omega_1 = \omega_2 = \omega_3 = \omega/3$, the value of $d^{(3)}$ governs third-harmonic generation. The more general case of unequal photon frequencies covers various types of three- and four-wave mixing, as well as the dc Kerr effect, in which one of the photons has zero frequency.

For molecules with inversion symmetry, $d^{(2)}$ vanishes identically. Hence, for SHG in polymers, one must choose noncentrosymmetric molecules or solids. For efficient SHG the phase-matching condition must be satisfied; that is, photon energy and momentum must both be conserved:

$$\mathbf{k}_1 + \mathbf{k}_2 = \mathbf{k}, \qquad \omega_1 + \omega_2 = \omega, \quad \text{(W14.73)}$$

where $\omega = kc/n(\omega)$, $\omega_1 = kc/n(\omega_1)$, and $\omega_2 = kc/n(\omega_2)$, n being the index of refraction of the material. The goal is to design materials with as large values for the nonlinear susceptiblities as possible and to have these materials be thermally, mechanically, and chemically stable. These polymers may then be fashioned into fibers, sheets, or bulk material. The custom design of polymers, such as polydiacetylenes, has proved useful in attaining this goal.

To obtain high values for the nonlinear optical coefficients, use is made of the delocalized nature of the π electrons in hydrocarbon molecules. Generally, a "donor" group is placed at one end of a molecule and an "acceptor" group is placed at the other end. They are separated by a bridge region in which there are π electrons. This molecule is then incorporated into a polymer. The values of the susceptibilities depend on dipole matrix elements between electronic states and the differences of energies between these states. Generally, the larger the dipole matrix element, the larger the

susceptibility, and the closer an energy difference matches a photon energy, the larger the susceptibility. It is therefore expeditious to keep the donor group as far away from the acceptor as possible. A virtually excited electron from the donor makes a transition to the acceptor with a concurrent large value for the transition-dipole moment. In $d^{(2)}$ three dipole transitions and two energy denominators are involved. In $d^{(3)}$ there are four transitions and three denominators.

It is important for the various regions of the polymer to act coherently, and therefore it is important that there is alignment of the chain molecules. Since there is generally a static electric-dipole moment associated with the molecule, it may be aligned in an applied dc electric field, in a process called *poling*. The sample is heated above the glass-transition temperature, T_g, the material is poled, and then the temperature is lowered below T_g. The field is then removed and the sample has become an electret, with a net electric-dipole moment per unit volume. This itself has interesting applications in designing piezoelectric materials (in which a strain gives rise to an electric field, and vice versa) and electro-optic materials (in which the index of refraction may be altered by applying external electric fields). An example of a polymer that is used as a nonlinear optical material is 6FDA/TFDB. The molecule is shown in Fig. W14.9. An example of a nonlinear chromophore that may be adjoined to a polymer appears in Fig. W14.10 and is the 3-phenyl-5-isoxazolone compound.

One of the interesting features of polymers is the dependence of $d^{(3)}$ on the length of the chain ($\propto N^{3.5}$ for $N < 100$). This may be understood as follows. The end-to-end distance grows as N^{ν}, with $\nu \sim \frac{3}{5}$. One imagines a virtual excitation involving a "surface" state at the end of the chain. Since there are four transition moments entering $d^{(3)}$, this would give an exponent 4ν. Finally, there are N monomers per chain molecule, so a net exponent of $4\nu + 1 = 3.4$ could be expected. For very large polymers, however,

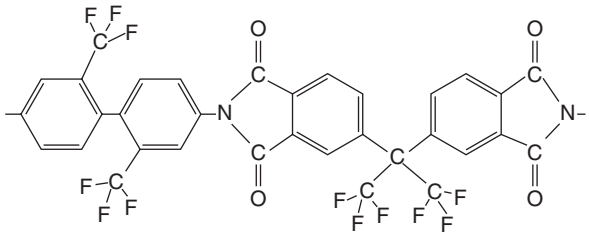

Figure W14.9. Monomer 6FDA/TFDB.

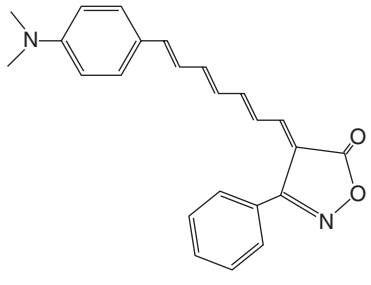

Figure W14.10. Chromaphore 3-phenyl-5-isoxazolone compound.

the dipole approximation would break down and higher frequency-dependent multipole moments would determine the nonlinear optical coefficients.

Recent attention has been directed to photorefractive polymers, such as doped poly(*N*-vinylcarbazole), for use as an optical information-storage material. The physics here is linear rather than nonlinear. A localized light beam directed at the polymer causes a real donor-to-acceptor transition of an electron. This produces a localized electric field that alters the local index of refraction. This constitutes the "write" step. A weak probe laser beam is able to detect the altered index of refraction in the "read" step. Poling in a strong external electric field restores the electrons to the donors, and thus the material is erasable. Since light is involved, one may attain several orders of magnitude greater read and write rates than with conventional magnetic media. By using two write lasers rather than one, it is possible to etch holographic interference patterns into the material.

PROBLEMS

W14.1 Consider a freely rotating chain consisting of N bonds, with the angle between successive bonds constrained to be equal to $\pi - \theta$.

(a) Show that $\langle \hat{u}_j \cdot \hat{u}_{j+k} \rangle = \cos^k \theta$.

(b) Show that the radius of gyration s is given by

$$s^2 = \frac{Na^2}{6} \frac{1 + \cos\theta}{1 - \cos\theta}.$$

W14.2 Show that the radius of gyration of a cyclic freely jointed chain is given by $s^2 = Na^2/12$.

CHAPTER W15

Dielectric and Ferroelectric Materials

W15.1 Capacitors

Improvement in the design of capacitors has progressed steadily since the introduction of the Leyden jar in the nineteenth century. The basic formula for the capacitance of a parallel-plate capacitor is $C = \epsilon_r \epsilon_0 A/d$, where ϵ_r is the dielectric constant, A the surface area of a plate, and d the gap distance between plates. To increase C one either increases ϵ_r, increases A, or decreases d. Early capacitors consisted of metal foils separated by wax ($\epsilon_r \approx 2.5$), mica ($\epsilon_r \approx 3$ to 6), steatite ($\epsilon_r \approx 5.5$ to 7.5), or glass ($\epsilon_r \approx 5$ to 10). The use of titania (rutile) provided a significant increase ($\epsilon_{r_\parallel} = 170$, $\epsilon_{r_\perp} = 86$). This was followed by technology based on the perovskites, such as barium titanate ($\epsilon_r \approx 1000$), whose dielectric constant varies rapidly with temperature, undergoing a near divergence at a phase transition temperature. By going to smaller grain sizes (≈ 1 μm) the divergence was spread out over a larger temperature range, making the $\epsilon_r(T)$ curve flatter. Such perovskites are called *relaxors*. DRAM chips currently utilize capacitors with Si_3N_4 or SiO_2 as the dielectric material. The electrodes are made of doped Si or poly-Si.

The demands for miniaturization largely preclude an increase in the face area A. One exception is the multilayer ceramic capacitor (MLCC), in which case $C = \epsilon_r \epsilon_0 A(N-1)/d$, where N is the number of stacked plates. Electrolytic capacitors are successful in increasing C by reducing the gap distance d to atomic dimensions. In this case the dielectric consists of a monolayer of alumina ($\epsilon_r \approx 4.5$ to 8.4) or tantalum oxide (Ta_2O_5) ($\epsilon_r \approx 21$) sandwiched between a metal and an ionic solution. The inherent difficulty, however, is that electrolytic capacitors work only when polarized in one direction. The oxide layer disappears when the polarity is reversed. This makes them suitable for dc power supplies but not for ac applications. The development of thin-film technology provides another avenue of approach for reducing d. The material SiO ($\epsilon_r \approx 6$) provides a convenient dielectric. SiO is a "mixture" or alloy of Si and SiO_2 (e.g., oxygen-deficient SiO_{2-x}, with $x \approx 1$).

The MLCC typically uses $BaTiO_3$ as the dielectric, although it has some shortcomings. Ideally, the dielectric should have a low electrical conductivity so that the leakage current is not too large. The time constant for decay of charge in a dielectric is given by $\tau = \epsilon/\sigma$. (This formula may be deduced from Gauss's law, $\nabla \cdot \mathbf{D} = \rho$, the constitutive equations $\mathbf{D} = \epsilon\mathbf{E}$ and $\mathbf{J} = \sigma\mathbf{E}$, and the continuity equation $\partial\rho/\partial t + \nabla \cdot \mathbf{J} = 0$.) For high-speed switching applications it is desirable to have $\tau < 1$ μs. For $\sigma = 1\ (\Omega \cdot \text{m})^{-1}$ and $\epsilon = \epsilon_0$, the time constant is only 8.85×10^{-12} s. To obtain a 1-μs storage time requires ϵ/σ to be increased by over five orders of magnitude. It is also desirable to have a high thermal conductivity to avoid the buildup of thermal stresses, a high breakdown strength ($> 4 \times 10^7$ V/m) so that moderate voltages (≈ 200 V) can be imposed across

a small thickness (≈ 5 μm), as well as a capacitance that will not vary appreciably with electric field. One would like to have $d \approx 0.5$ μm, or less, if possible. Current research indicates that $d \approx 10$ μm may soon be feasible. A low dissipation factor is generally sought. The dissipation factor is defined as the ratio of the imaginary part of the dielectric constant to the real part, and is also referred to as the *loss tangent*, $\tan\delta \equiv \epsilon_2/\epsilon_1$. A low firing temperature and a small grain size for the ceramic are assets. A list of typical dielectrics (relaxors) is presented in Table W15.1. The value of the structural phase transition temperature T_c is presented, along with the value of the relative dielectric constant at that temperature. The closer the value of T_c is to room temperature, the higher the value of the dielectric constant will be under normal operating conditions. Much of the research in developing relaxor dielectrics has been aimed at tuning the stoichiometric coefficients to bring T_c close to room temperature. This is illustrated by the perovskite $Pb_{1-x}La_x(Zr_yTi_{1-y})_{1-x/4}O_3$ (PLZT) in Table W15.1. Changing the composition (x, y) from (0.02,0.65) to (0.08,0.7) lowers T_c from 320°C to 20°C and changes ϵ_r at T_c from 4050 to 650. Typical room temperature values of ϵ_r for ($SrTiO_3$, (Ba,Sr)TiO_3, PLZT) are (90–240,160–600, $>$ 1000), respectively.

Electrode materials for use with the perovskites include the metals Ir, Pt, Ru and the conducting oxides RuO_2 and IrO_2.

Grain-boundary barrier layer (GBBL) capacitors achieve a high capacitance essentially by decreasing d. The dielectric consists of a set of microscopic conducting granules, of typical size a, separated from each other by thin insulating surface layers, of dimension d_g. The average number of grains spanning the gap is N. Using $Na + (N+1)d_g = d$, one finds that $N = (d - d_g)/(a + d_g) \approx d/a$. The net capacitance is obtained by regarding the $N + 1$ capacitors as being in series, resulting in

$$C = \epsilon_r\epsilon_0 \frac{A}{Nd_g} = \epsilon_r\epsilon_0 \frac{Aa}{dd_g}. \tag{W15.1}$$

Since $a \gg d_g$, this results in a substantial increase in C.

Capacitor design involves other issues beside having large capacitance. Dissipation is a major concern, and dc conductivity is another. Ion migration can cause currents to flow. These often involve defects, such as oxygen vacancies, moving through the dielectric. The tunneling of electrons from granule to granule in the GBBL capacitors

TABLE W15.1 Properties of Relaxor Dielectrics

Relaxor Material[a]			Transition $T_c(^\circ C)$	ϵ_r(max)
$Pb(Fe_{1/2}Nb_{1/2})O_3$	PFN	FE	112	24,000
$Pb(Mg_{1/3}Nb_{2/3})O_3$	PMN	FE	−0.8	18,000
$Pb(Mg_{1/2}W_{1/2})O_3$	PMW	AF	39	300
$Pb(Zn_{1/3}Nb_{2/3})O_3$	PZN	FE	140	22,000
$PbTiO_3$	PT	FE	490	8,000
$BaTiO_3$	BT	FE	130	12,000
	PLZT	FE	140	12,000

Source: Data from Y. Yamashita, *Am. Ceram. Soc. Bull.*, **73**, 74 (1994).

[a]FE and AF stand for ferroelectric and antiferroelectric transitions, respectively. The composition of PLZT is given by $Pb_{1-x}La_x(Zr_yTi_{1-y})_{1-x/4}O_3$, with $x = 0.07$ and $y = 0.65$.

provides a conduction mechanism. When working with granular materials a concern is the charging of the grains. For small enough granules, the discrete nature of the electronic charge plays an important role in determining the $I-V$ characteristics.

Another concern relates to the variation of capacitance with temperature. Often, circuits are used in which the stability of the RC time constant plays an important role. Since resistance of semiconductors drops with increasing temperature, it could be compensated for by finding a capacitor whose capacitance rises with increasing T. Relaxor materials often have such positive temperature coefficients.

W15.2 Substrates

Substrates are insulators that serve as the foundation upon which microcircuits are supported. Typical materials include alumina, aluminum nitride (both plain and diamond-coated), boron nitride, diamond thin films, mullite, and polyimide films, as well as others. Usually, the Si wafer which serves as the template for Si devices is bonded to a substrate that provides mechanical support and thermal dissipation. Table W15.2 provides a list of some common materials. Patterns of deposited metals, semiconductors, and insulators that comprise the circuit are supported by the Si template. The electrical insulating properties of the substrate are reflected in high values for the electrical resistivity.

Generally, the coefficient of thermal expansion, α, should match that of the semiconductor so that thermal stresses may be minimized. For example, alumina and GaAs have values that are well matched (see Table W15.2). GaAs can be bonded onto alumina with a gold–tin solder. In addition, materials of high thermal conductivity, κ, such as

TABLE W15.2 Properties of Substrate Materials[a]

Substrate	Dielectric Constant ϵ_r (at 1 MHz)	Rupture Modulus RM[b] (MPa)	Coefficient of Thermal Expansion α (10^{-6} K^{-1})	Thermal Conductivity κ (W/m·K)	Processing Temperature T_{proc} (°C)	Resistivity ρ (Ω·m)
Al_2O_3	9.9	550	6.7	17	1500	10^{13}
SiC	9.7	186	4.5	135	2000	—
Si_3N_4	7.0	850	3.4	30	1600	10^{10}
AlN	8.8	300	4.5	180	1900	10^{11}
BeO	6.8	250	7.6	250	2000	—
Mullite	3.8	185	5	6	1400	$>10^{12}$
Cordeirite	5	500	3	2	—	10^{9}
Titania	170	291	7.1	10.4	—	—
Borosilicate glass	4.0	70	3	2	800	—
Quartz + borosilicate	7.9	150	7.9	16	850	—
Si	11.7	—	2.5	151	—	—
GaAs	—	—	6.5	54	—	10^{6}

Source: Data from L. M. Sheppard, Ceram. Bull., **70**, 1467 (1991)).

[a]Note that large variations of reported values appear in the literature.
[b]Fracture strength under a bending load.

AlN, permit heat to be dissipated rapidly. The mechanical strength of the substrate should be high so that it can withstand the thermal stresses. Of paramount importance are the ability to deposit metallic layers on the material and to be able to withstand whatever machining operations are involved.

In photolithography there is the need to blacken the substrate, so that it will not reflect stray light and damage the latent image being cast upon a VLSI circuit. Oxides of Co, Cr, Fe, Nb, Ta, Ti, W, and Zr serve to blacken AlN without diminishing its high thermal conductivity.

For high-speed switching operations it is desirable to have small capacitances, so that the RC time constant will be small. This necessitates using substrates with small dielectric constants, preferably with $\epsilon_r < 5$. To this end, porous glasses may be used, with $\epsilon_r \approx 2$, although the presence of pores mechanically weakens the substrate. Boron phosphate glass ceramics offer materials with $\epsilon_r \approx 4$ and have very high resistivity, $\approx 10^{14}$ Ω·m. One may also use layered structures, making use of the fact that for capacitors in series, $C_{\text{total}} < \min(C_1, C_2, \ldots)$. For example, fluorohectorite is a synthetic mica silicate with layers separated from each other by sheets of hydrated cations. One may place layers of low-ϵ polymer between the sheets to form a low-capacity microstructure. Since the packaging of a VLSI chip also contributes to the capacitance, materials with low dielectric constants should be employed. Such materials as Teflon, polyimides, and benzocyclobutenes are often utilized.

W15.3 First-Order Ferroelectric Phase Transitions

First-order transitions may be handled by returning to Eq. (15.29) of the textbook[†] and assuming that $c > 0$ and $b < 0$. In place of Eq. (15.30), one has

$$\frac{\partial g}{\partial P} = a_0(T - T_0)P + bP^3 + cP^5 = 0. \tag{W15.2}$$

There now exists a temperature T_C such that for $T > T_C$, the minimum value of g is g_0 and there is no spontaneous polarization (i.e., $P = 0$). To determine T_C, the equations $\partial g/\partial P = 0$ and $g = g_0$ are solved simultaneously, giving

$$T_C = T_0 + \frac{3b^2}{16a_0c}, \tag{W15.3}$$

$$P = P(T_C) = \pm\sqrt{-\frac{3b}{4c}}. \tag{W15.4}$$

Note that the order parameter undergoes a discontinuity as the temperature is lowered below T_C. For temperatures below T_C, the spontaneous polarization is given by

$$P = \pm\sqrt{-\frac{b}{2c} + \sqrt{\frac{b^2}{4c^2} - \frac{a_0}{c}(T - T_0)}}. \tag{W15.5}$$

[†] The material on this home page is supplemental to *The Physic and Chemistry of Materials* by Joel I. Gersten and Frederick W. Smith. Cross-references to material herein are prefixed by a "W"; cross-references to material in the textbook appear without the "W."

The dielectric constant is obtained as before. For $T > T_C$

$$\epsilon_r = 1 + \frac{1}{\epsilon_0 a_0 (T - T_0)}, \tag{W15.6}$$

which is the same as in Eq. (15.35), but remains finite at $T = T_C$. For $T < T_C$ one finds that

$$\epsilon_r = 1 + \frac{1}{4\epsilon_0 c x (x - b/2c)}, \tag{W15.7a}$$

where

$$x = \sqrt{\frac{b^2}{4c^2} - \frac{a_0}{c}(T - T_0)}. \tag{W15.7b}$$

Since $b < 0$, this remains finite at $T = T_0$.

The extension to three dimensions may be obtained by writing the Gibbs free-energy density in a form consistent with cubic symmetry:

$$g = g_0 - \mathbf{E} \cdot \mathbf{P} + \frac{a}{2}P^2 + \frac{b}{4}P^4 + \frac{b' - b}{2}(P_y^2 P_z^2 + P_z^2 P_x^2 + P_x^2 P_y^2) + \frac{c}{6}P^6 + c'[P_x^4(P_y^2 + P_z^2) + P_y^4(P_z^2 + P_x^2) + P_z^4(P_x^2 + P_y^2)] + c'' P_x^2 P_y^2 P_z^2 + \cdots \tag{W15.8}$$

where $\mathbf{E}$ is the electric field vector. Matters may be simplified by letting $c' = 0$ and $c'' = 0$. As before, one begins with $\mathbf{E} = 0$. At the minimum value of g, three conditions apply:

$$\frac{\partial g}{\partial P_x} = P_x[a + bP^2 + (b' - b)(P_y^2 + P_z^2) + cP^4] = 0, \tag{W15.9a}$$

$$\frac{\partial g}{\partial P_y} = P_y[a + bP^2 + (b' - b)(P_z^2 + P_x^2) + cP^4] = 0, \tag{W15.9b}$$

$$\frac{\partial g}{\partial P_z} = P_z[a + bP^2 + (b' - b)(P_x^2 + P_y^2) + cP^4] = 0, \tag{W15.9c}$$

Various extrema may be identified. The first is at $(P_x, P_y, P_z) = (0, 0, 0)$, at which point the crystal has cubic symmetry and $g = g_0$. A second solution occurs at $(P_x, P_y, P_z) = (0, 0, \pm|P_z|)$, in which case

$$|P_z| = \sqrt{-\frac{b}{2c} + \rho\sqrt{\left(\frac{b}{2c}\right)^2 - \frac{a}{c}}}, \tag{W15.10}$$

where $\rho = \pm 1$. This solution corresponds to the breaking of cubic symmetry. There exists a spontaneous polarization, and the crystal has tetragonal symmetry. (Equivalent solutions follow from the cyclical permutation of P_x, P_y and P_z.) The reality of this solution requires that $b^2 > 4ac$. If $b < 0$, then $\rho = +1$ is always possible whereas if $b > 0$, then $\rho = -1$ is always possible. If $a < 0$ and $b < 0$, then $\rho = -1$ can also

occur. If $a < 0$ and $b > 0$, then $\rho = +1$ is another possibility. The Gibbs free-energy density at the extrema is given by

$$g = g_0 - \frac{ba}{12c} + \left(\frac{a}{3} - \frac{b^2}{12c}\right) P_z^2. \tag{W15.11}$$

If this Gibbs free-energy density lies below g_0, it will be the preferred thermodynamic state. Note that due to the symmetry of the solution, the parameter b' does not appear in Eq. (W15.10) or (W15.11).

For $E_z \neq 0$ the dielectric constant is determined approximately as before by solving

$$\frac{\partial g}{\partial P_z} = P_z(a + bP_z^2 + cP_z^4) - E = 0. \tag{W15.12}$$

For the cubic case the result expressed in Eq. (W15.6) is found.

For the tetragonal case

$$\epsilon_r = 1 + \frac{1}{4\epsilon_0 c}\left[\left(\frac{b}{2c}\right)^2 - \frac{a}{c} - \rho\sqrt{\left(\frac{b}{2c}\right)^2 - \frac{a}{c}}\right]^{-1/2}. \tag{W15.13}$$

Note that the dielectric constant diverges as b^2 approaches 4ac.

W15.4 Nonvolatile Ferroelectric Random-Access Memory

Computer random-access memory (RAM) currently employs semiconductor technology. One major drawback is that the information stored in RAM is lost in the event of a power failure or other sudden shutdown of the computer. A remedy for this is the use of nonvolatile ferroelectric random-access memory (NVFRAM). Ferroelectric domains are used to store the bits of information. A binary 1 corresponds to the electric polarization vector, **P**, pointing in one direction and a binary 0 to **P** pointing in the opposite direction. Since the polarization within a domain is determined by ionic displacements within the unit cells, domain walls typically propagate at speeds characteristic of ionic motion (i.e., the speed of sound, $c_s \sim 10^3$ m/s). For a domain of size $L \sim 1$ μm, this translates into a switching time of $L/c_s \sim 1$ ns. In addition to their nonvolatility, NVFRAMs can be written and erased many times (10^9–10^{13}) without degradation of switching polarization (fatigue), have low leakage currents, and retain their polarization state for a long time.

Many phenomena appearing in ferroelectrics have analogs in ferromagnetism. In particular, the hysteresis loops of ferroelectricity, obtained when P is plotted against the electric field, E, are analogous to the hysteresis loops of ferromagnetism, in which the magnetization, M, is plotted as a function of the magnetic intensity, H. The latter case is studied in some detail in Chapter 17, so only an abridged introduction to hysteresis is given here.

The hysteresis loop describes P as a double-valued function of E and is illustrated in Fig. W15.1. Suppose that initially all the electric dipole moments of a domain are aligned by applying a strong electric field. The value of the polarization vector will then be $P_{\text{sat}} = n\mu$, where n is the number of unit cells per unit volume and μ is the electric-dipole moment of a unit cell. Upon lowering E to zero, the polarization drops to a value P_{rem}, called the *remanent polarization*. Thus, even in the absence of an electric

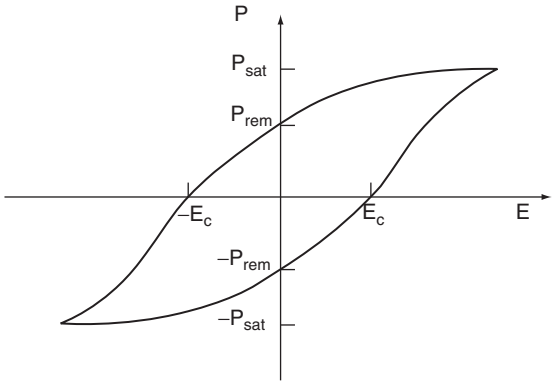

Figure W15.1. Ferroelectric hysteresis loop.

field, the polarization state is preserved and P_{rem} can serve as the binary 1 bit of the state of memory. This is what provides the nonvolatility of the memory. If the field is made more negative, the polarization will finally be zero at a value $E = -E_c$, where E_c is called the *coercive field*. If the field is made strongly negative, the polarization ultimately saturates at $-P_{\text{sat}}$. Reversing the process, and making $E = 0$, leads to a polarization $-P_{\text{rem}}$. This can represent the binary 0 of a state of memory. Increasing E to the value $+E_c$ removes the polarization, and making it strongly positive restores the saturation polarization P_{sat}. The net work done in going around the hysteresis loop is the area enclosed by the loop, $\oint E\,dP$, and is dissipated as heat.

In practical memory chips there are a large number of cells present on a surface array. Each domain is defined by the intersection of two conducting strips, one called the *word line* and the other called the *bit line*. To write a given bit, half the switching voltage is applied across the word line and half across the bit line, thus creating P_{rem}. To read a given bit, a switching voltage is applied. Half of it is supplied by the word line and half by the bit line, as in the writing case. If the cell is polarized in the $+P_{\text{rem}}$ state and a positive voltage is applied, a relatively small change in the polarization occurs, $P_{\text{sat}} - P_{\text{rem}}$. If the cell is in the $-P_{\text{rem}}$ state and a positive voltage is applied, a polarization change $P_{\text{sat}} + P_{\text{rem}}$ occurs. The resulting polarization current $J_P = -\partial P/\partial t$ produces a transient sensing voltage that may be detected and compared with that of a standard domain which is always switched from the + state. After reading the bit, the domain polarization is restored to its initial state by applying the appropriate electric field.

One problem is to prevent the polarization state of one domain from interacting with neighboring domains (i.e., *cross-talking*). Isolation transistors are inserted between domains to prevent this from happening.

Ferroelectrics currently used in NVFRAMs include the perovskite PZT [$Pb(Zr_xTi_{1-x})O_3$, with $x \approx 0.53$] and the layered perovskites SBT ($SrBi_2Ta_2O_9$) and SNT ($SrBi_2Nb_2O_9$). In the SBT crystal structure the unit cell consists of a stack along the c axis consisting of alternating $SrTa_2O_6$ perovskite blocks and planes of atoms containing Bi_2O_3. Typical parameters for some of these materials are $P_{\text{rem}} = 0.4$ C/m^2 and $E_c = 2800$ to 5000 kV/m for PZT, and $P_{\text{rem}} = 0.18$ C/m^2 and $E_c = 4500$ kV/m for SBT. The values depend on film thickness and the method of processing. The choice of proper electrode materials is of importance in decreasing the fatigue of the devices, as it can have a substantial effect on the microstructure of

the ferroelectric. For example, the sandwich combination Pt/PZT/Pt fatigues rapidly, whereas RuO_2/PZT/RuO_2, deposited on a MgO(100) substrate, has little fatigue. Other electrodes include IrO_2 and (La,Sr)CoO_3. The presence of oxygen vacancies can lead to charge trapping, which can pin domain walls and locally shift P_{rem} and E_c.

W15.5 Quartz Crystal Oscillator

As in the case of a bell, a crystal of finite size will "ring" with a characteristic set of normal-mode frequencies when excited mechanically. In the case of a piezoelectric crystal, electric fields are used to provide the stimulus. The frequencies are given approximately by $\omega \sim c_s/L$, where c_s is a speed of sound and L is a typical dimension. Although any piezoelectric crystal may be used, α-quartz is most commonly employed, and attention here is restricted to it. Oscillators with frequencies in the megahertz range are fabricated routinely. They are employed in clocks, computers, and radio transmitters and receivers. The quartz-crystal monitor is a basic tool for measuring thin-film deposition rates of adsorbates.

The nature of the modes of excitation of the crystal is determined by the shape of the cuts relative to the unit cell. The cuts are specified in terms of the dimensions of a rectangular parallelipiped of (thickness, length, width) $= (t, l, w)$, axes of rotation (x, y, z), and Euler angles of rotation of the parallelipiped relative to the crystal axes (ϕ, θ, ψ). The notation for the crystal cut is $xyz(t, l, w)\phi\theta\psi$. Various cuts are in use, labeled by the notation AT, BT, CT, DT, ET, GT, MT, NT, and so on. These cuts are special in that the piezoelectric coefficients are, to a first approximation, independent of temperature. Figure W15.2 shows a quartz crystal along with the directions of some of the cuts.

It should be noted that quartz is an example of an enantiomorphous crystal, which means that there are two independent but equivalent structures which are the mirror images of each other, referred to here as *right-* and *left-handed quartz*.

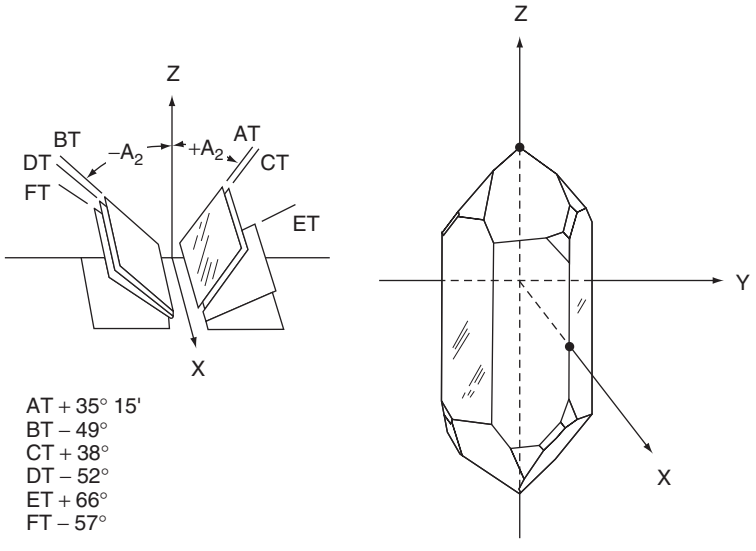

Figure W15.2. Quartz crystal along with some of the cuts used to create oscillator crystals. (Adapted from R. A. Heising, *Quartz Crystals for Electrical Circuits*, Van Nostrand, New York, 1946.)

The normal-mode frequencies are determined by solving the elastic equations of motion as in Section 10.10. To be more general, the expanded notation of Eq. (10.13) will be used, so

$$\rho\frac{\partial^2 u_\alpha}{\partial t^2} = -\rho\omega^2 u_\alpha = \sum_\beta \frac{\partial \sigma_{\alpha\beta}}{\partial x_\beta} = \sum_{\beta\mu\nu} C_{\alpha\beta\mu\nu}\frac{\partial \varepsilon_{\mu\nu}}{\partial x_\beta}, \tag{W15.14}$$

where ρ is the density, $\mathbf{u}$ the displacement, $\sigma_{\alpha\beta}$ the stress tensor, $\varepsilon_{\mu\nu}$ the strain tensor, and $C_{\alpha\beta\mu\nu}$ the elastic coefficient tensor. All indices run from 1 through 3. The boundary conditions are that the normal components of the stress tensor vanish on the surface:

$$\sum_\beta \sigma_{\alpha\beta}\hat{n}_\beta = 0. \tag{W15.15}$$

Quartz (a trigonal or rhombohedral crystal) has the (symmetric) elastic coefficient tensor (in reduced notation)

$$\mathbf{C} = \begin{bmatrix} C_{11} & C_{12} & C_{13} & C_{14} & 0 & 0 \\ \cdot & C_{11} & C_{13} & -C_{14} & 0 & 0 \\ \cdot & \cdot & C_{33} & 0 & 0 & 0 \\ \cdot & \cdot & \cdot & C_{44} & 0 & 0 \\ \cdot & \cdot & \cdot & \cdot & C_{44} & C_{14} \\ \cdot & \cdot & \cdot & \cdot & \cdot & 2(C_{11}-C_{12}) \end{bmatrix} \tag{W15.16}$$

where $(C_{11}, C_{12}, C_{13}, C_{14}, C_{33}, C_{44}) = (8.68, 0.71, 1.19, 1.80, 10.59, 5.82) \times 10^{10}$ Pa. The density is $\rho = 2649$ kg/m^3. The piezoelectric tensor is

$$\mathbf{d} = \begin{bmatrix} d_{11} & -d_{11} & 0 & d_{14} & 0 & 0 \\ 0 & 0 & 0 & 0 & -d_{14} & -2d_{11} \\ 0 & 0 & 0 & 0 & 0 & 0 \end{bmatrix}, \tag{W15.17}$$

with $(d_{11}, d_{14}) = (2.3, -0.67)$ pm/V (for right-handed quartz). For left-handed quartz the signs of d_{11} and d_{14} are opposite. The dielectric constant tensor is

$$\varepsilon_r = \begin{bmatrix} \varepsilon_1 & 0 & 0 \\ 0 & \varepsilon_1 & 0 \\ 0 & 0 & \varepsilon_2 \end{bmatrix} \tag{W15.18}$$

with $(\varepsilon_1, \varepsilon_2) = (4.34, 4.27)$. The coefficients of linear expansion are described by the tensor

$$\boldsymbol{\alpha} = \begin{bmatrix} \alpha_1 & 0 & 0 \\ 0 & \alpha_1 & 0 \\ 0 & 0 & \alpha_2 \end{bmatrix} \tag{W15.19}$$

with $(\alpha_1, \alpha_2) = (14.3, 7.8) \times 10^{-6}$ K^{-1}.

After solving the wave equation, expressions for the various modes are obtained. Consider here one such mode. The AT-cut $(\phi, \theta, \psi) = (-90^\circ, 35^\circ 15', 90^\circ)$ crystal has

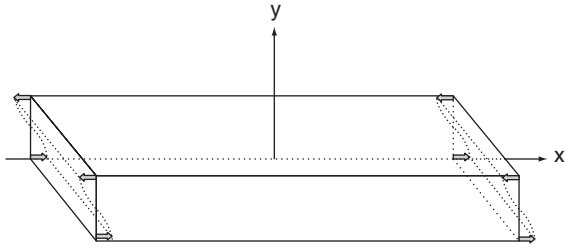

Figure W15.3. Shear oscillation of a quartz crystal oscillator. (Adapted from R. A. Heising, *Quartz Crystals for Electrical Circuits*, Van Nostrand, New York, 1946.)

a mode that undergoes a shear oscillation described by the equation

$$u_x(y,t) = U_0 \cos\frac{n\pi y}{d} e^{-i\omega_n t}, \tag{W15.20}$$

where U_0 is the amplitude and

$$\omega_n = n\frac{\pi}{d}\sqrt{\frac{C_{66}}{\rho}}, \qquad n\ odd. \tag{W15.21}$$

The thickness of the slab is denoted by d. This formula implies a wave speed of $c_s = \sqrt{C_{66}/\rho} = 7757$ m/s for quartz, using $C_{66} = 2(C_{11} - C_{12})$. The vibrational motion is depicted in Fig. W15.3.

One of the main problems with the crystal oscillator is that the resonant frequency changes with temperature, due to thermal expansion and a temperature variation of the elastic constants. One may describe the frequency drift over a restricted range by the linear formula $\Delta f / f_0 = a(T - T_0)$, where a is called the *temperature coefficient*. The size of the parameter a depends on the nature of the crystal cut. For example, in AT-cut quartz, if $T_0 = 43°\text{C}$, then $a = 0$ in the neighborhood of $T = T_0$. This makes the AT oscillator stable against (small) temperature fluctuations. The various popular crystal cuts have different temperatures at which they attain optimum thermal stability. Thermistors operating in conjunction with microprocessors can now accurately compensate for the thermal drift of these oscillators and the precise cutting of crystals is less necessary than it once was.

One interesting application of crystal oscillators is for use as a thickness monitor for vapor-deposition technology. A layer of adsorbed material on the surface of a crystal oscillator increases the system's inertia and lowers the resonant frequency by an amount proportional to the additional mass. Thus, for the quartz-crystal deposition monitor (QCM), an adlayer of Al on an AT-cut slab with a resonant frequency of 6 MHz will shift the resonant frequency by 22.7 Hz per nanometer of adsorbate. With precision-counting electronics, such shifts are readily measurable.

W15.6 Lithium-Ion Battery

The need for a compact reliable battery for computers, watches, calculators, and implantable medical devices has prompted the invention of the lithium-ion battery. Early batteries did not carry enough energy per unit mass. For

example, the lead-acid battery can provide only ≈ 35 W·h/kg (70 W·h/L) and the Ni/Cd battery ≈ 25 W·h/kg (100 W·h/L). In contrast, the Li battery provides ≈ 200 W·h/kg (250 W·h/L), as compared with gasoline, which can provide $\approx$ 15,000 W·h/kg of thermal energy (1 W·h = 3600 J). Any battery has mass and occupies a volume. For some applications mass is the more crucial parameter, so one rates the battery in terms of W·h/kg. In other applications volume may be more crucial, so the rating in terms of W·h/L is more relevant.

The Li battery consists of three parts: the anode (lithium), the electrolyte, and the cathode. Since Li reacts strongly with aqueous solutions, the electrolyte is a liquid that must be aprotic (not contain hydrogen ions). Ideally, one would want an electrolyte with a high solubility for lithium salts and a high mobility for the ions. This involves the use of electrolytes with high dielectric constants and low viscosities. Both of these effects are understandable in terms of elementary physics.

When an ion of charge q is placed in a solvent, there is an electrostatic lowering of its energy by the Born solvation energy. This is illustrated in Fig. W15.4, which shows the solvent molecules as dipoles which become locally aligned with the electric field of the ion. Assuming that a solvation hole of radius a is produced around the ion, the solvation energy is $U = (1 - 1/\epsilon_r)q^2/8\pi\epsilon_0 a$. With large ϵ_r the solvation energy is increased. In addition, a large value of ϵ_r implies that ions are shielded from each other's influence by the polarization charge that gathers around the ions. The ions are less likely to impede each other's motion at high concentrations.

An applied electric field $\mathbf{E}$ leads to a steady-state ionic velocity $\mathbf{v}_i = \mu_i \mathbf{E}_i$, where μ_i is the ith ion's mobility. The net conductivity is $\sigma = \Sigma n_i q_i \mu_i$, where n_i, q_i, and μ_i are the concentration, charge, and mobility of the respective ions. Neglecting ion–ion interactions, the electric force and the Stokes viscous force on a given ion cancel at equilibrium. Thus $q_i\mathbf{E} - 6\pi\eta r_i \mathbf{v}_i = 0$, where η is the viscosity of the liquid and r_i is the ionic radius (including whatever "hydration" shell accompanies it). Thus

$$\mu_i = \frac{q_i}{6\pi\eta r_i}. \tag{W15.22}$$

The lower the viscosity of the electrolyte, the higher the mobility of the ions and the lower the internal resistance of the battery. Consider an electrolyte of thickness L and cross-sectional area A. The internal resistance is computed by regarding each ionic

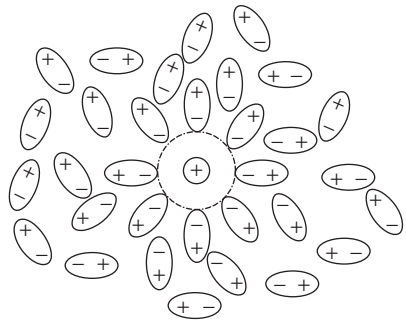

Figure W15.4. Dipoles of the solvent become polarized by the ion.

TABLE W15.3 Electrolyte Solvents[a]

Electrolyte Solvent	Dielectric Constant ϵ_r	Viscosity η (cp)	Temperature (°C) Melting T_m	Boiling T_b
Acetonitrile (AN)	38	0.35	−46	82
Dimethoxyethane (DME)	7.2	0.46	−58	84
N,*N*-Dimethylformate (DMF)	37	0.80	−61	158
Methylformate (MF)	65	0.63	−99	32
Propylene carbonate (PC)	64	2.53	−49	241
Nitromethane (NM)	36	0.62	−29	101
Dimethylsulfite (DMSI)	23	0.77	−141	126
Tetrahydrofuran	7.6	0.46	−109	66
Ethyl acetate (EC)	6.0	0.44	−84	77

Source: Data from H. V. Venkatasetty, ed., *Lithium Battery Technology*, Wiley, New York, 1984.

channel as operating in parallel with the others, so

$$\frac{1}{R_{\text{int}}} = \sum_i \frac{1}{R_i} = \sum_i \frac{A}{L}\sigma_i = \frac{A}{6\pi\eta L}\sum_i \frac{n_i q_i^2}{r_i} \tag{W15.23}$$

Clearly, a low viscosity favors a low internal resistance.

In Table W15.3 data are presented relevant to some of the common organic solvents used in conjunction with lithium salts as electrolytes for lithium batteries. The melting and boiling temperatures (T_m and T_b) define the temperature limits for the electrolyte remaining a liquid.

The electrolyte consists of salt dissolved in the organic solvent. Typical salts employed are LiCl, LiBr, LiI, $LiAsF_6$, LiSCN, $LiNO_3$ and $LiClO_4$. See also Fig. 14.14, which describes the use of $p(EO)_9LiCF_3SO_3$ as a polymer electrolyte. Both the Li^+ and the corresponding negative ions contribute to the electrical current. Interestingly enough, the negative ion often has the higher mobility, despite the fact that its bare radius is larger than that of the positive ion. The reason has to do with the "hydration" shell. Positive ions, being smaller, bind solvent ions more effectively than do negative ions. The solvated ion moves as a unit. Typically, the negative ion may have twice the mobility of the positive ion.

Some common cathode materials employed are CF_x, CuO, CuS, FeS, FeS_2, MnO_2, MoS_2, V_6O_{13}, $SOCl_2$, V_2O_5, and $Bi_2Pb_2O_5$. Often, these are intercalated into graphite or another binder. In Table W15.4 typical battery systems are listed along with their open-circuit voltage and operating voltages. Also listed are the energy densities stored in the batteries. The open-circuit voltages, V_{open}, are determined by the difference in the standard electrode potentials between the cathode and the anode (see Section W12.4, where corrosion is discussed).

W15.7 Fuel Cells

Fuel cells (FCs) are batteries in which there is a continuous input of fuel and oxidizer and a corresponding output of electrical power as well as waste products and waste

TABLE W15.4 Common Lithium-Ion Battery Configurations

Cathode	Electrolyte	Open-Circuit Voltage V_{open} (V)	Operating Voltage V_{oper} (V)	Energy Density u (W·h/kg)
CF_x	DME/PC + $LiBF_4$	3.4	2.6	235
CuO	1,3-dioxolane	2.4	1.3	165
CuS	—	2.1	1.8	198
FeS	Li halide salts	1.4	1.3	105
FeS_2	$LiCF_3SO_3$ in solvent	1.9	1.5	220
MnO_2	—	3.3	2.8	150
MoS_2	PC/Ec + $LiAsF_6$	2.4	1.9	61
V_6O_{13}	PE + $LiClO_4$	3.3	3.0	200
$SOCl_2$	Thionyl chloride + $LiAlCl_4$	3.7	3.2	385
V_2O_5	ME + $LiAsF_6$ + $LiBF_4$	3.4	2.8	264

Source: Data from C. D. S. Tuck, ed., *Modern Battery Technology*, Ellis Horwood, New York, 1991.

heat. FCs were invented in 1836 by Sir William Grove. The present FCs operate on the inverse reaction to the electrolysis of water, $2H_2 + O_2 \rightarrow 2H_2O$, which is an exothermic reaction in the liquid phase with $\Delta G = -4.92$ eV. The cells offer the possibility of providing a clean and efficient energy source. The hope is that they will some day become inexpensive enough to be more widely used.

There are five basic designs for the cells: the alkaline fuel cell (AFC), the proton-exchange membrane fuel cell (PEMFC), the phosphoric acid fuel cell (PAFC), the molten-carbonate fuel cell (MCFC), and the solid-oxide fuel cell (SOFC). The operating temperature ranges for these cells are quite different. For the AFC, PEMFC, PAFC, MCFC, and SOFC devices, the temperature ranges are 60 to 200, 60 to 110, 150 to 210, 550 to 700, and 1000 to 1100°C, respectively. In the case of the MCFC and SOFC, elevated temperatures are needed to have sufficient ion mobility through the electrolyte.

A typical fuel cell is shown schematically in Fig. W15.5. In the PEMFC, hydrogen is convected through the anode and impinges on a platinum catalyst layer. The reaction $H_2 \rightarrow 2H^+ + 2e^-$ is exothermic when it occurs on the catalyst. The electrons flow into the external circuit and the protons diffuse into the proton-exchange membrane which

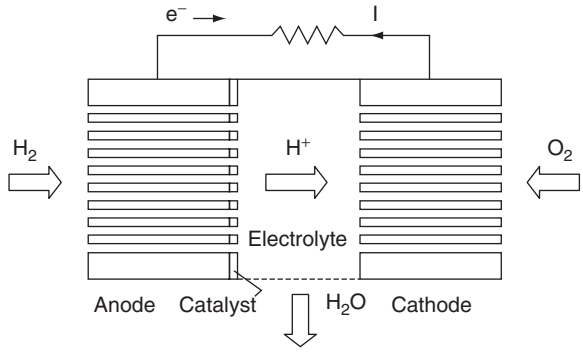

Figure W15.5. Prototype of a typical PEMFC fuel cell using hydrogen as the fuel.

serves as the electrolyte. The membrane is typically a material with a high proton conductivity, such as a sulfonated fluorocarbon polymer (NAFION), or the sulfonated styrene/ethylene–butylene/styrene copolymer. On the other side of the membrane is the cathode.† Oxygen diffuses in from the other side of the FC through the cathode and combines with the protons and the electrons returning from the circuit according to the reaction $4H^+ + O_2 + 4e^- \rightarrow 2H_2O$. Since there are four electrons pumped into the circuit for the reaction $2H_2 + O_2 \rightarrow 2H_2O$, the theoretical EMF for the hydrogen FC is $\epsilon = -\Delta G/4e = 1.23$ V. A fuel-cell generator generally consists of a stack of several hundred FCs with the batteries connected in series with each other.

The internal resistance of the FC limits the actual terminal voltage when a current is drawn from it. This is determined largely by the mean free path of the ions in the electrolyte as well as by whatever hydrodynamic constraints are placed on the flows. For example, a transition from laminar to turbulent flow for the hydrogen and oxygen flowing through the electrodes will impose a constraint on how rapidly fuel and oxidant may be delivered to the FC. In addition, thermally activated reverse reactions at the electrodes (such as $2H^+ + 2e^- \rightarrow H_2$ at the anode and $2H_2O \rightarrow 4H^+ + O_2 + 4e^-$ at the cathode) compete with the forward reactions, giving rise to what are called *exchange overpotentials*. These reactions act as batteries with reverse polarity in series with the FC.

The theoretical efficiency for the conversion of chemical energy to electrical energy in the FC is high. It may be computed from a knowledge of the enthalpy change $\Delta H = -5.94$ eV in the liquid phase and the Gibbs free energy change $\Delta G = -4.92$ eV. Since the waste heat is $Q = T\Delta S = \Delta H - \Delta G$, the efficiency is $\eta = \Delta G/\Delta H = 82.8\%$. Practical MCFCs have $\eta \approx 60\%$ and PAFCs have $\eta \approx 40\%$.

One of the requirements of the electrolyte is that it be impervious to the reactants but allow the ions to pass through with high conductivity. In the SOFC the electrolyte is ZrO_2/Y_2O_3 and it is the O^{2-} ion that diffuses through the electrolyte. In the MCFC the electrolyte is Li_2CO_3/K_2CO_3. The AFC uses KOH as the electrolyte and the PAFC uses phosphoric acid, H_3PO_4. In the AFC OH^- ions are the diffusing species, and in the MCFC they are the CO_3^{2-} ions.

One of the main problems with fuel cells is the preparation of the hydrogen fuel. Ideally, one would like to produce it from fuels such as methane by a process called *reforming*. The hydrogen could be stored temporarily in metal hydrides. Additional problems to FC design arise from poisoning of the catalysts by CO or CO_2.

REFERENCES

Batteries

Tuck, C. D. S., ed., *Modern Battery Technology*, Ellis Horwood, New York, 1991.

Venkatasetty, H. V., ed. *Lithium Battery Technology*, Wiley, New York, 1984.

Quartz-Crystal Oscillator

Heising, R. A., *Quartz Crystals for Electrical Circuits*, Van Nostrand, New York, 1946.

† Note that the term *anode* is used here as the electrode which acts as the source of positive charge inside the battery and negative charge outside the battery. This is opposite to the more conventional definition.

Nonvolatile Ferroelectric RAM

Auciello, O., J. F. Scott, and R. Ramesh, The physics of ferroelectric memories, *Phys. Today*, July 1998, 22.

Fuel Cells

Hoogers, G., Fuel cells: power for the future, *Phys. World*, Aug. 1998, 31.

Kartha, S., and P. Grimes, Fuel cells: energy conversion for the next century, *Phys. Today*, Nov. 1994, 54.

PROBLEM

W15.1 Consider the AT-cut quartz-crystal deposition monitor. Let c_s denote the speed of sound in quartz. Derive the formula for the shift of resonant frequency of the oscillator, Δf, when an adlayer of thickness δ and mass density ρ_a is deposited on the surface:

$$\frac{\Delta f}{f} = f\frac{\delta}{c_s}\frac{\rho_a}{\rho},$$

where ρ is the density of quartz.

CHAPTER W16

Superconductors

W16.1 Further Discussion of Thermal Conductivity in Superconductors

When heat is conducted primarily by the electrons in the normal state for $T > T_c$ (i.e., when $\kappa_n \approx \kappa_{en}$), then below T_c, κ_s falls rapidly below κ_n. This is illustrated in Fig. W16.1*a* for the elemental superconductor Al. In this case $\kappa_s \approx \kappa_{es}$ is observed to approach zero exponentially as T decreases, again providing strong evidence for a superconducting energy gap. When the conduction of heat by phonons dominates in the normal state for $T > T_c$ (i.e., when $\kappa_n \approx \kappa_{ln}$), as is often the case in alloys where electron-impurity scattering effects are important and also in the high-T_c superconductors discussed in Section 16.5 of the textbook,[†] then below T_c, $\kappa_s \approx \kappa_{ls}$. In this case, κ_s can actually be greater than the corresponding normal-state value κ_n, as illustrated in Fig. W16.1*b* for superconducting alloys of Pb with In and Bi. In most cases both the conduction electrons and the phonons make appreciable contributions to the conduction of heat in the normal state above T_c, so the variation of $\kappa_s(T)$ below T_c lies between the two limits presented here.

The situation is more complicated when the superconductor is in the mixed state. The normal electrons associated with the vortices can scatter phonons, thus decreasing κ_{ls}, but can also transport heat, thus increasing κ_{es}.

W16.2 Two-Fluid Model

The *two-fluid model* of Gorter and Casimir[‡] presented in 1934 is a classical thermodynamic treatment which assumes that in the superconducting state the conduction electrons can be separated into two separate, interpenetrating but noninteracting phases or fluids. In this model the concentration of conduction electrons for $T < T_c$ is given by $n = n_s(T) + n_n(T)$, where n_s and n_n are the concentrations of the *superconducting* and *normal* electrons, respectively. The fraction of superconducting electrons is $f_s = n_s/n$, while for the normal electrons, $f_n = n_n/n = 1 - f_s$. It is assumed that both n_s and n_n are temperature dependent, with $n_s(T_c) = n_n(0\ \text{K}) = 0$ and $n_s(0\ \text{K}) = n_n(T_c) = n$.

According to one approach, the superconducting fraction is given by $f_s(T) = 1 - (T/T_c)^4$ and the Gibbs free energy per unit volume of the superconducting state is

[†] The material on this home page is supplemental to *The Physics and Chemistry of Materials* by Joel I. Gersten and Frederick W. Smith. Cross-references to material herein are prefixed by a "W"; cross-references to material in the textbook appear without the "W."

[‡] C. J. Gorter and H. B. G Casimir, *Physica*, **1**, 306 (1934).

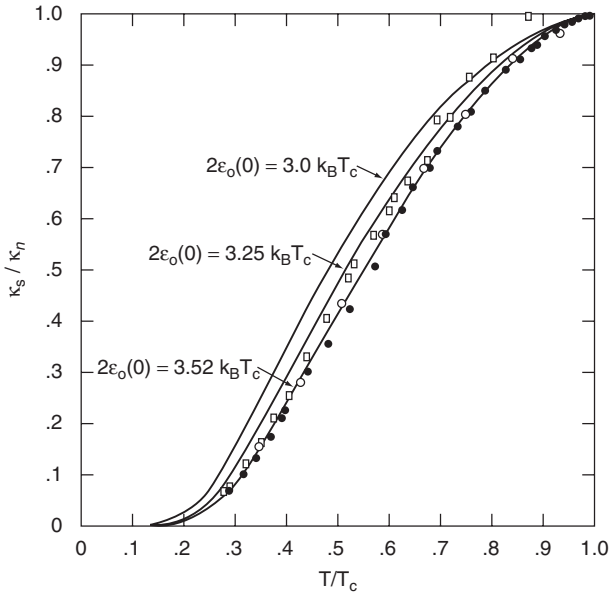

(a)

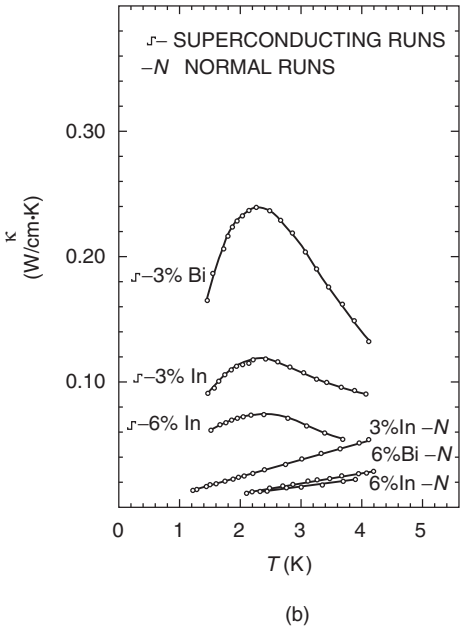

(b)

Figure W16.1. Thermal conductivity κ_s in the superconducting state and κ_n in the normal state. (*a*) The ratio κ_s/κ_n falls rapidly below unity for $T < T_c$ for the elemental superconductor Al. The solid curves represent the predictions of the BCS theory for various values of the superconducting energy gap in units of $k_B T_c$. (*b*) The quantity κ_s can be greater than κ_n below T_c, as illustrated for three superconducting alloys of Pb with In and Bi. [(*a*) From C. B. Satterthwaite, *Phys. Rev.*, **125**, 893 (1962). Copyright 1962 by the American Physical Society. (*b*) From P. Lindenfeld, *Phys. Rev. Lett.*, **6**, 613 (1961). Copyright 1961 by the American Physical Society.]

given as the sum of contributions from the superconducting and normal electrons by

$$G_s(T) = f_s(T)\left(-\frac{\mu_0 H_{c0}^2}{2}\right) + \sqrt{1 - f_s(T)}\left(-\frac{\gamma T^2}{2}\right). \tag{W16.1}$$

Here $-\mu_0 H_{c0}^2/2$ is the condensation energy per unit volume of the superconducting electrons relative to the normal state and $-\gamma T^2/2$ is the temperature-dependent part of the energy of the normal electrons. The parabolic dependence of the critical field $H_c(T)$ on T given in Eq. (16.6) can be shown to follow from this two-fluid expression for $G_s(T)$. It should be noted that while useful as a conceptual tool, the two-fluid model in this form cannot predict the observed exponential temperature dependence of the specific heat C_{es} as $T \to 0$ K.

W16.3 Superconducting Alloys of Metallic Elements

When alloys composed of superconducting elements such as Sn and In or Pb and Sn are prepared within the limits of their mutual solid solubility, the resulting single-phase superconductors also exhibit type I behavior as long as the electron mean free path l has not been decreased too much by the enhanced electron-impurity scattering present in the alloy. Further decreases in l result in an increase in the penetration depth λ and a decrease in the coherence length ξ until $\xi \approx l$ and $\kappa > 1/\sqrt{2}$. The alloy then becomes a type II superconductor.

The transition temperature T_c of such alloys typically decreases slowly, by 1 or 2%, when up to about 1 at % of alloying element is added, essentially independent of the host or the alloying element. It is believed that this is also a mean-free-path effect in which the decrease in l due to alloying eliminates the anisotropy of the energy gap present in the pure metal. Additional alloying beyond the level of ≈ 1 at % can lead to an increase or a decrease in T_c, depending on the nature of the host and alloying elements. When the alloying element possesses a magnetic moment (e.g., as for Fe or Mn), T_c is typically depressed to 0 K by only a few tens or hundreds of parts per million of the magnetic impurity.

Transition metal alloys are usually type II superconductors. In crystalline alloys of the $3d$, $4d$, and $5d$ transition metal elements such as the $4d$ alloys $Nb_{1-x}Zr_x$ and $Nb_{1-x}Mo_x$, it is observed that T_c has maxima for values of the average number z_{av} of valence electrons per atom near 4.7 and 6.5. This is at least partially an electron density-of-states effect since the electronic contribution to the alloy specific heat that is proportional to $\rho(E_F)$ also exhibits peaks for the same values of z_{av}. The BCS prediction of Eq. (16.27) indeed indicates that high T_c should be correlated with high $\rho(E_F)$, all other factors remaining constant. It is also interesting to note that lattice (i.e., structural) instabilities are observed in these alloys near the same electron concentrations where high T_c values are found. The BCC crystal structure is stable for $4.7 < z_{av} < 6.5$, while the HCP crystal structure is stable for both $z_{av} < 4.7$ and $z_{av} > 6.5$. From the BCS point of view it should not be surprising that electron density-of-states effects and lattice effects both influence T_c.

W16.4 Superconducting Intermetallic Compounds

Intermetallic compounds differ from metallic alloys in that they have well-defined compositions or limited ranges of composition. In addition, the elements present in a compound occupy specific, ordered sites in the unit cell instead of occupying random

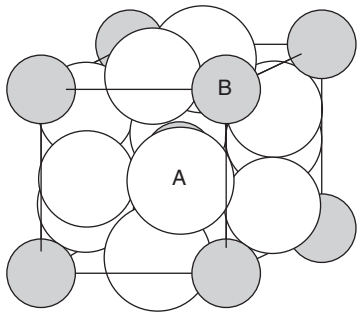

Figure W16.2. Cubic unit cell for the superconductors with the A15 crystal structure and the chemical formula A_3B. (From L. R. Testardi, *Rev. Mod. Phys.*, **47**, 637 (1975). Copyright 1975 by the American Physical Society.)

sites as in an alloy. For example, the two materials currently used in superconducting magnets, Nb_3Sn and $Nb_{0.36}Ti_{0.64}$, correspond to an intermetallic compound and a metallic alloy, respectively.

The A15 superconductors with the general formula A_3B (e.g., V_3Si, Nb_3Sn, Nb_3Ga, and Nb_3Ge) held the records for the highest T_c values from 1954 to 1986 when the discovery of the high-T_c cuprate superconductors occurred. The cubic crystal structure of these intermetallic compounds is shown in Fig. W16.2, where it can be seen that the B atoms occupy the sites of a BCC lattice. In this structure pairs of A atoms occupy adjacent sites in each of the six faces of the cubic unit cell, with three sets of nonintersecting linear chains of A atoms extending along the mutually perpendicular [100], [010], and [001] directions. Disorder in the chains due to deviations from the A_3B stoichiometry has been found to result in significant decreases in T_c.

Although there are at least 60 superconductors of the A_3B type, high T_c values are found only when the A atom is V, Nb, Mo, or Ta and the B atom is a metal such as Al, Ga, or Sn or a nonmetal such as Si or Ge. Thus the attainment of high T_c values is not strongly correlated with chemical bonding effects. Instead, the presence of a high density of states at the Fermi level associated with the exact A_3B stoichiometry is apparently necessary. The stoichiometric Nb-based compounds with B = Al, Ga, Si, and Ge are all metastable and are prepared by rapid quenching or other techniques. The highest T_c values are $T_c = 23.2$ K for Nb_3Ge and $T_c = 20.3$ K for Nb_3Ga. Specific heat and magnetic susceptibility studies have shown that Nb_3Ge and Nb_3Ga possess some of the highest values of $\rho(E_F)$ for the A15 superconductors. The normal-state properties of the A_3B compounds have also been studied widely to help understand the relatively high T_c values observed in these materials.

A list of some representative intermetallic compounds of different crystal structures, including several of the NaCl and A15 types, with T_c values near or greater than 10 K is presented in Table W16.1. This list serves to illustrate the extremely wide variety of materials and crystal structures in which superconductivity with $T_c \geq 10$ K is found. The superconducting AB compounds with the NaCl crystal structure form another important class of superconductors. The element A is typically a transition metal such as Nb, Mo, Ti, or Zr, while B is either C, N, O, or B. The highest T_c values are observed for those compounds with 9 or 10 valence electrons per formula unit (e.g., NbC or NbN and MoC, respectively).

TABLE W16.1 Transition Temperatures and Crystal Structures of Intermetallic Compound Superconductors

Superconductor	Structure Type[a]	T_c (K)
MoC	NaCl (FCC)	14.3
NbN_x[b]	NaCl (FCC)	17.3
PdH	NaCl (FCC)	9.5
PdD	NaCl (FCC)	11.6
HfV_2	$MgCu_2$, Laves (FCC)	9.4
$RhZr_2$	Al_2Cu (BCT)	11.3
V_3Si	UH_3, A15 (cubic)	17.1
Nb_3Sn	UH_3, A15 (cubic)	18.1
Nb_3Al	UH_3, A15 (cubic)	18
Nb_3Ga	UH_3, A15 (cubic)	20.3
Nb_3Ge	UH_3, A15 (cubic)	23.2
$LiTi_2O_4$	$MgAl_2O_4$, spinel (cubic)	13.7
YRh_4B_4	B_4CeCo_4 (tetragonal)	11.3
$LaMo_6Se_8$	$PbMo_6S_8$, Chevrel (trigonal)	11.4
YNi_2B_2C	— (tetragonal)	16.6

Source: Most data from D. R. Lide and H. P. R. Frederikse, eds., *CRC Handbook of Chemistry and Physics*, 75th ed., CRC Press, Boca Raton, Fla., 1994.

[a]The Bravais lattice is given in parentheses.

[b]The existence of nitrogen vacancies in NbN_x, with $x < 1$, allows T_c to be varied over a wide range. The T_c reported here is the highest known value for NbN_x.

The last entry, YNi_2B_2C, is a nonmagnetic member of the recently discovered family of rare earth nickel borocarbides (i.e., RNi_2B_2C, where R is a rare earth element). Superconducting members of this family include R = Y, Dy, Ho, Er, Tm, and Lu, of which Dy, Ho, Er, and Tm, and the R = Gd and Tb members undergo magnetic transitions to an antiferromagnetic state below a Néel temperature T_N. It is observed that $T_c > T_N$ for R = Ho, Er, Tm, and Lu, whereas the reverse is true for R = Dy. Study of these materials offers the opportunity of examining the interplay between magnetism and superconductivity.

W16.5 Further Discussion of Structure, Bonding, Composition, and Normal-State Properties of the Oxide-Based Ceramic Superconductors

The oxide $BaPb_{1-x}Bi_xO_3$ is superconducting for $0.05 < x < 0.3$ and can be considered to be the predecessor of the high-T_c cuprate superconductors discovered in 1986. For this mixed-valence material with a slightly distorted perovskite structure, the stoichiometric insulating $BaBiO_3$ compound with $x = 1$ can be represented by the formula $Ba^{2+}(Bi^{3+})_{0.5}(Bi^{5+})_{0.5}(O^{2-})_3$. When this oxide is doped with Pb^{4+} ions or when it is prepared in an oxygen-deficient form, the normally equal balance of closed-shell $Bi^{3+}(5d^{10}6s^2)$ and $Bi^{5+}(5d^{10})$ ions is disturbed and the concentration of electrons is modified. This material is semiconducting for $0.4 \leq x \leq 1$ and metallic for $x \leq 0.35$. By 1980, a T_c of 13 K had been achieved in this material for $x \approx 0.25$, corresponding to an electron concentration of about 3×10^{27} m^{-3}. This composition is actually closer to $BaPbO_3$, a metallic compound, than to the insulator $BaBiO_3$.

A related mixed-valence material that has the cubic perovskite structure for $x > 0.25$ is $Ba_{1-x}K_xBiO_{3-y}$, where $T_c \approx 30$ K has recently been achieved for $x \approx 0.4$. The charge carriers in this material have been shown to be electrons occupying a less than half-filled energy band. Although the K^+ ions donate one less electron to the structure than the Ba^{2+} ions they replace, the result of the doping is an electron-deficient metal rather than a metal in which the charge carriers are holes. The insulator $BaBiO_3$ can thus be transformed into a metallic superconductor either by doping with Pb on the Bi sites or with K on the Ba sites. The latter method is clearly more effective for obtaining higher T_c values.

Three of the superconductors shown in Fig. 16.17 are now described in more detail.

$La_{2-x}Sr_xCuO_4$ (LSCO). The stoichiometric compound La_2CuO_4 with nominal ionic charges La^{3+}, Cu^{2+}, and O^{2-} is an antiferromagnetic insulator with a Néel temperature $T_N = 340$ K. The Cu^{2+} ions have magnetic moments $m \approx 0.5\ \mu_B$. This compound becomes superconducting when doped with divalent ions such as Sr^{2+} or Ba^{2+} which replace some of the La^{3+} ions (e.g., $La_{2-x}Sr_xCuO_4$) or when doped with excess oxygen which enters the LaO layers as O^{2-} ions (e.g., La_2CuO_{4-y} with $y < 0$). Both types of doping result in the introduction of holes into the CuO_2 layers through the removal of electrons. In the first case, one of the electrons normally contributed by each La^{3+} ion to these layers is now no longer available. If an Sr^{2+} ion simply replaces a La^{3+} ion (similar to B^{3+} replacing Si^{4+} in crystalline Si) with no other changes taking place, hole doping will occur, an electron will be missing from some type of chemical "bond," and ionic charge neutrality will be violated. But if $Cu^{2+} \rightarrow Cu^{3+}$ in order to maintain ionic charge compensation, all the bonds will be satisfied and the hole will instead be present in the $3d$ shell of the Cu^{3+} ion. The related compound $Nd_{2-x}Ce_xCuO_4$ is an electron-type superconductor when doped with Ce^{4+} ions since each Ce^{4+} contributes an additional electron to the CuO_2 planes.

When doped at the level x greater than about 0.05, enough holes are introduced into the CuO_2 planes so that $La_{2-x}Sr_xCuO_4$ becomes a metal. It also becomes a superconductor whose highest $T_c \approx 40$ K is observed at the optimum doping level of $x \approx 0.16$. This is illustrated in the phase diagram for $La_{2-x}Sr_xCuO_4$ shown in Fig. 16.18. Notice the similarity of this phase diagram to that of $YBa_2Cu_3O_{7-x}$ given in the same figure. Regions where $La_{2-x}Sr_xCuO_4$ is an orthorhombic antiferromagnetic insulator and an orthorhombic or tetragonal metal are indicated.

As can be seen in Fig. 16.17, each CuO_2 layer in the La_2CuO_4 structure is separated from adjacent CuO_2 layers by pairs of LaO layers. This corresponds to a greater separation between CuO_2 planes than is found in $YBa_2Cu_3O_7$ and in the other cuprate superconductors where the CuO_2 planes are clustered in groups of two or three and are separated from each other only by single planes containing Y^{3+} or Ca^{2+} ions.

$YBa_2Cu_3O_{7-x}$ (YBCO). The orthorhombic unit cell of the $YBa_2Cu_3O_7$ structure is shown in Fig. W16.3 and the stacking sequence of the layers is shown in Fig. W16.4. It can be seen that the two CuO_2 layers in the unit cell are slightly puckered, while the CuO layer containing the linear $\ldots$CuOCuO$\ldots$ chains, taken to lie along the b axis, is planar. $YBa_2Cu_3O_7$ can be considered to be oxygen deficient in the sense that two oxygen atoms would appear to be missing from the hypothetical compound $YBa_2Cu_3O_9 = (YCuO_3)(BaCuO_3)_2$, which has the nominal perovskite stoichiometry. There are actually only eight possible oxygen sites in the unit cell, and one of these

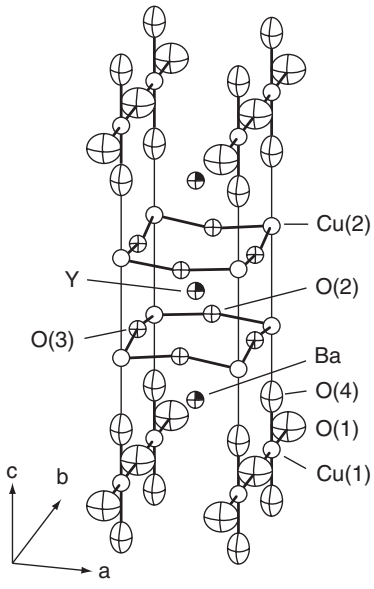

Figure W16.3. Orthorhombic unit cell of the $YBa_2Cu_3O_7$ structure. (From J. D. Jorgensen et al., *Phys. Rev. B*, **36**, 3608 (1987). Copyright 1987 by the American Physical Society.)

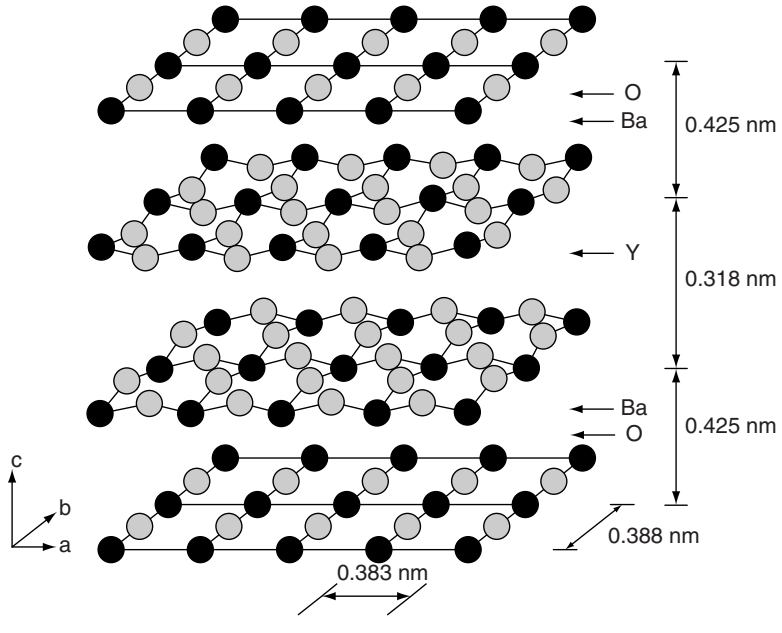

Figure W16.4. Stacking sequence of the layers parallel to the *c* axis in the $YBa_2Cu_3O_7$ structure. (From C. P. Poole, Jr., et al., *Copper Oxide Superconductors*, copyright 1988, John Wiley & Sons, Inc. Reprinted by permission of John Wiley & Sons, Inc.)

sites, in the layer with the CuO chains, is always vacant. Thus $YBa_2Cu_3O_7$ is, in fact, the correct chemical formula for this compound.

The $YBa_2Cu_3O_7$ structure differs from the other structures found in the high-T_c cuprate materials as follows:

1. In addition to the CuO_2 layers containing Cu ions with four NN O ions, there exist CuO layers consisting of CuO chains in which each Cu ion has two NN O ions in the layer and also two next-NN O ions just above and below it in the BaO layers at a distance of ≈ 0.18 nm. One half of the possible oxygen sites in this CuO layer are vacant, with the filled oxygen sites ordered along the *b* axis.
2. Overall ionic charge neutrality is maintained only if Cu^{3+} ions and/or oxygen vacancies are present in the structure. An alternative point of view is that ionic charge neutrality is in fact not required and that instead there are mobile holes in some of the copper–oxygen layers, as is discussed later.

The chemical bonding in $YBa_2Cu_3O_7$ is almost completely ionic for the Y^{3+} and Ba^{2+} ions but is of a mixed ionic–covalent type in the copper–oxygen layers. The interaction between the Y^{3+} and Ba^{2+} ions and the ions in the neighboring copper–oxygen layers is very weak. Thus the layers containing Y^{3+} and Ba^{2+} are insulating and the charge carriers are confined to the conducting copper–oxygen layers.

As mentioned earlier, if overall ionic charge neutrality were required within the $YBa_2Cu_3O_7$ formula unit with the assumed ionic charge states Y^{3+}, Ba^{2+}, and O^{2-}, the three Cu ions could have the following ionic charge states: Cu^{2+}, Cu^{2+}, and Cu^{3+} (i.e., one of the three Cu ions per formula unit would be trivalent). But requiring overall neutrality for ionic charge would mean that no delocalized charge carriers are present and $YBa_2Cu_3O_7$ would be an insulator. For $YBa_2Cu_3O_7$ to be a metallic conductor, the Fermi energy must lie within a partially filled energy band. This would result if all the Cu ions were actually in the Cu^{2+} charge state, resulting in one bonding electron per formula unit missing from the CuO_2 layers. This is equivalent to the point of view that there is one mobile hole per formula unit in the CuO_2 layers. In fact, it is not clear where the hole is present: on the Cu or O ions, in the CuO_2 layers, or in the CuO chains. If the Cu^{3+} ion is present instead, the hole would appear in the partially filled $3d$ shell of this ion.

There are at least two different ways to understand the presence of mobile holes in the stoichiometric $YBa_2Cu_3O_7$ compound in terms of chemical bonding arguments. According to a strictly ionic or *formal charge* viewpoint, if the charge states of the ions are assumed to be Y^{3+}, Ba^{2+}, Cu^{2+}, and O^{2-}, the net ionic charge per $YBa_2Cu_3O_7$ formula unit is $q_{\text{ion}} = +3e + 2(+2e) + 3(+2e) + 7(-2e) = +13e - 14e = -e$. Overall charge neutrality in the material could then be maintained by the presence of one hole with charge $+e$ per formula unit in the CuO_2 layers. From the alternative, covalent bonding point of view each of the four oxygen ions in the CuO_2 layers is assumed to have an ionic charge of $+2e$ (instead of $-2e$) and to contribute two electrons to the covalent bonds that it forms with its neighboring Cu^{2+} ions. According to this covalent point of view, each formula unit of $YBa_2Cu_3O_7$ has only 15 electrons available for bonding in the two CuO_2 layers, including three from the Y^{3+} ion, instead of the 16 required for the eight covalent bonds present. There is again one hole per formula unit present in the CuO_2 layers. Since the actual bonding

in the copper–oxygen layers is of a mixed ionic–covalent type, the true picture must lie somewhere between the ionic and covalent limits just described.

If oxygen vacancies are present in the material, as indicated by the formula $YBa_2Cu_3O_{7-x}$ with $x > 0$, then either fewer than one-third of the Cu ions would have to be in the +3 charge state in order to preserve ionic charge neutrality, or there would be fewer holes in the CuO_2 layers. If the oxygen vacancies occur in the CuO chains, corresponding to the formula $Y(BaO)_2(CuO_2)_2CuO_{1-x}$, the Cu^{2+} ions in the chains could donate electrons to the CuO_2 layers, thereby removing holes and causing a reduction in T_c.

The phase diagram for $YBa_2Cu_3O_{7-x}$ is shown in Fig. 16.18*b*. The physical properties of this material can be seen to be extremely sensitive to the oxygen stoichiometry, with structural and metal–insulator transitions along with rapid changes in both T_N and T_c occurring as x is varied. Note that $YBa_2Cu_3O_{7-x}$ becomes tetragonal and semiconducting for $x > 0.65$.

$HgBa_2Ca_2Cu_3O_8$ (HBCCO or Hg-1223). The current record for the highest known T_c, 135 K, is held by the $n = 2$ or Hg-1223 member of the $HgBa_2Ca_nCu_{n+1}O_{2n+4}$ family of compounds. For this family T_c increases with the number $(n + 1)$ of CuO_2 layers per unit cell (see Table 16.5). The unit cell of the $n = 1$ or Hg-1212 compound with $T_c = 128$ K is shown in Fig. W16.5. The excess oxygen that is apparently necessary for the superconductivity of $HgBa_2Ca_2Cu_3O_{8+x}$ resides in the Hg layers. The hole doping of the CuO_2 layers therefore originates from the Hg layer. Problems with control of composition have been found in this material due to loss of Hg during high-temperature processing.

Normal-State Properties. To obtain an understanding of the origins of the high-T_c superconductivity in the cuprates, it is first necessary to understand why they are

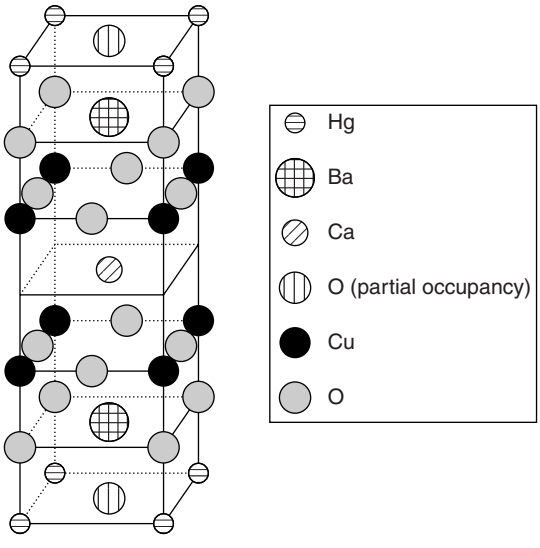

Figure W16.5. Tetragonal unit cell of the $n = 1$ or Hg-1212 member of the $HgBa_2Ca_nCu_{n+1}O_{2n+4}$ series of compounds with $T_c = 128$ K. (Reprinted from R.L. Meng et al., Physica **C214**, 307 (1993), copyright 1993, with permission from Elsevier Science.)

metallic conductors and not insulators in the normal state. Two viewpoints are possible: Chemical bonding effects lead to the existence of mobile charge carriers or the delocalization of the charge carriers can be understood as resulting from the particular electronic band structure of the material. Both points of view are useful and can provide important insights into the existence of the normal-state metallic behavior. Extrinsic effects such as doping can also play an important role in determining the conductivity of these materials in the normal state.

In the normal state above T_c, the cuprate materials are not typical metals and are not very good conductors of electricity. In addition, the electronic contribution to the specific heat in these materials is rather high, about a factor of 10 greater than that of simple metals such as Na or Cu. This latter result is attributed to the high effective masses of the carriers in high-T_c materials. The normal-state properties of these materials are strongly anisotropic, due to their tetragonal or orthorhombic crystal structures. Another unusual property of the high-T_c materials is that their electrical resistivities vary linearly with temperature above T_c.

From a covalent point of view, the chemical bonding between the Cu and O atoms in the copper–oxygen layers makes use of the s, p_x, p_y, and $d_{x^2-y^2}$ atomic orbitals of the $Cu^{2+}(3d^9)$ ions and the p_x and p_y atomic orbitals of the filled-shell O^{2-} $(2s^2 2p^6)$ ions, as shown in Fig. W16.6. These four atomic orbitals on Cu atoms hybridize to form square-planar dsp^2 hybrid orbitals which then overlap, that is, interact with the p_x and p_y atomic orbitals on adjacent O atoms (see Section W2.1 for a description of these atomic and hybrid orbitals). These interactions can then lead to the formation of σ-type molecular orbitals or chemical bonds which in the cuprate superconductors are actually of a mixed ionic–covalent nature due to the different electronegativities of the Cu and O atoms involved. It is clear that occupation of all four dsp^2 orbitals associated with the Cu^{2+} ion requires that two additional electrons be donated by other ions in the structure, such as Y^{3+} and Ca^{2+}. The electrons in these bonds form the valence energy bands of the material, which lie below the Fermi energy. From molecular orbital theory it appears that the states at E_F in $YBa_2Cu_3O_7$ will be antibonding orbitals of the Cu $d_{x^2-y^2}$ type. Most high-T_c cuprates display hole-type conduction in a conduction band that is nearly half full.

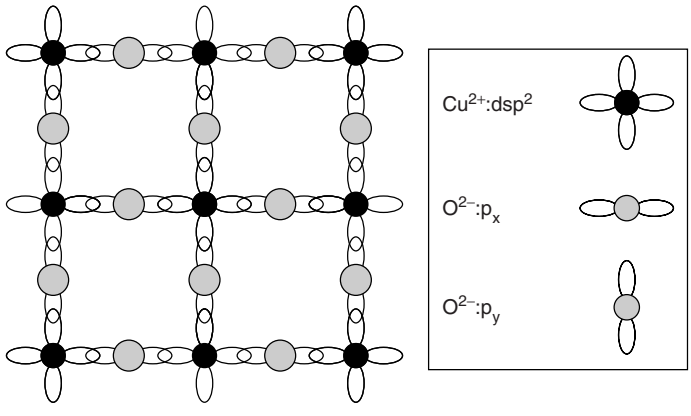

Figure W16.6. Chemical bonding between the Cu and O atoms in the copper–oxygen layers illustrated using the atomic orbitals involved: the square-planar dsp^2 hybrid orbitals of the Cu atoms and the p_x and p_y orbitals of the O atoms.

Rather than using the extended Bloch wavefunctions which are appropriate in good metals, the highly correlated nature of the electrons or holes in the copper–oxygen planes is often treated using tight-binding Hubbard models of the type used to describe the behavior of electrons associated with magnetic ions, as discussed in Chapter W9. The tight-binding approximation in two dimensions is applied to the Cu–O planes in Section 7.9. The goal of these models is to predict the occupancy by a pair of electrons of the orbitals on two adjacent sites. The effects of electrons hopping between the sites and of Coulomb repulsion between two electrons on a given site are the essential ingredients of these tight-binding models. It is possible that the important aspects of the high-T_c cuprate superconductivity can be understood in terms of the t–J version of the Hubbard model. Here t is the tunneling or hopping matrix element, J the exchange energy parameter given by $J = t^2/U$, and U the Coulomb repulsion energy for two electrons on the same site. In the limit $U \to 0$, the material will be a metal, while for $U \gg t$, the material will be an insulator with one electron localized on each site. The electrons in the high-T_c materials are *strongly correlated* because U is significantly greater than the average kinetic energy of the electrons at E_F. These strong correlations can induce both localized magnetic moments, which may undergo antiferromagnetic ordering and also localized electronic states leading to insulating behavior. An alternative approach to this problem is the *resonant valence bond* (RVB) model, in which the ground state corresponds to the usual chemical bonds in the copper–oxygen planes.

Calculations of the energy bands based on the three-state Hubbard model appropriate for the copper atom and two oxygen atoms per unit cell show that as a function of hole doping into the CuO_2 layers, peaks in the electronic density of states at E_F can lead to high T_c values. In addition, energy-band-structure calculations for these high-T_c materials have successfully predicted the observed anisotropy of the electrical conductivity and have provided useful information concerning the distribution of charge, thereby helping to clarify the chemical bonding present. Band-structure calculations predict that the electronic states in the vicinity of E_F are associated with the bonding orbitals in the copper–oxygen layers, which originate from the $Cu^{2+} d_{x^2-y^2}$ and the $O^{2-} p_x$ and p_y atomic orbitals.

Metal–insulator (MI) *transitions* can also appear within the framework of the Hubbard models as electrons are added to the energy bands. Metallic or conducting behavior will occur when E_F lies in a partially filled energy band. When E_F is nearer the top of an energy band and when there are unoccupied regions of the relevant Brillouin zone outside the Fermi surface, hole-type conduction can dominate the electrical behavior. MI transitions are indeed observed in the normal state of the high-T_c materials, such as $La_{2-x}Sr_xCuO_{4-y}$, as the composition changes. This material is an antiferromagnetic insulator with $T_N \approx 340$ K when undoped (i.e., for $x = 0$ and $y \geq 0$) and is metallic when doped (i.e., for $y = 0$ and $x > 0.05$; see Fig. 16.18).

All the high-T_c cuprate materials exhibit antiferromagnetic ordering in their insulating phases, which results from interactions between the Cu ($3d^9$) magnetic moments within the CuO_2 layers. The interaction responsible for the ordering is the indirect superexchange mechanism involving the copper $ds p^2$ hybrid orbitals and the oxygen p orbitals. The long-range order along the c axis is controlled by the much weaker interlayer coupling of the magnetic moments. The Néel temperature T_N decreases rapidly as doping increases and the metallic phase is approached. The incompatibility of the magnetic with the metallic phase occurs because the localized $3d$ electrons involved in the long-range magnetic order interact strongly with the delocalized charge carriers. As a result, the directions

of the magnetic moments of the localized $3d$ electrons fluctuate rapidly, destroying the antiferromagnetic long-range order. Short-range antiferromagnetic order can still exist below T_c, however. Phase diagrams showing the dependencies of structure and of T_c and T_N on the compositional parameter x are shown in Fig. 16.18 for $La_{2-x}Sr_xCuO_{4-y}$ and $YBa_2Cu_3O_{7-x}$. Note that $YBa_2Cu_3O_{7-x}$ is superconducting for x less than about 0.6 and is a semiconductor for $0.6 < x < 1$. The oxygen content determines both the hole concentration of this material and the shape of the Fermi surface. The Cu ions in YBCO apparently have local moments $m \approx 0.3\ \mu_B$ in the normal state above T_c.

Measurements of the Hall effect in the normal state of high-T_c materials have provided useful information on the signs and concentrations of the charge carriers, and, in conjunction with measurements of the electrical conductivity, have also helped to determine the charge carrier mobilities. These Hall effect studies have identified holes as the majority carriers in most high-T_c materials. The concentration of holes is observed to increase with increasing T and with doping (e.g., replacement of La^{3+} by Sr^{2+} in La_2CuO_4). In $La_{1.9}Sr_{0.1}CuO_4$ with $T_c \approx 35$ K, the hole concentration is $\approx 1 \times 10^{27}$ m^{-3}, at least a factor of 10 lower than that found in typical metals. This corresponds to about 0.1 hole per Cu atom, as expected from the Sr fraction. Hall effect studies in $YBa_2Cu_3O_{7-x}$ also identify holes as the charge carriers, with concentrations that decrease as x increases (i.e., as more O vacancies are present in the material).

The electrical resistivities of the high-T_c materials in their normal states are observed to have temperature dependencies of the form

$$\rho(T) = A + BT. \tag{W16.2}$$

This behavior is unusual since in conventional metals, $\rho(T) = A + BT^n$ with $n \approx 5$ as $T \to 0$ K. To illustrate this behavior, the measured resistivities for $YBa_2Cu_3O_7$ along the a, b, and c axes are presented in Fig. W16.7. The normal-state electrical

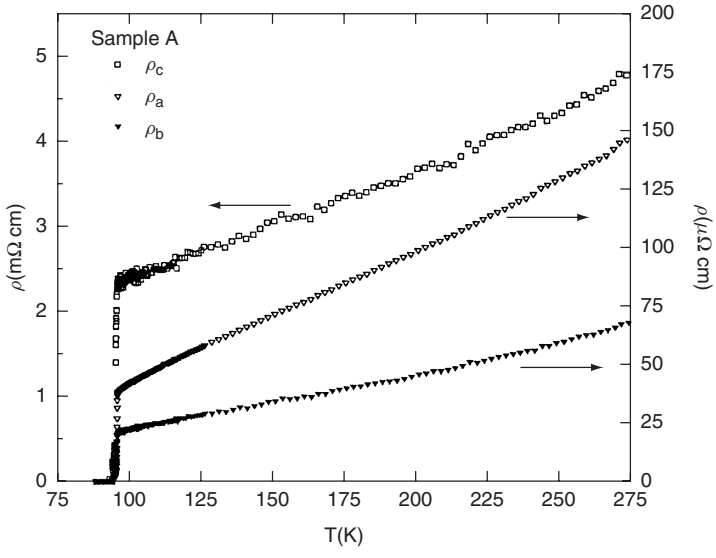

Figure W16.7. Measured electrical resistivities for $YBa_2Cu_3O_7$ along the a, b, and c axes. [From T. A. Friedmann et al., *Phys. Rev. B*, **42**, 6217 (1990). Copyright 1990 by the American Physical Society.]

resistivity of $YBa_2Cu_3O_7$ can be seen to be quite anisotropic, with the resistivity ρ_c perpendicular to the *ab* planes a factor of up to 150 times greater than the in-plane resistivities ρ_a and ρ_b. This behavior is consistent with the effective mass m_c^* for the motion of charge carriers along the *c* axis being much greater than m_a^* and m_b^* for motion in the *ab* plane. Evidence for localization of the charge carriers along the *c* axis has been found in some samples (i.e., ρ_c increases as T decreases). The lowest resistivity is found along the *b* axis, the axis of the Cu–O chains in the CuO planes, indicating that the Cu–O chains do contribute to the electrical conductivity in this material.

The temperature dependence of the resistivity of thin films of $DyBa_2Cu_3O_{7-x}$ as a function of x is shown in Fig. W16.8. The transition from semiconducting to metallic behavior can be observed as the concentration of oxygen vacancies decreases to zero. It should be noted that the replacement of Y by the rare earth atom Dy has essentially no effect on the superconducting or normal-state properties of this material.

Very similar values of the coefficient in Eq. (W16.2) of the linear term in $\rho_a(T)$ or $\rho_b(T)$ are found for most of the cuprate materials above their T_c values, indicating that the CuO_2 layers may exhibit a type of universal normal-state behavior in these materials.

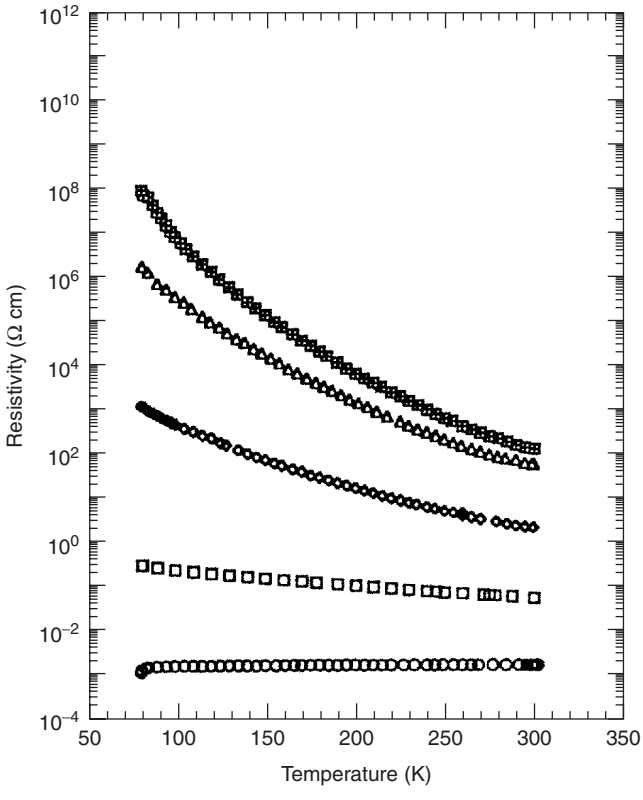

Figure W16.8. Temperature dependence of the resistivity of thin films of $DyBa_2Cu_3O_{7-x}$. The resistivity increases as x increases. The transition from semiconducting to metallic behavior occurs as the concentration of oxygen vacancies decreases. [From G. Yu et al., *Phys. Rev. B*, **45**, 4964 (1992). Copyright 1992 by the American Physical Society.]

W16.6 Further Discussion of Superconducting-State Properties of the Oxide-Based Ceramic Superconductors

An important property of the high-T_c cuprate superconductors is the strongly anisotropic nature of the superconductivity which results from the anisotropic tetragonal or orthorhombic structures of these materials. With the obvious exception of the transition temperature T_c, all the superconducting properties (i.e., critical fields and critical currents, superconducting energy gaps, penetration depths, coherence lengths, etc.) have values that are the same (or nearly the same) in the *ab* plane but which differ considerably from the corresponding values along the *c* axis. These anisotropies result from the anisotropic structure and effective masses m^* of the charge carriers in the normal state, with $m_c^*/m_a^* \approx 30$ in $YBa_2Cu_3O_7$. Even-higher effective-mass anisotropies are observed in the BSCCO and TBCCO families.

Since $\lambda \propto (m^*)^{1/2}$ [Eq. (16.10)] and $\xi \propto v_F \propto (m^*)^{-1/2}$ [Eq. (16.32)], the following inequalities can be expected to apply in high-T_c superconductors where $\xi \ll \lambda$ and $m_c^* \gg m_a^*$:

$$\lambda_c > \lambda_{ab} \gg \xi_{ab} > \xi_c, \tag{W16.3a}$$

$$\kappa_c \gg \kappa_{ab} \gg 1. \tag{W16.3b}$$

These predictions are consistent with the following results obtained for $YBa_2Cu_3O_7$:

$$\lambda_c \approx 500 \text{ nm} > \lambda_{ab} \approx 100 \text{ nm} \gg \xi_{ab} \approx 3 \text{ nm} > \xi_c \approx 0.5 \text{ nm} \tag{W16.4}$$

as well as the observed extreme type II behavior. The clean limit ordinarily applies to $YBa_2Cu_3O_7$ since the electron mean free path $l \approx 10$ nm is much greater than ξ_{ab} or ξ_c. As a result of this anisotropy, the cores of vortices will be circular when **H** is applied along the *c* axis and elliptical when **H** is applied parallel to the *ab* plane. In the mixed state with **H** applied along the *c* axis, the vortices are no longer continuous flux tubes but are proposed to be individual "pancake" vortices in a given CuO_2 layer which are only weakly coupled to each other through the intervening, nonsuperconducting layers. In addition, the low values of the coherence lengths ξ imply that the properties of these superconductors will be quite sensitive to deviations from chemical and structural uniformity.

Using the Ginzburg–Landau prediction that $H_{c2}(i) \propto \Phi_0/\xi_j\xi_k$, it can be shown that

$$\frac{H_{c2}(c)}{H_{c2}(ab)} = \sqrt{\frac{m_{ab}^*}{m_c^*}} \ll 1. \tag{W16.5}$$

Thus the upper critical field $H_{c2}(c)$ for H applied along the *c* axis in anisotropic superconductors such as $YBa_2Cu_3O_7$, where $m_c^* \gg m_a^*$ or m_b^* is predicted to be much less than the in-plane critical field $H_{c2}(ab)$. This is indeed observed to be the case for $YBa_2Cu_3O_7$, where it is found that $B_{c2}(c) = \mu_0 H_{c2}(c) \approx 20$ T, while $B_{c2}(ab) = \mu_0 H_{c2}(ab) \approx 70$ T at $T = 77$ K. The critical transport currents J_c in the high-T_c superconductors are also quite anisotropic, with the values of J_c parallel to the *ab* planes typically 10 times greater than J_c parallel to the *c* axis (see Table W16.2). Apparently, superconducting currents can flow along both the copper–oxygen layers and chains in $YBa_2Cu_3O_{7-x}$.

The superconducting energy gaps of the high-T_c superconductors are also observed to be quite anisotropic, with $2\varepsilon_{ab}(0) \approx$ (6 to 8) $k_B T_c$ and $2\varepsilon_c(0) \approx$ (2 to 4) $k_B T_c$. The energy gap in $YBa_2Cu_3O_7$ as measured by infrared reflectivity is quite anisotropic, with $2\varepsilon_{ab}(0) \approx 8k_B T_c$ and $2\varepsilon_c(0) \approx 3.5k_B T_c$, the latter being in good agreement with the weak-coupling BCS prediction and the former giving evidence for strong-coupling behavior. Electron tunneling studies tend to give a lower value for the $2\varepsilon_{ab}(0)$ gap, which is, however, still well above the BCS prediction of $3.52k_B T_c$.

The microwave surface resistance R_s of $YBa_2Cu_3O_{7-x}$ just below T_c shows evidence for an energy gap of magnitude $2\varepsilon(0) \approx 8k_B T_c$. Below $T_c/2$, however, the measured R_s is much higher than would be predicted by BCS on the basis of an energy gap of this size. These enhanced losses at lower T are due to unpaired charge carriers which are present due either to a much smaller energy gap or to the absence of a true gap (i.e., gapless superconductivity). It has been suggested that these may be carriers residing in the Cu–O chains. This "gapless" behavior is enhanced in oxygen-deficient samples with $x > 0$. An additional source of microwave losses in some samples could be weak links between the superconducting grains.

It is found in the high-T_c superconductors that ξ_c is comparable to the typical spacing between adjacent superconducting CuO_2 layers within a given unit cell and less than the distance between groups of CuO_2 layers in adjacent unit cells. Thus the CuO_2 layers are expected to be only weakly coupled to each other. The $HgBa_2Ca_1Cu_2O_6$ structure shown in Fig. W16.5, for example, has two CuO_2 layers within each unit cell which are separated from each other by Ca^{2+} layers and from the CuO_2 layers in adjacent unit cells by the BaO and Hg^{2+} layers.

The roles that the different layers or sites play in the high-T_c materials is illustrated by the effects that magnetic ions have on the superconductivity when they are introduced into the structure. Magnetic rare earth ions on the Y site in YBCO do not affect the superconductivity even if they order antiferromagnetically below T_c. The $3d$ magnetic ions on the Cu ion site destroy superconductivity, however, because they interact much more strongly with the superconducting electrons or holes.

While results of specific-heat studies show a jump at T_c, it has not been possible to check the BCS weak-coupling prediction that $C_{es}(T_c) - C_{en}(T_c) = 1.43\gamma T_c$, due to the inability to obtain reliable values for γ. Indeed, since H_{c2} is so large for these materials, it has not been possible to return to the normal state at sufficiently low T where the γT term could be extracted reliably from the measured specific heat. In the cuprates the phonon T^3 contribution to the specific heat dominates over the electron γT linear term at T_c. This behavior is opposite to that observed for relatively low-T_c superconductors such as Sn, Pb, and Nb.

W16.7 Unusual Superconductors

The wide variety of materials that become superconducting is further illustrated by several materials that may be considered to be unusual, not necessarily because the mechanism responsible for superconductivity is no longer the BCS indirect electron–phonon mechanism but because the existence or some aspect of the superconductivity is unexpected or unusual. Several examples are described next.

Intercalated Graphite. When K atoms are chemically inserted (i.e., *intercalated*) between the atomic planes of crystalline graphite, stoichiometric crystalline compounds

such as KC_8 can be obtained which are superconductors even though neither of the components (i.e., semimetallic graphite or metallic K) are themselves superconductors. The compound KC_8 retains the structure of graphite but with regular planar arrays of K atoms present which are separated along the c axis by single planes of C atoms. The superconductivity of KC_8 with $T_c \approx 0.39$ K apparently arises from the interactions between the electrons provided by the "donor" K atoms and the phonons of the planar graphite structure.

Doped Fullerites. In the solid state the C_{60} molecules known as *buckminsterfullerene*, as *fullerene*, or simply as *buckyballs* possess a three-dimensional FCC crystal structure known as *fullerite*. When the two tetrahedral and one octahedral vacant interstitial sites per C_{60} molecule in the FCC structure are occupied by alkali metal atoms such as K, the insulating C_{60} solid becomes a conductor and superconductivity is observed. These doped fullerites are known as *fullerides*. It has been observed that K_3C_{60} has $T_c = 19$ K, while a T_c value as high as 47 K has been found in Cs_3C_{60}. As in intercalated graphite (e.g., KC_8), the dopant alkali K^+ ions in solid K_3C_{60} provide the conduction electrons, while the C_{60} molecular structure provides both the necessary energy levels corresponding to extended or metallic electronic states and the phonons that are needed for the occurrence of superconductivity, assuming that the BCS indirect electron–phonon mechanism is operative.

Si and Ge Under Pressure. When Si and Ge are placed under pressures of about 120 atm, they undergo transformations to more highly coordinated metallic structures in which each atom has more than four NNs. In this metallic state they become superconducting at $T_c(\text{Si}) \approx 6.7$ K and $T_c(\text{Ge}) \approx 5.3$ K. Note that metallic Sn and Pb from the same column of the periodic table are conventional superconductors with $T_c = 3.7$ K and 7.2 K, respectively. Other normally nonmetallic elements which become superconducting due to phase transitions which occur under pressure include the group V elements P, As, Sb, and Bi and the group VI elements S, Se, and Te.

Heavy-Fermion Systems. There exist intermetallic compounds and metallic alloys in which the electronic contributions to the specific heat and to the Pauli paramagnetic susceptibility can be anomalously large, by about a factor of 100 above the predictions of the free-electron model. These anomalies can also occur for the rare earth elements, as described in Section 12.4, and are generally attributed to a strong, narrow peak in the density of electron states at E_F. Since $\rho(E_F)$ is proportional to the band-structure effective mass m^* of the electrons, these materials are usually called *heavy-fermion* or *heavy-electron systems*. When superconducting, these materials have relatively low T_c values: for example, $T_c = 0.43$ K for UPt_3, 0.6 K for $CeCu_2Si_2$, and 1.3 K for URu_2Si_2. In this sense these materials differ dramatically from essentially all other superconductors where a high electronic specific-heat coefficient γ is usually correlated with a high T_c value (see Fig. 16.19). These heavy-fermion systems often undergo antiferromagnetic ordering of the $4f$ or $5f$ magnetic moments at the Néel temperature T_N, which lies above the corresponding superconducting T_c.

A common component of these systems is an element with an unfilled f shell (e.g., the rare earth Ce or the actinide U with $4f^2$ and $5f^3$ electron configurations, respectively). These $4f$ or $5f$ electrons apparently hybridize or mix strongly with the conduction electrons, resulting in a narrow energy band that overlaps the Fermi

energy of the material. The mechanism for superconductivity in these heavy-fermion systems has not yet been identified. It is possible that the indirect electron–phonon BCS mechanism does not apply.

Charge-Transfer Organic Solids. Some unusual charge-transfer compounds composed of organic molecular *electron-donor* ions such as BEDT-TTF$^+$ (ET for short; $[C_2S_2C_2S_2(CH_3)_2]_2^+$) and inorganic *electron-acceptor* ions such as $Cu(NCS)_2^-$ are highly conducting materials that can become superconducting at temperatures as high as $T_c = 10$ K. The properties of these charge-transfer organic superconductors are usually highly anisotropic. They exhibit nearly one- or two-dimensional conducting behavior, due to the presence in the structures of stacked planar aromatic rings connected by π bonds. In this sense there are some interesting similarities between these materials and the high-T_c cuprate superconductors.

W16.8 Further Discussion of Critical Currents

The critical transport current density J_c in the mixed state of a type II superconductor will be the current for which the Lorentz forces exceed the average *pinning* forces that tend to prevent vortex motion. Thermal *depinning* of vortices can also lead to vortex motion and hence losses. This will be especially important in the high-T_c materials where the available thermal energy k_BT can exceed the depth of the typical pinning potential well. The introduction of defects such as dislocations in a cold-worked material can lead to significant increases in the critical current without at the same time affecting the upper critical field H_{c2}. The introduction of defects corresponding to a certain size, type, and concentration of pinning center can be carried out through a variety of techniques, including irradiation with protons or neutrons. The development of superconducting materials with sufficiently strong pinning forces to allow the attainment of high current densities in the presence of high magnetic fields is an area of great current interest.

Some typical values of critical transport current densities J_c for superconductors of technological importance are given in Table W16.2. Also specified are the temperature and applied magnetic field at which J_c was measured. In the case of an applied field, the direction of current flow is perpendicular to the direction of **H**.

It can be seen from Table W16.2 that the highest critical currents in $YBa_2Cu_3O_7$ are found in thin films rather than in single crystals. Apparently, the films contain more pinning centers than do the single crystals. For the single crystals, J_c can be increased by a factor of about 100 through neutron or proton irradiation. Oxygen vacancies in $YBa_2Cu_3O_{7-x}$ may be the most important pinning centers. Grain boundaries between neighboring $YBa_2Cu_3O_7$ crystallites which are at low angles with respect to the CuO_2 planes are necessary for the achievement of high critical current densities since high-angle grain boundaries can act as weak links between the grains. It can also be seen that for a given superconductor, J_c decreases with increasing T and also with increasing applied external H. This temperature dependence for J_c is consistent with the prediction of the G-L theory that

$$J_c(T) = H_c(T)/\lambda(T). \tag{W16.6}$$

This critical current density is essentially equal to the depairing current density determined by equating the kinetic energy density of the current-carrying electrons to the

TABLE W16.2 Critical Current Densities J_c for Superconductors of Technological Importance

Superconductor	T (K)	J_c (MA/cm^2)	$B = \mu_0 H$ (T)	Comments
$Nb_{0.36}Ti_{0.64}$	4.2	0.37	5	Filament
Nb_3Sn	4.2	>0.1	12	Filament
$YBa_2Cu_3O_{7-x}$	5	1.4	0–1	Single crystal, $B \perp ab$ plane
	77	0.01	0.1	Single crystal, $B \perp ab$ plane
	77	0.0043	1	Single crystal, $B \perp ab$ plane
	4.2	60	0	Epitaxial film
	4.2	40	8	Epitaxial film, B in ab plane
	4.2	6	8	Epitaxial film, $B \perp ab$ plane
	4	1300	0	Epitaxial film, 500 nm thick
	77	1	0	1 to 2-μm films on metal tapes
	77	0.1	5	1 to 2-μm films on metal tapes
$Bi_2Sr_2CaCu_2O_8$	4.2	0.17	30	Filaments in Ag-sheathed tape
$Bi_{2-x}Pb_xSr_2Ca_2Cu_3O_{10}$	4.2	0.1	25	Filaments in Ag-sheathed tape
	77	0.05	0	Filaments in Ag-sheathed tape

Source: Data collected from various sources, including C. P. Poole, Jr., H. A. Farach, and R. J. Creswick, *Superconductivity*, Academic Press, San Diego, Calif., 1995, p. 392.

superconducting condensation energy. The depairing current density corresponds to the excitation of charge carriers across the superconducting energy gap due to their increased kinetic energy associated with the flow of transport current. Measured values of J_c often fall well below this prediction, due to the vortex motion, which is not accounted for in the G-L theory.

A vortex that is pinned and therefore unable to move also hinders the motion of neighboring vortices. Thus vortex motion and pinning are collective processes, especially for fields near H_{c2}. When the pinning forces are not strong enough to prevent vortex motion, the superconductor is termed "*soft*", while the reverse is true in "*hard*" superconductors. Hard superconductors exhibit magnetization curves which show strong hysteresis effects due to the trapping of flux caused by vortex pinning. Examples of hysteretic magnetization curves for the type II high-T_c superconductor $YBa_2Cu_3O_7$ are shown in Fig. W16.9. As the superconductor is cycled around the magnetization loop the energy dissipated in the material per unit volume is proportional to the area inside the hysteresis loop [see Eq. (17.10)]. The remanent magnetization M_r and the coercive field H_c are defined as shown. The magnetization M_r remaining

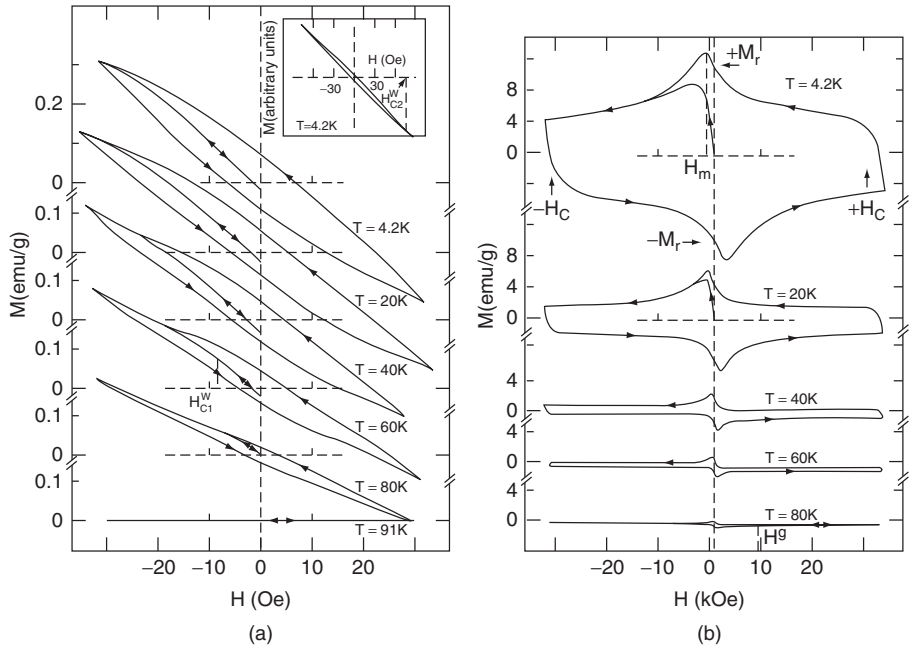

Figure W16.9. Magnetization curves for the high-T_c superconductor $YBa_2Cu_3O_7$: (*a*) low-field loops; (*b*) high-field loops. The observed hysteresis is due to the trapping of flux caused by the pinning of vortices. The remanent magnetization M_r and the coercive field H_c are defined as shown. The quantities H_m and H^g are the magnetic fields at which M reaches a maximum and above which M is reversible, respectively. (From S. Senoussi et al., *J. Appl. Phys.*, **63**, 4176 (1988). Copyright 1988 by the American Institute of Physics.)

at $H = 0$ corresponds to the magnetic moment per unit volume of the shielding supercurrents which flow around regions of *trapped flux*. These regions of trapped flux are either void regions or regions that remain normal even after most of the material has returned to the superconducting state. The fraction of the sample that remains in the normal state at $H = 0$ is proportional to M_r.

The phenomenon of *flux creep* can occur in the presence of a transport current flowing through a superconductor when the pinning forces are strong, while the process of *flux flow* occurs when the pinning forces are weak. In both cases, dissipation is present. The results of measurements of the critical currents in two $Nb_{0.5}Ta_{0.5}$ alloys with different defect concentrations are shown in Fig. W16.10. The voltage–current curves shown have intercepts on the current axis equal to i_c, the critical current at which a voltage first appears in the superconductor. The slopes dV/di for $i > i_c$ yield the *flux-flow resistance* R_{ff}, which corresponds to a resistivity $\rho_{\text{ff}} \approx \rho_n(B/B_{c2})$, where ρ_n is the normal-state resistivity and B is the average flux density in the mixed state. Note that i_c is higher for the alloy with the higher defect or pinning center concentration, while the flux-flow resistances are independent of the defect level. The resistance R_{ff} increases with increasing magnetic field, as the vortices move faster through the material, and approaches the normal-state resistance as $H \to H_{c2}$.

The collective motion of vortices can be understood in terms of the flow of a two-dimensional viscous fluid. When the vortices are strongly pinned, the vortex fluid

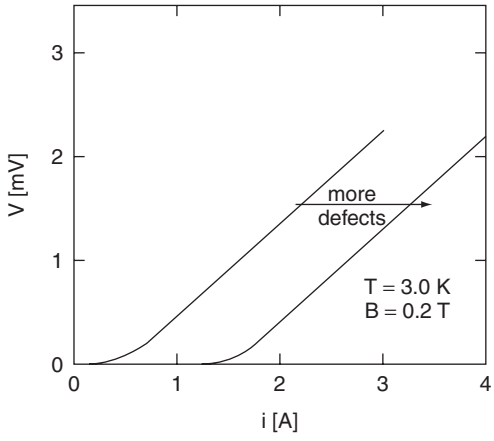

Figure W16.10. Results of measurements of the critical currents in two $Nb_{0.5}Ta_{0.5}$ alloys with different defect concentrations. [From A. R. Strnad, C. F. Hempstead, and Y. B. Kim, *Phys. Rev. Lett.*, **13**, 794 (1964). Copyright 1964 by the American Physical Society.]

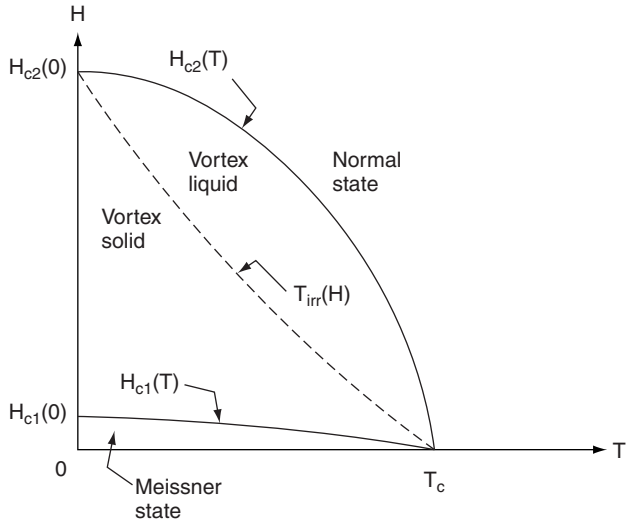

Figure W16.11. Magnetic phase diagram for a type II high-T_c superconductor. The vortex solid (or glass) and vortex liquid phases in the mixed state between H_{c1} and H_{c2} are shown.

instead forms a solid phase. When long-range order is present in the solid phase, a *vortex lattice* is formed (see Fig. 16.11). The vortex solid is termed a *vortex glass* if only short-range order is present, due to the spatial randomness of the pinning centers. A schematic magnetic phase diagram for a type II high-T_c superconductor showing the vortex solid and liquid phases in the mixed state between H_{c1} and H_{c2} is presented in Fig. W16.11 for H perpendicular to the *ab* planes. In practice, H_{c1} can be orders of magnitude less than H_{c2}. This phase diagram is considerably more complicated than the simpler version given in the textbook in Fig. 16.7*c* for low-T_c conventional type II superconductors. The fact that dissipation-free transport of current

can occur only in the vortex solid phase where the vortices are strongly pinned has complicated the development of the high-T_c superconductors for high-field current-carrying applications. Recent progress that has been made in this area is discussed later when large-scale applications of superconductivity are described.

Note that the vortex solid "melts" as either higher temperatures (thermal activation) or higher magnetic fields are applied to the superconductor. Under these conditions the vortices become depinned from defects and decoupled from each other. This transition occurs at the *irreversibility temperature* T_{irr} shown in Fig. W16.11, which defines the melting line separating the vortex solid and liquid phases. This boundary also serves to define the temperature-dependent *irreversibility magnetic field* H_{irr}. Magnetic flux-dependent reversibility is observed in the vortex liquid phase, while magnetic irreversibility is found in the vortex solid phase. Flux trapping therefore occurs much more readily in the vortex solid phase. Even before the flux lattice melts, flux creep can still occur for $T < T_{\text{irr}}$ due to thermal activation of the vortices out of their pinning potential wells. The velocity of the resulting flux motion is given by

$$v = v_{\text{o}} \exp\left(-\frac{U}{k_B T}\right), \tag{W16.7}$$

where the activation energy U is a complicated function of current density J, magnetic field H, and temperature T. Note that $U \to 0$ as $J \to J_c$. The energy U can have values ranging from tenths of an electron volt up to several electron volts. The vortex liquid phase is more evident and occupies a greater portion of the phase diagram for high-T_c superconductors than for conventional superconductors, due to the higher T_c values of the former, which enhance the effects of thermal depinning. The boundary between the vortex solid and liquid phases can be shifted to higher magnetic fields and temperatures by introducing additional pinning centers into the superconductor which help to stabilize the vortex solid phase.

Although defects are useful for the pinning of vortices, if too much of the superconductor is defective (e.g., nonsuperconducting), the necessary superconducting current paths will not be present.

W16.9 Further Discussion of Large-Scale Applications

Since Nb_3Sn is inherently brittle and cannot be drawn down by itself into wires, the wire used for superconducting applications is typically formed by inserting Nb rods into Sn tubes which are then drawn down repeatedly to a certain size. The thin rod thus formed is then inserted into a Cu tube and drawn down repeatedly again. Heat treatment is then used to form the Nb_3Sn superconducting compound at the Nb/Sn interfaces. The resulting wire can carry high currents in a lossless manner and is also relatively flexible and mechanically stable due to the copper sheathing. Nb–Ti alloys do not require such complex processing since they have the advantage of being inherently ductile.

The *pinning centers* in Nb–Ti alloys can be created by annealing processes that cause the precipitation of clusters of metallic α-Ti with $T_c \approx 0.4$ K. After drawing the wire down, the Ti pins typically are $\approx$ 1 to 2 nm in size and spaced $\approx$ 3 to 6 nm apart. Pinning centers can also be introduced into the Nb–Ti alloy in an artificial manner by placing a macroscopic pin material such as a low-field superconductor (Nb

or Ti), a normal metal (Cu), or even a ferromagnetic metal (Ni or Fe) into the alloy before drawing it down. The ferromagnetic pins are especially effective because of the destructive effect that magnetic moments have on superconductivity.

The high-T_c cuprate superconductors are ceramics and hence are inherently brittle. This property presents a serious challenge for the fabrication of long wires of these materials. The current-carrying capacity of polycrystalline high-T_c samples can be improved by techniques which enhance intergrain contact so that superconducting currents can easily flow from one grain to another, preferably parallel to the *ab* planes, which have higher critical currents. High-angle grain boundaries in high-T_c materials which form weak links between adjacent superconducting crystalline grains will limit the lossless flow of supercurrents through the materials.

High-T_c superconductors tend to have weaker pinning forces than elemental or intermetallic compound superconductors, due in part to the fact that they have "pancake" vortices (i.e., the supercurrents surrounding each vortex exist only within the CuO_2 layers). Therefore, the vortices in adjacent CuO_2 layers are not as strongly coupled to each other as in superconductors whose structures are three-dimensional. Intrinsic pinning in high-T_c materials refers to the difficulty that vortices have in moving perpendicular to the copper–oxygen layers through the isolation barriers composed of layers of atoms which are essentially normal material. The pancake vortices can move within the *ab* planes, and defects confined to a given layer will affect only the motions of vortices in that layer. Flux creep occurs much more rapidly when vortices move parallel to the copper–oxygen layers than when the vortex motion is perpendicular to the layers.

The vortex solid is much more stable in $YBa_2Cu_3O_7$ than in other high-T_c superconductors, such as the BSCCO family. This is likely the result of pinning centers with deeper potential wells in $YBa_2Cu_3O_7$. Also, because the spacing between groups of superconducting CuO_2 layers is smaller in $YBa_2Cu_3O_7$ than in the BSCCO family, the pancake vortices are more strongly coupled along the c axis in $YBa_2Cu_3O_7$. Nevertheless, $YBa_2Cu_3O_7$ tends to have lower critical currents due to weak links between adjacent superconducting grains and is more difficult to prepare in wire form.

A method similar to that used for Nb_3Sn is employed for some high-T_c materials where a silver tube is filled with powder of, for example, Pb-stabilized $Bi_{2-x}Pb_xSr_2Ca_2Cu_3O_{10}$. The filled tube is then drawn, rolled, and sintered, resulting in a material that is fairly well aligned with the superconducting CuO_2 layers of the crystallites lying roughly parallel to each other. This desirable platelike microstructure of the BSCCO superconductors results from the ease of cleavage of the two adjacent BiO layers perpendicular to the c axis (see Fig. 16.17). The success of this processing method is due to the chemical stability of the high-T_c materials in the presence of Ag and also to the ease of diffusion of oxygen through the Ag sheath, that allows the proper stoichiometry to be achieved following sintering or annealing in O_2. Heavy-ion irradiation of $Bi_2Sr_2Ca_2Cu_3O_{10+x}$/Ag tapes introduces columnar defects in the form of amorphous regions ≈ 7.4 nm in diameter surrounded by an associated strain field. These columnar defects are currently the most efficient pinning centers known for flux lines in layered superconductors, such as the high-T_c cuprates.

Although some important fabrication problems have been solved, the losses in $Bi_2Sr_2Ca_2Cu_3O_{10}$ wires remain too high for their application at $T = 77$ K in high magnetic fields. When used in applications such as superconducting magnets or electrical machinery where high magnetic fields are present, this material must be kept below $T = 25$ to 30 K in order to operate in the vortex solid region of the magnetic

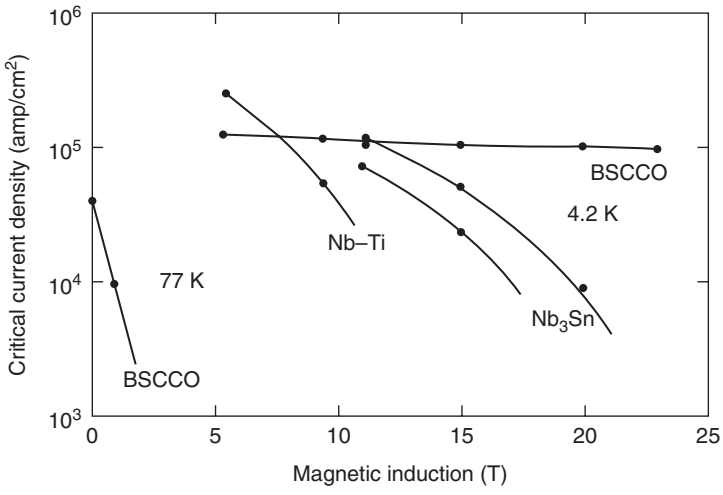

Figure W16.12. Magnetic field dependence of the critical current density in BSCCO tapes sheathed in Ag compared with J_c for Nb–Ti and Nb_3Sn. (From D. Larbalestier, *Phys. Today*, **44**, 74 (1991). Copyright 1991 by the American Institute of Physics.)

phase diagram, where resistive losses are low. The magnetic field dependence of the critical current density in BSCCO tapes sheathed in Ag is presented in Fig. W16.12 and compared with J_c for commercial Nb–Ti and Nb_3Sn superconductors. It can be seen that $Ba_2Sr_2Ca_2Cu_3O_{10}$ retains its ability to carry transport currents to much higher fields at $T = 4.2$ K, but not at 77 K, than the Nb-based superconductors.

The growth of $YBa_2Cu_3O_7$ on flexible Ni alloy tapes with matching thermal expansion coefficients and the use of an intermediate buffer layer of yttria-stabilized zirconia to prevent chemical interactions has proven to be a useful method of synthesizing superconducting wire which can operate at $T = 77$ K with $J_c \approx 1$ MA/cm^2 in zero magnetic field (see Table W16.2). When operated at $T \approx 64$ K, short lengths of these $YBa_2Cu_3O_7$ conductors have critical current densities in fields up to 8 T, which are equal to those of the currently used Nb–Ti and Nb_3Sn materials at $T = 4.2$ K.

In a high-T_c superconductor such as $YBa_2Cu_3O_7$, where $\xi \approx 1$ to 2 nm, the optimum configuration of pinning defects corresponds to a very high density of small defects. Thus any form of atomic disorder should serve as a pinning center in these high-T_c superconductors. The difficulty is in introducing this atomic-level disorder in a reproducible manner.

W16.10 Josephson Effects

When both sides of a tunnel junction are superconducting (e.g., for an S–I–S junction), an additional contribution to the usual quasiparticle or normal-electron tunneling current can arise from the passage of a supercurrent of Cooper pairs across the junction even when the applied voltage $V = 0$. The resulting *Josephson current* has been observed experimentally, and the related *Josephson effects* serve as the basis for the operation of SQUIDs as the most sensitive existing sensors of magnetic flux. The Josephson relations that are the basis of the Josephson effects are derived next.

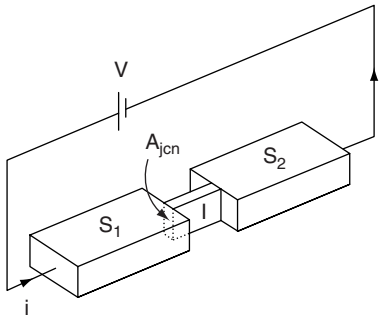

Figure W16.13. Two superconductors, S_1 and S_2, which are part of an S_1–I–S_2 Josephson tunnel junction are weakly coupled to each other through an insulating barrier or weak link I.

Consider two superconductors S_1 and S_2 which are part of an S_1–I–S_2 *tunnel junction* (Fig. W16.13). S_1 and S_2 are weakly coupled to each other through an insulating barrier I, which serves as a weak link. The time-dependent Schrödinger equations for the macroscopic superconducting wavefunctions Ψ_1 and Ψ_2 in the two superconductors are given by

$$\begin{aligned} i\hbar\frac{d\Psi_1}{dt} &= eV\Psi_1 + K\Psi_2, \\ i\hbar\frac{d\Psi_2}{dt} &= eV\Psi_2 + K\Psi_1. \end{aligned} \tag{W16.8}$$

Here the strength of the coupling through the barrier is represented by the parameter K. The physical significance of these equations is that the wavefunctions and the corresponding Cooper pairs of the two superconductors can overlap each other within the junction region. When the overlap is sufficiently strong, the phases of the two wavefunctions will be coupled to each other and Cooper pairs will be able to tunnel across the junction even for $V = 0$. Note that these equations are also appropriate for the case when a voltage is applied across the junction.

The wavefunctions Ψ_1 and Ψ_2 can be written as the products of an amplitude factor expressed in terms of the concentration n_s of superconducting electrons and a phase factor as follows:

$$\begin{aligned} \Psi_1(t) &= \sqrt{n_{s1}(t)}e^{i\theta_1(t)}, \\ \Psi_2(t) &= \sqrt{n_{s2}(t)}e^{i\theta_2(t)}, \end{aligned} \tag{W16.9}$$

where $\theta(t) = \theta_2(t) - \theta_1(t)$ is the phase difference between the wavefunctions on opposite sides of the junction. Note that $|\Psi_1|^2 = n_{s1}$ and $|\Psi_2|^2 = n_{s2}$. When these expressions for Ψ_1 and Ψ_2 are substituted into Eq. (W16.8), the following results can be derived:

$$\hbar\frac{dn_{s1}}{dt} = 2K\sqrt{n_{s1}n_{s2}}\sin\theta, \tag{W16.10a}$$

$$\hbar\frac{dn_{s2}}{dt} = -2K\sqrt{n_{s1}n_{s2}}\sin\theta, \tag{W16.10b}$$

$$\frac{d\theta}{dt} = \frac{2eV}{\hbar}. \tag{W16.11}$$

The *Josephson current* $i(t)$ that can flow through the junction is given in terms of the rates of change with time of n_{s1} and n_{s2} by

$$i(t) = e\left(V_1 \frac{dn_{s1}}{dt} - V_2 \frac{dn_{s2}}{dt}\right). \tag{W16.12}$$

Here the volumes V_1 and V_2 correspond to the regions in the superconductors in which the changes in n_{s1} and n_{s2} occur, typically within a coherence length ξ of the junction. The substitution of Eqs. (W16.10*a*) and (W16.10*b*) into Eq. (W16.12) results in the following current-phase relationship:

$$J(t) = J_c \sin\theta(t). \tag{W16.13}$$

The Josephson current density is defined as $J = i/A$, where A is the cross-sectional area of the junction. Thus it is evident that an applied current will control the phase difference θ across the junction. The prefactor J_c, the *critical current density*, corresponds to the maximum current that can flow through the junction when $V = 0$. It is given by

$$J_c = \frac{4eK\sqrt{n_{s1}n_{s2}}}{\hbar} \frac{(V_1 + V_2)}{A}. \tag{W16.14}$$

Equations (W16.11) and (W16.13) are known as the *Josephson relations* and are the fundamental expressions describing the tunneling of Cooper pairs.

Four distinct types of phenomena involving the tunneling of Cooper pairs across a *Josephson junction* are discussed next.

DC Josephson Effect. The *dc Josephson effect* corresponds to the spontaneous flow of the direct tunneling current $J = J_c \sin\theta_0$ given in Eq. (W16.13) for $V = 0$. Since in this case $d\theta/dt = 0$ from Eq. (W16.11), the difference in phase θ_0 of the superconducting order parameter across the junction will be constant. Thus a superconducting Josephson junction can act as a direct-current source. It can be seen from Eq. (W16.14) that $J \propto n_s(T)$. It follows, therefore, that $J_c(T)$ will increase from 0 at $T = T_c$ and will reach a finite value at $T = 0$ K, which can be shown to be about 80% of the corresponding normal-metal tunneling conductance. For the current to exceed J_c, a voltage must be present across the junction.

There exist junctions or weak links between pairs of superconductors in which the current does not exhibit the sinusoidal dependence on the phase difference θ expressed in Eq. (W16.13). Although these are not Josephson junctions, they are nevertheless sensitive to θ and to changes in the magnetic flux Φ through the junction. True Josephson tunneling can be observed only for the case of very thin barriers, ≈ 1 nm thick.

AC Josephson Effect. When a constant voltage is applied across the Josephson junction, it follows from Eq. (W16.11) that the phase difference θ will change linearly with time according to

$$\theta(t) = \frac{2eVt}{\hbar} + \theta_0. \tag{W16.15}$$

In additional to the usual tunneling of normal electrons or quasiparticles, there will also be a sinusoidal or alternating tunneling current of Cooper pairs in this case given by

$$J(V,t) = J_c \sin\left(\frac{2eVt}{\hbar} + \theta_0\right). \tag{W16.16}$$

This alternating current flows through the junction at the Josephson angular frequency $\omega_J = 2eV/\hbar = 2\pi V/\Phi_0$, where Φ_0 is the flux quantum. This current corresponds to the *ac Josephson effect*. For an applied voltage $V = 1$ mV, the corresponding *Josephson frequency* $f_J = \omega_J/2\pi = 4.84 \times 10^{11}$ Hz is in the RF region. The junction can therefore act as a source of RF radiation whose frequency, 4.84×10^{11} Hz/mV, can be controlled precisely through the applied voltage. An interesting application of the ac Josephson effect is in an extremely precise determination of the ratio e/h, which is used in establishing a self-consistent set of recommended values of the fundamental physical constants. The amplitude J_c is also a function of the applied voltage and reaches a maximum at $eV = 2\varepsilon$, the superconducting energy gap. Note that in this case a photon is involved in the Cooper pair tunneling for conservation of energy because, with $|V| > 0$, the condensed states are no longer aligned across the junction.

A detailed analysis of the response of a Josephson junction when "driven" by a constant voltage must also take into account the capacitance of the junction and also any nonzero normal conductance that the barrier may have if it is not a perfect insulator. While the response of the junction approaches normal-metal tunneling for $eV > 2\varepsilon$, the i–V characteristics for $eV < 2\varepsilon$ can be complicated and can exhibit hysteresis.

Inverse AC Josephson Effect. The *inverse* ac Josephson effect is observed when either incident RF radiation or an applied RF current of frequency f causes a dc voltage $V = hf/2e$ to appear across an unbiased junction. The junction can thus serve as a very sensitive detector of radiation. The i–V characteristic in this case exhibits current steps or spikes as a function of the voltage, with the voltage separation between steps given by $\Delta V = hf/2e$. For this application the use of a weak link in the form of a constriction or point contact is preferred due to the ease of coupling the radiation into or out of the junction.

Macroscopic Quantum Effects. The application of a transverse magnetic field H to a "short" S_1–I–S_2 Josephson junction can result in the flow of a tunneling current given by

$$J(\Phi) = J_c \sin\theta_0 \frac{\sin(\pi\Phi/\Phi_0)}{\pi\Phi/\Phi_0}. \tag{W16.17}$$

Here Φ is the total magnetic flux passing through the junction and given by $\Phi = BA_{\text{eff}} = \mu_0 H d_{\text{eff}} w$, Φ_0 is the quantum of flux, and θ_0 is the phase difference at a certain point in the junction. A "short" junction is defined as one for which the magnetic field of the junction current J is much less than the applied magnetic field H. Note that the effective junction width $d_{\text{eff}} = (d + \lambda_1 + \lambda_2)$ accounts for the penetration of magnetic flux into the two superconductors adjacent to the junction (see Fig. W16.14). This current represents a *macroscopic quantum interference effect* in which $J(\Phi)$ oscillates as a function of the magnetic flux Φ passing through the effective area A_{eff} of the junction. Note that $J = 0$ when $\Phi = n\Phi_0$ (i.e., whenever an integral number of flux

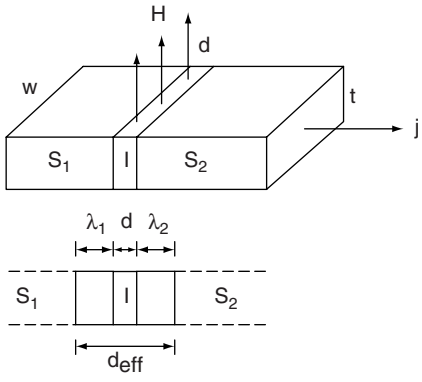

Figure W16.14. Application of a magnetic field H to an S_1–I–S_2 tunnel junction results in magnetic flux $\Phi = BA_{\text{eff}}$ passing through the junction.

quanta pass through A_{eff}). The actual current flow changes directions over the cross section of the junction perpendicular to the direction of the current flow.

W16.11 SQUIDS and Other Small-Scale Applications

The sensitivity of the two-junction loop (see Fig. 16.23*a*) to changes in magnetic flux can be illustrated by first noting that the total change in phase $\Delta\theta$ of the superconducting order parameter around the loop is proportional to the total magnetic flux Φ passing through the loop. This follows from the expression

$$\oint \nabla\theta \cdot d\mathbf{l} = \frac{2\pi}{\Phi_0} \oint \mathbf{A} \cdot d\mathbf{l}, \tag{W16.18}$$

where $\mathbf{A}$ is the vector potential and the integrals are taken around the loop along a path on which the current density $J = 0$. The integral on the left is equal to $\Delta\theta$ while the integral on the right is just the total flux Φ. Evaluation of the two integrals therefore yields

$$\Delta\theta = \theta_a - \theta_b = \frac{2\pi\Phi}{\Phi_0}, \tag{W16.19}$$

assuming that the loop currents do not contribute to the flux Φ. Since the phase is constant within each superconductor, the changes in phase θ_a and θ_b occur across the respective junctions.

The total current i passing through the two-junction loop from an external source is given by the sum of the individual currents passing through each junction, which can be written using Eqs. (W16.13) and (W16.19) as

$$\begin{aligned} i &= i_a(\theta_a) + i_b(\theta_b) = i_{ca}\sin\theta_a + i_{cb}\sin\theta_b \\ &= i_{ca}\sin\theta_a + i_{cb}\sin\left(\theta_a - \frac{2\pi\Phi}{\Phi_0}\right) = i(\Phi). \end{aligned} \tag{W16.20}$$

For the idealized case where the two junctions carry equal currents $i_{ca} = i_{cb} = i_c$, it can be shown that the maximum current that can flow depends on the flux Φ through

the loop and is given by

$$i_{\max}(\Phi) = 2i_c \left| \cos \frac{\pi \Phi}{\Phi_0} \right| . \tag{W16.21}$$

This is known as the *Josephson loop interference equation* since, in the absence of an applied voltage, no net current i can flow through the loop when the total flux through the loop $\Phi = (n + \frac{1}{2})\Phi_0$ due to destructive interference between the two Josephson currents i_a and i_b. The existence of these interference effects justifies calling the loop containing two Josephson junctions a *superconducting quantum interference device* (i.e., a SQUID). In practice the two junctions in the loop will not be identical, so the resulting, more complicated expression for $i(\Phi)$ will depend on both i_{ca} and i_{cb}. Also, when the magnetic flux passing through the junctions cannot be neglected, the current i given in Eq. (W16.20) will be modulated due to the quantization of flux within the junctions themselves.

From a practical point of view, the fabrication of SQUIDs from high-T_c superconductors that can operate at $T = 77$ K is a significant challenge, due to the necessity of maintaining bulk superconducting properties up to within a coherence length ξ of the junction interface. This will be difficult even in the *ab* plane, where $\xi_{ab} \approx 1.5{-}2$ nm. Fortunately, grain boundaries making high angles with respect to the CuO_2 layers that occur naturally in $YBa_2Cu_3O_7$ or which can be introduced during growth can act as Josephson junctions. A significant disadvantage of operating a SQUID at $T = 77$ K is the higher thermal noise that results in loss of resolution when compared to operation at $T = 4.2$ K.

SQUIDs have been used for sensitive electrical and magnetic measurements in the following configurations, shown in Fig. 16.23:

1. In the SQUID-based picovoltmeter the voltage is converted into a change of magnetic flux to which the SQUID can respond.
2. The SQUID magnetometer consists of a dc SQUID (i.e., a pair of Josephson junctions) coupled magnetically to a larger pickup loop. A resolution in magnetic flux density B of 10^{-15} T can be achieved. This corresponds to approximately $10^{-4}\Phi_0$ over an area of 10^{-4} m^2.

Some additional small-scale applications of superconductors are outlined briefly next.

Superconducting Computer Devices. The ability of Josephson junctions to switch from the superconducting to the normal state and back within a few picoseconds (i.e., at frequencies ≈ 100 GHz) with very low power dissipation makes possible their use in ultrafast superconducting digital devices, including logic circuits, shift registers, and A/D converters. These devices will probably make use of either single flux-quantum (SFQ) logic or single-electron logic (SEL). The demonstrated compatibility of junction fabrication with Si-based processing technology will be important for this application. An important advantage of low-temperature operation, at either $T = 4.2$ or 77 K, will be the stability of the devices with respect to the phenomenon of electromigration, which is a serious problem for semiconductor devices operated at room temperature and above.

Optical Detectors. The rapid change in resistivity observed near T_c means that the resistance of a superconductor which also has a low heat capacity can be very sensitive to outside sources of energy. Thin-film superconducting devices based on this effect,

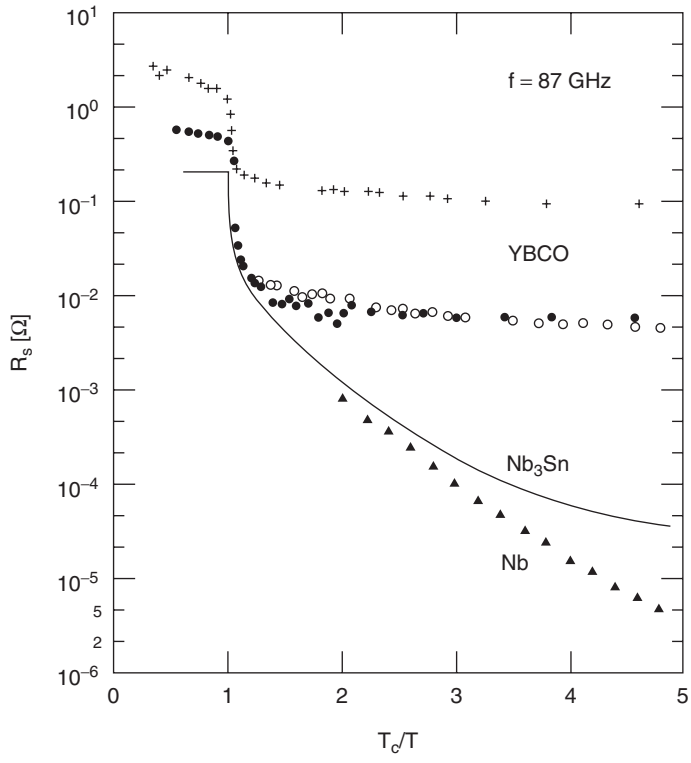

Figure W16.15. Temperature dependence of the measured microwave surface resistance R_s for the high-T_c superconductor $YBa_2Cu_3O_7$ is compared with other superconductors. [From H. Piel and G. Mueller, *IEEE Trans. Magn.*, **27**, 854 (1991). Copyright 1991 IEEE.]

known as *transition-edge bolometers*, have been employed as sensitive detectors of far-infrared radiation. SIS tunnel junctions can also function as sensitive detectors of single photons at infrared frequencies. A photon absorbed in the superconducting thin film breaks superconducting Cooper pairs, thereby generating a cascade of electrons that tunnel through the junction. The total charge collected is proportional to the energy of the incident photon.

Thermal Switches. Superconducting wires with very low κ_s/κ_n ratios of thermal conductivities in the superconducting and normal states are often used as thermal switches. For example, a Pb wire at $T = 4.2$ K has $\kappa_s/\kappa_n \approx 1/100$ and a critical field $H_C \approx 6.4 \times 10^4$ A/m (≈ 800 G). Thus for $H < H_C$ a thin Pb wire in the superconducting state will serve as a thermal insulator. When a field $H > H_c$ is applied, the Pb wire will serve as a good conductor of heat. This capability has been used in cryogenic heat capacity measurements where the sample being studied can be placed in good contact with a liquid He bath and then thermally isolated simply by switching the magnetic field applied to the Pb wire from $H > H_c$ to $H < H_c$.

Microwave Components and Devices. The uses of thin films of the high-T_c superconductor $YBa_2Cu_3O_7$ or the conventional superconductor Nb as delay lines, resonators, and filters in passive microwave devices are being developed due to the

accompanying reduction of losses resulting from the low microwave surface resistances R_s of these materials. For example, epitaxial thin films of $YBa_2Cu_3O_7$ have much lower values of R_s at $T = 77$ K for frequencies up to 100 GHz than are found in normal metals such as Cu and Au. Measured values of R_s for $YBa_2Cu_3O_7$ as a function of temperature are compared with other superconductors in Fig. W16.15. For successful operation, the properties of the superconducting film must be uniform in the surface region corresponding to the penetration depth λ.

One important goal is the achievement of more communication channels in the microwave region of the electromagnetic spectrum for cellular and "personal communication" applications through the use of filters based on high-T_c thin films, which have sharper frequency cutoffs than Cu filters. These microwave devices are likely to be the first successful applications of the high-T_c superconductors.

REFERENCE

Hebard, A. F., Superconductivity in doped fullerenes, Phys. Today, Nov. 1992, p. 26.

PROBLEMS

W16.1 Using the Gibbs free energy per unit volume for the superconducting state as given by the two-fluid model in Eq. (W16.1), calculate (**a**) $C_s(T)$ as $T \to 0$, and (**b**) $\Delta C(T_c) = C_n(T_c) - C_s(T_c)$.

W16.2 A magnetic field H is applied parallel to the surface of a long superconducting cylinder. (*Note*: See Fig. 16.10.)

- **(a)** Show that the variation of the effective magnetization M_y [$= (B_y/\mu_0) - H_y$] resulting from the supercurrents near the surface of the superconductor is given by $M_y(x) = -H_y(x = 0)(1 - e^{-x/\lambda_L})$.
- **(b)** What is the resulting value of M_y inside the superconductor (i.e., for $x \gg \lambda_L$)?

W16.3 A superconducting wire of radius $a = 1$ mm is formed into a single-turn circular loop of radius $r = 10$ cm. A current i is observed to flow around this isolated loop for five years without any measurable decay. Estimate a lower limit for the electrical conductivity σ (or an upper limit for the resistivity ρ) of this wire in the superconducting state. (*Hint*: The inductance of a single-turn circular loop of wire is $L \approx \mu_0 r[\ln(8r/a) - 2]$.)

W16.4 A type I superconductor has a critical magnetic field slope at $T_c = 3$ K given by $d(\mu_0 H_c)/dT = -15$ mT/K.

- **(a)** Estimate its critical field H_{c0} at $T = 0$ K. [*Hint*: Make use of the parabolic expression for $H_c(T)$ given in Eq. (16.6).]
- **(b)** Estimate the superconducting condensation energy per unit volume $G_n - G_s$ at $T = 0$ K for this superconductor.

W16.5 Show that the parabolic dependence of $H_c(T)$ given in Eq. (16.6) follows from the two-fluid expression for $G_s(T)$ of Eq. (W16.1) when the temperature dependence of the fraction of superconducting electrons is given by $f_s(T) = 1 - (T/T_c)^4$.

W16.6 For the A15 structure shown in Fig. W16.2 with the chemical formula Nb_3Ge and cubic lattice constant $a = 0.515$ nm, write down the NN and second-NN configurations and distances for both the Nb and Ge atoms.

W16.7 In the superconducting oxide $Ba_{1-x}K_xBiO_{3-y}$ with the cubic perovskite crystal structure, oxygen vacancies can be present to provide ionic charge compensation for the replacement of Ba^{2+} ions by K^+ ions. What value of y would be needed for complete ionic charge compensation of this material when $x = 0.4$?

W16.8 Show that the $n = 0$, 1, and 2 versions of the $HgBa_2Ca_nCu_{n+1}O_{(2n+4)+x}$ compound with $x = 0.06$, 0.22, and 0.40 have 0.12, 0.22, and 0.27 holes per Cu atom, respectively. The additional oxygen atoms can be assumed to have entered the Hg^{2+} layers.

W16.9 **(a)** Using the results that the penetration depth $\lambda \propto (m^*)^{1/2}$ and the coherence length $\xi \propto (m^*)^{-1/2}$, show that the inequalities $\xi_{ab} > \xi_c$ and $\lambda_c > \lambda_{ab}$ apply to anisotropic superconductors in which $m_c^* \gg m_a^* = m_b^*$.

(b) Using $H_{c2}(i) = \Phi_0/2\sqrt{2}\mu_0\xi_j\xi_k$, show that $H_{c2}(ab)/H_{c2}(c) = \sqrt{m_c^*/m_{ab}^*}$.

W16.10 Show that the expression $J_c(T) = H_c(T)/\lambda(T)$ for the critical transport current density can be derived by setting the kinetic energy density KE/V of the supercurrents equal to the superconducting condensation energy per unit volume $\mu_0 H_c(T)^2/2$. [*Hint*: Use $\text{KE}/V = (n_s/2)(2m)\langle v\rangle^2/2$, where $\langle v\rangle$ is defined by $J_c = (n_s/2)(2e)\langle v\rangle$ for the Cooper pair current.]

W16.11 Starting from Eqs. (W16.8) and (W16.9), derive the Josephson relations given in Eqs. (W16.11) and (W16.13).

W16.12 Sketch the tunneling current

$$J(\Phi) = J_c \sin\theta_0 \frac{\sin(\pi\Phi/\Phi_0)}{\pi\Phi/\Phi_0}$$

passing through the tunnel junction shown in Fig. W16.14 as a function of Φ/Φ_0. Note that $J = 0$ when $\Phi = n\Phi_0$ (i.e., whenever an integral number of flux quanta pass through the junction area A). Show that $J(\Phi \to 0)$ approaches the finite limit $J_c \sin\theta_0$.

W16.13 Consider a Nb–I–Pb junction which is $d = 50$ nm thick and 20 μm wide. For what value of magnetic field H applied perpendicular to the junction will exactly one quantum of flux Φ_0 be present within the effective area A_{eff} of the junction? Be sure to use the effective width of the junction $d_{\text{eff}} = d + \lambda_{Nb} + \lambda_{Pb}$ (see Fig. W16.14).

CHAPTER W17

Magnetic Materials

W17.1 Details on Domain Structures

If N_d is the number of domains in the array shown in Fig. 17.2*b* in the textbook,[†] there will be $(N_d - 1)$ domain walls, each of area lt, in the ferromagnetic film. When $N_d \gg 1$, the total energy associated with the domain walls will be

$$U_w = N_d \sigma_w lt = \frac{\sigma_w V}{d}, \tag{W17.1}$$

where d is the width of each domain, V is the total volume, and $N_d = w/d$. The total magnetic energy of the ferromagnetic film will then be

$$U = U_m + U_w = \frac{0.136 \mu_0 M_s^2 V d}{t} + \frac{\sigma_w V}{d}. \tag{W17.2}$$

When the energy U is minimized with respect to d, the following results are obtained:

$$d = \frac{2.71}{M_s} \sqrt{\frac{\sigma_w t}{\mu_0}}, \tag{W17.3}$$

$$U = 0.738 V M_s \sqrt{\frac{\mu_0 \sigma_w}{t}}. \tag{W17.4}$$

If the energy U is less than the energy U_m for the single domain given in Eq. (17.4), the domain structure shown in Fig. 17.2*b* will be favored over the single domain shown in Fig. 17.2*a*. This will be true and expressions (W17.3) and (W17.4) will be valid as long as the domain wall surface energy σ_w is not too large, that is, as long as

$$\sigma_w < 0.46 \mu_0 M_s^2 t. \tag{W17.5}$$

The actual domain structure found in a ferromagnetic solid can be very complicated and cannot in general be predicted beforehand except in very simple cases.

[†] The material on this home page is supplemental to *The Physics and Chemistry of Materials* by Joel I. Gersten and Frederick W. Smith. Cross-references to material herein are prefixed by a "W"; cross-references to material in the textbook appear without the "W."

W17.2 Details on Size and Shape Effects

A straightforward estimate for an upper limit to the coercive field H_c for a small magnetic particle can be obtained by noting that the effects of anisotropy can be overcome by a magnetic field **H** applied in the direction opposite to the direction of **M** along an easy axis. It has been shown[†] that the magnetic field, which leads to a reversal of the magnetization via the rotation of $\mathbf{M}_s$, is equal to the effective shape anisotropy field H_s when the direction of the applied field **H** is opposite to the direction of $\mathbf{H}_s$ and **M**. Thus H_s can be taken as an upper limit to the coercive field H_c. The corresponding predictions for H_c are summarized in Table W17.1 for the three different types of magnetic anisotropy discussed in Section 17.5. Values of H_c calculated for small Fe particles from these predictions are also included.

It can be seen that the coercive fields due to the anisotropies associated with crystal structure and with applied stress are both inversely proportional to M_s while H_c resulting from particle shape anisotropy is directly proportional to M_s. For the case of a collection of noninteracting randomly oriented particles, H_c is reduced below its value for a single particle. Coercive fields can also be reduced by the magnetic interactions between individual particles in a powder, the effect being greater the denser the packing. Note that for the case of particle-shape anisotropy, the coercive field is a maximum for a long circular cylinder ($N_\perp = \frac{1}{2}$, $N_\parallel = 0$) magnetized along its length. In this case, $H_c = M_s/2$.

The contributions of surfaces and interfaces to the magnetocrystalline and magnetoelastic anisotropies can be important in magnetic thin films and multilayers. For example, in Au/Co/Au sandwiches the easy axis in the Co film is out of the plane for Co thicknesses of about six atomic layers and less. This has been attributed to magnetocrystalline

TABLE W17.1 Estimates Predicted for the Upper Limit of the Coercive Fields H_c of Small Magnetic Particles

Type of Anisotropy	H_c[a]	Typical Value[b] (kA/m)
Magnetocrystalline		
Single particle	$\dfrac{2K_1(\text{or } K_u)}{\mu_0 M_s}$	39
Randomly oriented particles ($K_1 > 0$)	$\dfrac{0.64K_1(\text{or } K_u)}{\mu_0 M_s}$	25
Particle shape		
Single particle	$(N_\perp - N_\parallel)M_s$	855
Randomly oriented particles	$0.48(N_\perp - N_\parallel)M_s$	410
Applied stress	$\dfrac{3\lambda\sigma}{\mu_0 M_s}$	3.6

[a] K_1 and K_u are the magnetocrystalline anisotropy coefficients for cubic and uniaxial ferromagnets, respectively.

[b] The parameters used are those appropriate for Fe at $T = 300$ K: $K_1 = 4.2 \times 10^4$ J/m^3, $M_s = 1710$ kA/m, magnetostriction $\lambda \approx 2 \times 10^{-5}$, yield strength $\sigma_y = 1.3 \times 10^8$ N/m^2. For the case of shape anisotropy, the particle shape corresponds to a long needle with $N_\perp = \frac{1}{2}$ and $N_\parallel = 0$.

[†] C. Kittel, *Rev. Mod. Phys.*, **21**, 541 (1949).

anisotropy related to the orbital component of the magnetic moment. This type of magnetocrystalline anisotropy results from the anisotropic bonding in multilayers such as Au/Co/Au and the spin–orbit interaction. In thicker Co films the shape-induced in-plane anisotropy dominates the orbital anisotropy and the easy axis is in-plane.

When the easy axes are the same for the magnetocrystalline and shape anisotropy effects, as might be the case in a long, needle-shaped particle, the coercive field is predicted to be enhanced since these anisotropy effects are then additive. In this case, H_c would be given by

$$H_c = \frac{2K_1(\text{or } K_u)}{\mu_0 M_s} + (N_\perp - N_\parallel)M_s. \tag{W17.6}$$

Measured values of H_c are often found to fall well below those predicted in Table W17.1, which correspond to the coherent rotation of **M**. These lower values of H_c are usually due to domain nucleation associated with defects. In other mechanisms for the reversal of the magnetization that can occur at lower fields, the rotation of **M** is noncoherent (i.e., it occurs in a spatially nonuniform manner within the material).[†]

W17.3 Details on Magnetostriction

The magnetostriction of single-crystal $Fe_{1-x}Ni_x$ alloys with $x = 0.6$ and 0.85 is, in fact, observed to be isotropic. For the $Fe_{0.4}Ni_{0.6}$ alloy λ is large and positive, while for the $Fe_{0.15}Ni_{0.85}$ alloy magnetostriction is essentially absent (i.e., $\lambda \approx 0$). For completely random polycrystalline materials which can be expected to be both elastically and magnetically isotropic, the *isotropic magnetostriction* is given by

$$\lambda = \frac{2\lambda_{100}}{5} + \frac{3\lambda_{111}}{5}, \tag{W17.7}$$

where λ_{100} and λ_{111} correspond to single crystals of the same material.

While an applied stress can affect the state of magnetization in a magnetic material, it does not affect the value of the spontaneous magnetization M_s in the elastic limit. Changes in M_s can occur in the inelastic regime, however, but only when the applied stress is large enough to cause a structural phase transition. When $K_\sigma > K_1$ or K_{u1} for the magnetocrystalline anisotropy, the effect of the applied stress can be large enough to change the direction of the easy axis away from that corresponding to the magnetocrystalline anisotropy.

The dependence of the linear magnetostriction $\delta l/l$ on applied magnetic field for the rare earth ferromagnet $Tb_{0.6}Dy_{0.4}$ is shown at $T = 77$ K in Fig. W17.1 for two different stresses applied to an *a*-axis rod. The magnetization and magnetostriction both reach saturation at essentially the same magnetic field. The observed changes in $\delta l/l$ result from the changing state of the magnetization in the material as the applied field is increased and the magnetic domains are aligned in the direction of **H**. When the magnetization is saturated, the observed magnetostriction also reaches its saturation value λ, as shown.

When a magnetic field **H** is applied perpendicular to the easy *c* axis of a crystalline uniaxial ferromagnet such as Co, the development of the macroscopic magnetization

[†] I. S. Jacobs and C. P. Bean, *Phys. Rev.*, **100**, 1060 (1955).

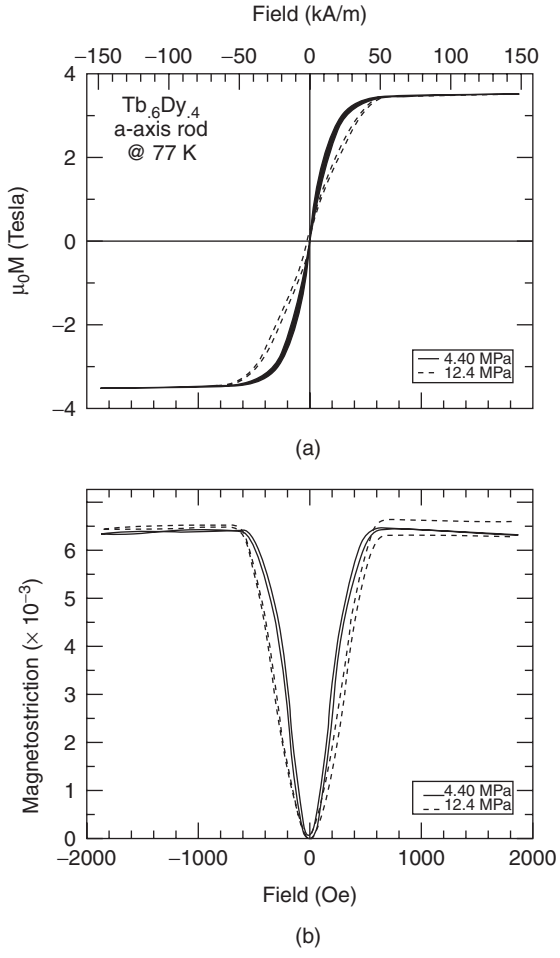

Figure W17.1. Dependencies of the magnetization M, (*a*), and magnetostrictive strain $\delta l/l$, (*b*), on applied magnetic field at $T = 77$ K for the rare earth ferromagnet $Tb_{0.6}Dy_{0.4}$ are presented for two different stresses (MPa = megapascals) applied to an *a*-axis rod. (Note that the magnetization is actually plotted as $\mu_0 M$ and that the field scales are the same in (a) and (b)). [From A. E. Clark et al., *IEEE Trans. Magn.* **MAG-22**, 3156 (1992). Copyright 1992 by IEEE.]

M takes place solely by rotation of the individual domain magnetizations. In this case the dependence of the fractional change in length is given in terms of M by

$$\frac{\delta l}{l} = \frac{3\lambda}{2}\left(\frac{M}{M_s}\right)^2. \tag{W17.8}$$

For cubic ferromagnets with magnetocrystalline anisotropy coefficients $K_1 > 0$, the dependence of $\delta l/l$ on M/M_s is determined by the relative ease with which 90° and 180° domains walls move. A useful discussion of the phenomenology of magnetostriction is given in Chikazumi (1964 Chap. 8). The topic of volume magnetostriction is also covered by Chikazumi.

W17.4 Giant and Colossal Magnetoresistance

So-called *giant negative magnetoresistance* (GMR) effects in magnetically inhomogeneous materials, first observed in metallic Fe/Cr magnetic multilayers, typically correspond to changes in the ratio $[R(0) - R(H)]/R(H)$ by 100 to 1000% in fields of about 1.6×10^3 kA/m. These effects arise from changes in the spin-dependent scattering of the conduction electrons as a result of an applied magnetic field that affects the orientation of the magnetization **M** in the ferromagnetic Fe layers. Experimental results for the GMR effect in three different Fe/Cr multilayers at $T = 4.2$ K are shown in Fig. W17.2. The longitudinal magnetoresistance and the magnetization of these multilayers reach saturation at the same magnetic field H_s. It can be seen that the magnitude of the magnetoresistance changes with the thickness of the nonferromagnetic Cr layer. In fact, the magnitude of the GMR effect oscillates as the thickness of the Cr layer is increased. This is attributed to an interlayer exchange coupling that oscillates between ferromagnetic and antiferromagnetic. Only multilayers for which the interlayer coupling is antiferromagnetic display large GMR effects, apparently due to the fact that only in these systems can the coupling be changed significantly by an applied magnetic field.

The scattering processes that give rise to the GMR effect are believed to take place at the interfaces between the ferromagnetic layers and the adjacent nonferromagnetic or nonmagnetic layers rather than within the ferromagnetic layers themselves. In fact, the magnetoresistance of the Fe/Cr multilayers is much greater than the intrinsic magnetoresistance of the Fe layers themselves. The resistance of the multilayer structure is higher when the magnetizations in the ferromagnetic layers are antiparallel and lowest when they are parallel. A wide variety of transition metal magnetic-multilayer systems have been observed to demonstrate the GMR effect, including Co/Cu, which exhibits very large GMR effects even at room temperature. In fact, Co/Cu multilayers are now used in magnetic read heads for the detection of magnetic bits on hard disks, as described in Sections 17.12 and W17.12.

The phenomenon of *colossal magnetoresistance* (CMR), with observed magnetic field-induced decreases of resistance in the range 10^5 to 10^6%, have been observed

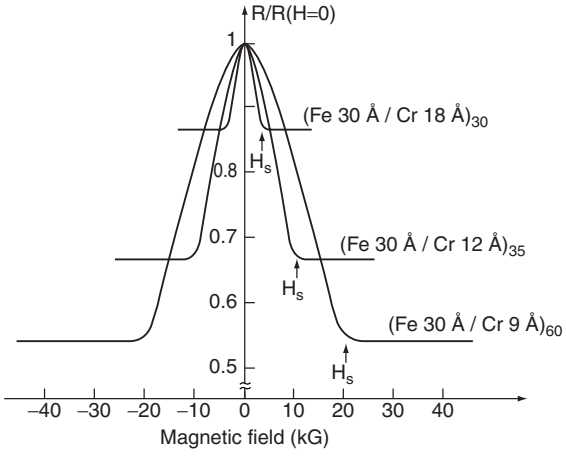

Figure W17.2. Experimental observations of giant longitudinal magnetoresistance $R(H)/R(0)$ in three different (001)Fe/(001)Cr magnetic multilayers at $T = 4.2$ K. [From M. N. Baibich et al., *Phys. Rev. Lett.*, **61**, 2472 (1988). Copyright 1988 by the American Physical Society.]

in ceramic magnetic materials of the form $A_{1-x}B_xMnO_3$ (e.g, $La_{1-x}Ca_xMnO_3$), which have the cubic perovskite crystal structure shown in Fig. 15.6. Here A and B are trivalent rare earth and divalent alkaline earth ions, respectively. In these CMR materials, magnetic ions such as Mn can exist in more than one valence state (e.g., as Mn^{3+} and Mn^{4+} in $La_{1-x}Ca_xMnO_3$). The change in valence from Mn^{3+} to Mn^{4+} occurs as the La^{3+} ions are replaced by Ca^{2+} ions. The effects of an applied field H on the ordering and alignment of the spins of the magnetic ions determine the magnitude of the CMR effect. Conduction in these oxides is proposed to take place by the hopping of d electrons from Mn^{3+} ions to neighboring Mn^{4+} ions via intervening O^{2-} ions. For hopping to occur, the spins of the two Mn ions involved must initially be parallel, thus demonstrating that the resistivity of the material will depend on its magnetic order. This indirect interaction between next-NN Mn^{3+} and Mn^{4+} ions is termed *double exchange* and is essentially a ferromagnetic interaction. The properties of these materials are very sensitive to inhomogeneities related to deviations from oxygen stoichiometry. It should be noted that $LaMnO_3$ itself is an antiferromagnetic insulator, while $La_{1-x}Ca_xMnO_3$ becomes ferromagnetic for $0.3 < x < 0.5$. Note that the superexchange interaction between next-NN Mn^{2+} ions in MnO, described in Section 9.7, via the intervening O^{2-} ions is an antiferromagnetic interaction.

It is possible that this CMR may result from a magnetic field–induced ferromagnetic metal–paramagnetic insulator transition.[†] The CMR effect occurs over a restricted range of temperatures near the transition. Starting from high T, as the temperature is lowered, evidence is found for the formation of small ferromagnetic clusters which are approximately 1.2 nm in diameter in $La_{0.67}Ca_{0.33}MnO_3$. The clusters are conducting but are isolated from each other. As the temperature is lowered still further, the number of these clusters grows until they percolate through the material at the transition temperature and form an infinite cluster. Above T_c the material conducts weakly via carrier hopping from cluster to cluster, while below T_c, electrons are delocalized over the entire percolation cluster and the material conducts as a metal. The magnetic and *metal–insulator* (M–I) transitions do not occur at well-defined temperatures, with the M–I transition occurring at a slightly lower temperature.

The mechanism of the CMR is still an open area of research. In the high-temperature insulating state the spin-up and spin-down states are degenerate and both bands are fully occupied by Mn $3d$ electrons. The Fermi level lies above both bands. In the low-temperature ferromagnetic state, there is a splitting of the spin-up and spin-down bands. Spin-resolved photoemission studies have verified that the Fermi level lies in the interior of the majority-spin band, so that those electrons can conduct, whereas the minority-spin band lies below the Fermi level, and those electrons remain nonconducting. The material is said to be a *half-metal*. The unequal occupancy of the two bands leaves an unbalanced magnetic moment and the material becomes a ferromagnet, as shown in Fig. W17.3.

The magnetic moment of each cluster is randomly oriented in zero field. Hopping of electrons and holes from one cluster to another is inhibited since the spins of the clusters may not be aligned. Carriers from one cluster would have to hop an appreciable distance to find a suitably aligned cluster. The application of an external magnetic field serves to align the magnetic moments of the clusters and hence to reduce the effective hopping distance. This can account for the dramatic sensitivity of the conductivity

[†] For a useful review, see C. N. R. Rao et al., *Chem. Mater.*, **8**, 2421 (1996).

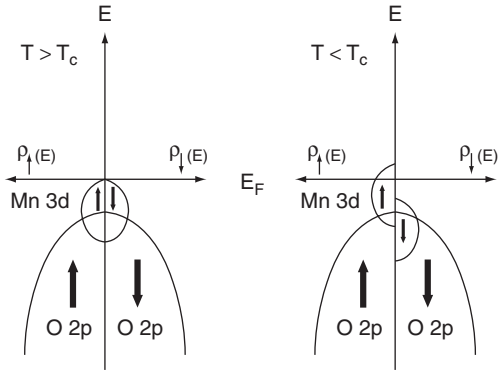

Figure W17.3. Schematic diagram of the Mn $3d$ and O $2p$ spin-up and spin-down energy bands in a $La_{1-x}Ca_xMnO_3$-type perovskite, both above and below the Curie temperature T_C. [Adapted from J. H. Park et al., *Nature*, **392**, 794 (1998).]

to external magnetic field and thus for the CMR phenomenon. The effect is most pronounced near T_c.

W17.5 Faraday and Kerr Effects

Faraday Effects. *Faraday rotation* usually corresponds to the rotation by an angle θ_F of the plane of polarization of a linearly polarized EM wave due to its transmission through a magnetic material (or through a suitable medium in the presence of a magnetic field). Faraday rotation in nonmagnetic materials is described in Chapter W18. For the polar Faraday effect the Faraday rotation θ_F is usually defined to be one half of the change in phase angle ϕ between the right and left circularly polarized waves due to transmission. This is given by

$$\theta_F = \frac{\phi_+ - \phi_-}{2} = \frac{\pi(n_+ - n_-)d}{\lambda}, \tag{W17.9}$$

where λ is the wavelength in vacuum, d the sample thickness, and n_+ and n_- the real parts of the complex indices of refraction for right and left circularly polarized light, respectively. The difference $(n_+ - n_-)$ is called the *magnetic circular birefringence* (MCB).

When the absorption of light in the material is small, the Faraday rotation is

$$\theta_F = \frac{-\sigma'_{xy}d}{2nc\epsilon_0}. \tag{W17.10}$$

Here σ'_{xy} is the real part of σ_{xy}, an off-diagonal component of the complex conductivity tensor σ, n is the average of n_+ and n_-, and ϵ_0 is the permittivity of free space.[†] The quantity σ_{xy} is in general linear in the magnetization M of the material. When the

[†] In SI units the complex conductivity tensor $\sigma(\omega)$ is related to the complex dielectric function tensor $\epsilon_r(\omega)$ by $\sigma(\omega) = -i\omega\epsilon_0[\epsilon_r(\omega) - 1]$.

induced magnetization M is linear in the applied field H, as in paramagnetic and diamagnetic materials, both σ_{xy} and θ_F are also linear in H. The Faraday rotation is then expressed as

$$\theta_F = VHd, \tag{W17.11}$$

where V is the *Verdet constant*, usually expressed in the non-SI units of arcminutes/oersted·m [see Eq. (W18.12) and Table W18.1]. Note that V can depend on temperature through the magnetic susceptibility of the material and on the wavelength λ of the light through the optical constants of the material. In general, θ_F will be given by VMd, where M is the magnetization of the material.

Magnetic circular dichroism (MCD) corresponds to the difference in the absorption of light with right and left circular polarizations, also in the polar geometry. When the absorption is small, the difference in the absorption coefficients is given by

$$\alpha_+ - \alpha_- = \frac{\sigma''_{xy}}{c\epsilon_0}, \tag{W17.12}$$

where σ''_{xy} is the imaginary part of σ_{xy}. The MCD or Faraday ellipticity effect will also transform linearly polarized light into elliptically polarized light. When employed with circularly polarized x-rays, MCD is known as *XMCD spectroscopy* and is a technique that can be used to determine element-specific spin and orbital magnetic moments and their anisotropies in a quantitative manner. Since XMCD can have submonolayer sensitivity, it is a useful technique for studying magnetism at surfaces and in thin films, including the direction of easy magnetization in thin films and magnetic imaging.

For the longitudinal or transverse Faraday geometries, the observed effects are quadratic in M or H and are referred to as *magnetic linear birefringence* (MLB) and *magnetic linear dichroism* (MLD). These effects are not discussed here. For a summary of the MLB and MLD effects, see Craig (1991).

Kerr Effects. *Magneto-optical Kerr effects* (MOKEs) correspond to changes in the state of polarization of electromagnetic waves associated with their reflection from the surfaces of magnetic materials. The Kerr signal is proportional to the average surface magnetization of the material and to its reflectivity. Typical geometries for the polar, transverse, and longitudinal Kerr effects are illustrated schematically in Fig. 17.16.

In the *polar Kerr effect* geometry the magnetization **M** of the ferromagnet is oriented perpendicular to its surface. In this case, when the incident EM wave is linearly polarized, the reflected wave will be elliptically polarized and the major axis of the resulting ellipse will be rotated either clockwise or counterclockwise, depending on the direction of **M**. The *polar Kerr rotation* θ_K and *ellipticity* η_K are given by

$$\theta_K + i\eta_K = \frac{i\epsilon_{xy}}{\sqrt{\epsilon_{xx}}(\epsilon_{xx} - 1)}, \tag{W17.13}$$

where the complex quantities ϵ_{xx} and ϵ_{xy} are diagonal and off-diagonal components of the complex dielectric function $\epsilon = \epsilon_1 + i\epsilon_2$. The angle of rotation of the major axis of the ellipse is

$$\theta_K = \frac{\lambda\sigma''_{xy}}{2\pi nc\epsilon_0}. \tag{W17.14}$$

This is similar in form to θ_F for the Faraday effect given in Eq. (W17.10), but with two important differences: the thickness d in θ_F is replaced here by the wavelength λ of the incident light, and the real part σ'_{xy} of σ_{xy} appearing in θ_F is replaced here by the imaginary or absorptive part σ''_{xy}. Note that for a transparent material, σ''_{xy}, and hence θ_K, are both zero. The polar Kerr effect has the largest response of the three Kerr effects and, in addition, probes the component of the magnetization perpendicular to the surface of the material. Only the polar Kerr effect is nonzero for normal incidence.

In the *transverse Kerr effect* geometry, **M** is parallel to the surface of the magnetic material and is perpendicular to the incident plane of polarization of the EM wave. In the *longitudinal Kerr effect* geometry, **M** is also parallel to the surface but lies in the incident plane of polarization. The *Voigt effect* has the same geometry as the transverse Kerr effect but corresponds to the case of reflection from a nonabsorbing medium.

If the **E** field of the incident EM wave is perpendicular to the plane of incidence in the transverse Kerr geometry, the reflectivity R will not be affected significantly by the magnetization of the material. If, however, the **E** field lies in the plane of incidence, R will depend linearly on **M**. It follows therefore that when unpolarized light is incident on an absorbing magnetic material, the reflectivity R measured for different regions will depend on the local direction of **M** (i.e., on the magnetic domain structure). This effect can be employed for the observation of magnetic domains in magnetic recording media. The Voigt effect is observed when the magnetic material is nonabsorbing. In this case the amount of linearly polarized light that is converted upon reflection to elliptically polarized light will be proportional to M^2. This corresponds to a type of *magnetic birefringence*.

The *surface* MO Kerr effect (SMOKE) is often used in conjunction with ultrahigh-vacuum techniques to probe the magnetic properties of surfaces. Phenomena that have been studied include the existence of surface magnetism, the magnetic anisotropy induced by and associated with surfaces, and the Curie temperature T_C as a function of film thickness. Figure W17.4 shows magnetization curves of Fe/Mo/Fe multilayer films obtained via SMOKE. A square hysteresis loop is obtained when the two Fe layers are ferromagnetically aligned via coupling through the Mo layer. When

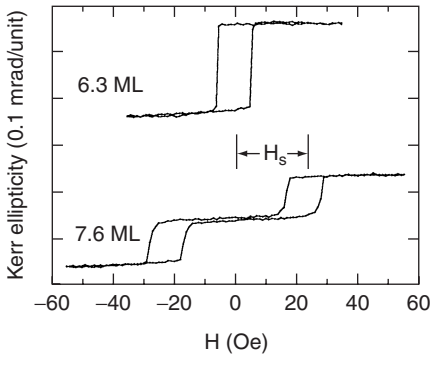

Figure W17.4. Magnetization curves of Fe/Mo/Fe multilayer films obtained via SMOKE. A square hysteresis loop is obtained when the two Fe layers are ferromagnetically aligned via coupling through the Mo layer. When the Mo layer is thicker, 7.6 monolayers (ML), the Fe layers couple antiferromagnetically and the switching field H_s is required to return their alignment to ferromagnetic. (From Z. Q. Qiu and S. D. Bader, *Mater. Res. Soc. Bull.*, **20**(10), 34 (1995).)

the Mo layer is thicker (e.g., 7.6 monolayers) the Fe layers couple antiferromagnetically and the switching field H_s is required to return their alignment to ferromagnetic.

W17.6 Details on Dynamic Magnetic Effects

Eddy Currents. The eddy currents generated in, for example, a long cylinder of a magnetic material by a changing magnetic field $H(t)$ can be calculated from electromagnetic theory using Faraday's law of induction. When the cylinder consists of a single magnetic domain and when the field H penetrates the cylinder completely, the power loss per unit volume of the material due to the eddy currents can be expressed in terms of the changing magnetization M by

$$p = \frac{P}{V} = \frac{\mu_0^2 r^2}{8\rho}\left(\frac{dM}{dt}\right)^2. \tag{W17.15}$$

Here r is the radius of the cylinder and ρ is the electrical resistivity of the material. When $M(t) = M_0 e^{-i\omega t}$, the power loss p will be proportional to $\omega^2 M_0^2$. From this expression it is clear that eddy current losses in magnetic materials can be reduced by increasing the resistivity ρ of the material.

When the cylinder has a magnetic microstructure consisting of more than one magnetic domain, the eddy current losses will be increased over the single-domain case due to localization of the currents induced in the vicinity of the domain walls. As domain walls move or as the magnetization within a domain rotates, the local time-dependent changes in M and H induce localized eddy currents whose distributions are very difficult to calculate. Localized eddy current losses will occur even if the magnetization loop is traversed slowly.

When the rates of change of H and M are very large, as at high frequencies, the magnetic fields resulting from the induced eddy currents will oppose the change in the applied field, thereby screening the applied field H from the center of the solid. This is known as the *skin effect* and is most pronounced in conducting materials. The applied field H and the corresponding changes in the magnetization M will decrease to $1/e$ of their values at the surface within a distance δ known as the *skin depth*, given by

$$\delta = \sqrt{\frac{2\rho}{\omega\mu}}. \tag{W17.16}$$

Here μ is the magnetic permeability of the material. Since Fe is a magnetic material widely used in the cores of transformers, it is useful to note that $\delta \approx 0.9$ mm at $f = 60$ Hz, using $\rho(\text{Fe}) = 1 \times 10^{-7}$ Ω·m and $\mu(\text{Fe})/\mu_0 \approx 500$ at $T = 300$ K. To allow for complete penetration of the magnetic field, transformer cores are therefore formed from thin, laminated sheets of Fe. In applications of magnetic materials at microwave frequencies, it is usually advantageous to employ materials with high resistivities such as magnetic ferrites in order to reduce the eddy current losses.

Ferromagnetic Resonance. The magnetization vector $\mathbf{M}$ of a magnetic solid will undergo precession around the direction of the total static magnetic field $\mathbf{H}_{\text{tot}}$, as illustrated schematically in Fig. W17.5. The sources of $\mathbf{H}_{\text{tot}}$ can correspond to a combination of an applied field $\mathbf{H}$ and internal fields such as a demagnetizing field $\mathbf{H}_D$, an effective

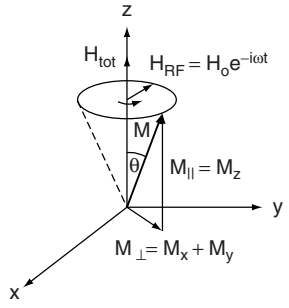

Figure W17.5. Precession of the magnetization vector **M** of a magnetic solid around the direction of a magnetic field $\mathbf{H}_{\text{tot}}$. An external RF magnetic field $H_{\text{RF}}(t)$ acting at right angles to the static field $\mathbf{H}_{\text{tot}}$ is also shown.

anisotropy field $\mathbf{H}_a$, and an effective molecular field $\mathbf{H}_{\text{eff}} = \mathbf{B}_{\text{eff}}/\mu_0$. This precessional motion is a consequence of the torque per unit volume $\boldsymbol{\tau}/V = \mu_0 \mathbf{M} \times \mathbf{H}_{\text{tot}}$ exerted on **M** by $\mathbf{H}_{\text{tot}}$ as described by the equation of motion:

$$\frac{d\mathbf{M}}{dt} = -\gamma\mu_0 \mathbf{M} \times \mathbf{H}_{\text{tot}}. \tag{W17.17}$$

Here $\gamma = ge/2m$ is the gyromagnetic ratio and g is the Landé g factor, given for an atom in Eq. (9.6). This expression is valid in the absence of any damping of the motion of **M**. For a long cylinder the precession of **M** occurs at an angular frequency given by

$$\omega = \gamma\mu_0 H_{\text{tot}}. \tag{W17.18}$$

In the presence of damping forces acting on **M**, energy will be transferred from the spin system (i.e., the magnetization) to the lattice or to the electrons. Examples of possible loss mechanisms include eddy currents, excitation of spin waves, and so on. These energy losses can be compensated by the application of a transverse radio-frequency magnetic field $H_{\text{RF}}(t) = H_0 e^{-i\omega t}$ acting at right angles to the static field $\mathbf{H}_{\text{tot}}$ (see Fig. W17.5). As the frequency ω of H_{RF} is varied, resonance will occur at $\omega = \omega_r = \gamma\mu_0 H_{\text{tot}}$, at which point the spin system absorbs the maximum amount of energy from the microwave field. For $g = 2$ and $\gamma = 1.76 \times 10^{11}$ C/kg, the resonant frequency is $\omega_r = 2.21 \times 10^{11}$ Hz in a typical field of $H_{\text{tot}} = 10^3$ kA/m. This frequency corresponds to a wavelength $\lambda = 8.54$ mm (i.e., to microwave radiation). The full-width at half maximum of the resonance peak in χ'' is proportional to the magnitude of the damping while the magnitude of χ'' at resonance is inversely proportional to the damping.

One important application of the resonant absorption of EM radiation by a ferromagnet (i.e., of a *ferromagnetic resonance* measurement) is the determination of the g factor, $g = 2m\omega_r/e\mu_0 H_{\text{tot}}$. Results obtained for the $3d$ transition metal ferromagnets are $g(\text{Fe}) = 2.10$, $g(\text{Co}) = 2.18$, and $g(\text{Ni}) = 2.21$. These values indicate that the magnetization in these materials is associated primarily with the spin magnetic moment m_{spin} of the electron. In fact, measurements of the g factor by ferromagnetic resonance allow the ratio $\varepsilon = m_{\text{orb}}/m_{\text{spin}}$ of the components of the magnetic moment of the material to be determined using the relationship $g = 2(1 + \varepsilon)$. For these three elemental ferromagnets the ratios $\varepsilon(\text{Fe}) = 0.05$, $\varepsilon(\text{Co}) = 0.09$, and $\varepsilon(\text{Ni}) = 0.105$ are

obtained. Since in these metallic ferromagnets the alternating field $H_{\mu\text{wave}}$ penetrates the material only to within the skin depth δ at the surface, defined in Eq. (W17.16), surface preparation is very important.

Additional parameters that can be obtained from measurements of ω_r in ferromagnets and ferrimagnets are the magnitudes of the effective anisotropy field H_K and the effective molecular field H_{eff}. For example, the resonant frequency due to magnetic anisotropy effects alone is obtained when $H = 0$ and $H_{\text{tot}} = H_a$ in Eq. (W17.18). With $H_K = 2K/\mu_0 M_s$, measurement of $\omega_r = g\mu_0 H_K$ can yield K if M_s is known from independent measurements.

In antiferromagnets it is possible for the magnetizations of the two spin sublattices to precess at the same frequency. For a uniaxial antiferromagnet in zero applied magnetic field, the resonant frequency is

$$\omega_r = \gamma\mu_0 \sqrt{H_K(H_K + 2H_{\text{eff}})}, \tag{W17.19}$$

where H_K is the effective anisotropy field and H_{eff} is the effective molecular field. Values of H_K and H_{eff} obtained for the antiferromagnet MnF_2 via antiferromagnetic resonance are 700 and 43,000 kA/m, respectively.

For ferrimagnets the resonance occurs in essentially the same way as in ferromagnets as long as $H_{\text{eff}} \gg H$ or H_K. The resonant frequency can lie in the range from microwave to infrared frequencies, depending on the particular mode excited.

Magnetic Relaxation. The time-dependent changes in the magnetization M which lag behind changes in an applied magnetic field H are known either as *magnetic relaxation* or as the *magnetic aftereffect*. Eddy currents can also lead to relaxation effects and have already been discussed. These magnetic relaxation effects can be reversible as long as no irreversible changes in the magnetic microstructure have occurred due to diffusion or to macroscopic structural changes.

Following a discontinuous change in H, changes in M can exhibit exponential time dependencies expressed either by

$$M(t) = M_0(1 - e^{-t/\tau}) \tag{W17.20a}$$

or by

$$M(t) = M_0 e^{-t/\tau}, \tag{W17.20b}$$

where τ is the time constant for the relaxation process. The mathematical formalism for the description of magnetic relaxation is similar to that employed in Chapter W10 for a description of the anelastic mechanical properties of materials. The energy losses associated with periodic magnetic-relaxation processes typically occur at frequencies $\omega = 2\pi/\tau$, which are lower than those associated with ferromagnetic resonance. The characteristic time τ for magnetic relaxation depends on the nature of the microscopic processes controlling the relaxation process. The lifetime τ can be temperature dependent if the process is thermally activated. Examples of such processes include diffusion of atoms or the hopping of electrons from atom to atom.

A physical mechanism for the magnetic relaxation observed in BCC α-Fe was first proposed by Snoek.[†] The *Snoek effect* is also discussed in Chapter 10, where

[†] J. Snoek, *Physica*, VI, 591 (1939).

its influence on the elastic properties of α-Fe is described. Relaxation of the elastic properties is proposed to be due to the redistribution of C or N atoms among the available interstitial sites in the BCC crystal structure. The same redistribution of C or N affects the magnetization of the material through the magnetoelastic interaction and so is related to the magnetostriction of α-Fe. An alternative explanation for the origin of the observed magnetic relaxation as suggested by Néel involves the effect on the anisotropic exchange interaction between Fe atoms due to the intervening interstitial C or N atoms.

Relaxation of the magnetization can also result from the thermally activated rotations of the magnetic moments of magnetic domains, of magnetic particles, or even of individual spins over energy barriers, which can be due, for example, to the effects of magnetic anisotropy. In small magnetic particles this effect is closely related to superparamagnetism. In the amorphous magnetic materials known as *spin glasses*, relaxation of the remanent magnetization occurs via the activation of single spins or clusters of strongly interacting spins over local energy barriers so that their magnetic moments point in energetically favorable directions. There is often a broad distribution of time constants associated with these processes so that the "freezing" process does not follow a simple thermal-activation law with a single time constant or activation energy. This process of spin glass "freezing" occurs over a wide range of temperatures.

The term *magnetic viscosity* is often used to describe the magnetic relaxation of collections of small magnetic particles or of spin glasses, for which there can exist a wide distribution of relaxation times resulting from a corresponding broad distribution of energy barriers to magnetization rotation, domain wall motion, and so on. In this case, the time dependence of the magnetization is often approximated by

$$M(t) = M_0 - S \ln(t/\tau_0), \tag{W17.21}$$

where M_0 and τ_0 are constants and $S = -dM/d(\ln t)$ is the magnetic viscosity. There are good reasons, however, to avoid the use of this simple logarithmic time dependence for $M(t)$ because such an expression does not in general fit experimental observations at times that are either short or long compared to the time duration t_{exp} of the measurement (Aharoni, 1996, pp. 100–105). Relaxation processes for which $\tau \ll t_{\text{exp}}$ or $\tau \gg t_{\text{exp}}$ will clearly fall outside the range of validity of Eq. (W17.21).

In many materials the magnetic viscosity levels off to a constant value at low temperatures, a result that is contrary to what is expected from thermally activated processes. This effect has been attributed to the quantum-mechanical reversal of the magnetization (i.e., to quantum tunneling of the magnetization).

Magnetomechanical Damping. The energy losses associated with mechanical vibrations in magnetic materials, referred to as *magnetomechanical damping*, are generally larger than those observed in nonmagnetic materials. The stresses causing the vibrations in a magnetic material lead to strains, which in turn cause changes in the magnetization via magnetostriction. The result is that by Faraday's law, oscillatory stresses can result in the generation of eddy currents with their associated losses in a magnetic material. Losses due to domain wall motion can also result from applied stresses.

TABLE W17.2 Technologically Important Magnetic Materials

Material	Magnetically Hard or Soft	Applications
Metals		
Steels (alloyed with W, Cr, etc.)	Hard	Permanent magnets
Fe particles (oxide-coated)	Hard	Magnetic recording media
Fe_xNi_{1-x} alloys: 78 Permalloy, $Fe_{0.22}Ni_{0.78}$; Supermalloy, $Fe_{0.16}Ni_{0.79}Mo_{0.05}$; Invar, $Fe_{0.65}Ni_{0.35}$	Soft	Electromagnetic devices, magnetic recording heads, precision instruments
Mumetal: $\approx Fe_{0.18}Ni_{0.77}Cu_{0.05}$	Soft	Magnetic shielding, transformer cores
Co alloys (CoCr, etc.)	Hard	Magnetic recording media
$Fe_{1-x}Si_x$	Soft	Transformer cores
Fe:Si:Al alloys: Sendust,[a] 85Fe10Si5Al	Soft	Magnetic recording heads
Alnico alloys: Alnico 5,[a] 51Fe14Ni8Al24Co3Cu	Hard	Permanent magnets
Amorphous rare earth–transition metal alloys	Soft	Magneto-optical recording media
Amorphous Fe:B:Si:C alloys	Soft	Magnetostrictive elements
Intermetallic compounds		
$SmCo_5$ and Sm_2Co_{17}	Hard	Permanent magnets
$Nd_2Fe_{14}B$	Hard	Permanent magnets
$TbFe_2$ and $(Tb_{0.3}Dy_{0.7})Fe_2$ (Terfenol-D)	Soft	Magnetostrictive elements
Ceramic compounds		
γ-Fe_2O_3	Hard	Magnetic recording media
CrO_2	Hard	Magnetic recording media
$Mn_{1-x}Zn_xFe_2O_4$	Soft	Magnetic recording heads
$Y_3Fe_5O_{12}$ (YIG)	Soft	Microwave technology
$BaO{\cdot}6Fe_2O_3$ or $SrO{\cdot}6Fe_2O_3$ ($BaFe_{12}O_{19}$, $SrFe_{12}O_{19}$)	Hard	Permanent magnets, magnetic recording media

[a]Composition given in weight percent.

W17.7 Technologically Important Magnetic Materials

See Table W17.2 for magnetic materials described in Chapters 17 and W17.

W17.8 Details on Permanent-Magnet Materials

To illustrate the operation of a permanent magnet, consider a toroidal magnet producing a magnetic field H_g in an airgap, as shown schematically in Fig. W17.6*a*. The introduction of the air gap leads to the presence of a demagnetizing field $\mathbf{H}_D = -N\mathbf{M}$ inside the magnet, directed opposite to both $\mathbf{M}$ and $\mathbf{B}$. When no external field $\mathbf{H}$ is applied to the magnet, its operating point will lie somewhere on the portion of the B–H or M–H loop in the second quadrant.

The portion of the B–H loop in the second quadrant which determines the operation of a permanent magnet is the *demagnetization curve*, shown in Fig. W17.6*b*. Note that

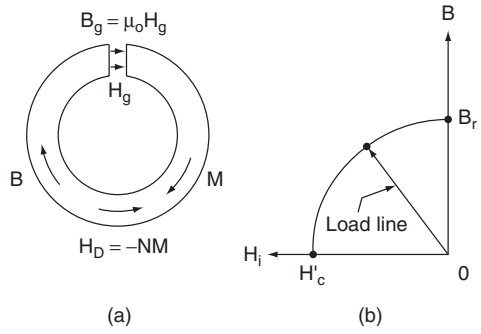

Figure W17.6. Permanent magnet: (*a*) configuration of a toroidal permanent magnet supplying a magnetic field H_g to an air gap; (*b*) portion of the B–H loop that determines operation of the permanent magnet, which is the demagnetization curve in the second quadrant.

it is standard practice to plot B–H curves for permanent-magnet materials rather than the usual M–H magnetization curves. Here the magnetic induction $\mathbf{B} = \mu_0(\mathbf{H}_i + \mathbf{M})$ in the material is shown plotted versus the internal magnetic field $\mathbf{H}_i$. The demagnetization curve extends from the remanent induction $B_r = \mu_0 M_r$ at $H_i = 0$ down to $H_i = -H'_c$, the coercive field corresponding to $B = 0$. Note that B_r is the maximum flux density that the magnet can produce under closed-circuit conditions (i.e., in the absence of an air gap). The operating point for the magnet in the absence of an external magnetic field is determined by the presence of the air gap and the resulting demagnetizing field $\mathbf{H}_D$. In this case the internal magnetic field is given by

$$\mathbf{H}_i = \mathbf{H}_D = -N\mathbf{M}. \tag{W17.22}$$

The operating point is thus not at B_r but rather, at the point where the magnetic induction $B(< B_r)$ is given by

$$\mathbf{B} = \mu_0(\mathbf{H}_D + \mathbf{M}) = \mu_0(1 - N)\mathbf{M}. \tag{W17.23}$$

Here $1 \geq N \geq 0$ is the demagnetizing factor for the magnet with the air gap. The magnetization M is less than M_r, due to the presence of $\mathbf{H}_D$. Note that in the air gap $B_g = \mu_0 H_g \approx B$ if the gap is narrow enough so that the fringing magnetic fields are small.

For a given amount or volume of magnetic material, the highest field H_g in a given air gap is achieved when the *energy density product* (BH) of the magnetic induction B and the field H_i inside the magnet is maximized. The energy density product is also known as the *strength* of the magnet. The operating point of the magnet should therefore lie as close as possible to the point on the B–H curve for which (BH) is largest [i.e., at $(BH)_{\max}$]. The actual energy stored per unit volume is $BH/2$. In this way the permanent magnet needed to produce a given magnetic field can be as small as possible.

The actual point of operation of the permanent magnet is determined by the demagnetizing factor N of the magnet with the air gap and corresponds to the magnetic induction given in Eq. (W17.23). The slope of the line connecting the origin to the operating point on the B–H curve is therefore

$$s = \frac{B}{H_{\text{int}}} = \frac{-\mu_0(1 - N)}{N}. \tag{W17.24}$$

This is the *load line* of the magnet as shown in Fig. W17.6. Slopes of $s = \infty$ and $s = 0$ correspond, respectively, to the limiting values of $N = 0$ and $N = 1$. For $N \ll 1$, the slope is given approximately by $s = -\mu_0/N$.

Transition Metal Alloys. The ferromagnetic $3d$ transition metals Fe, Co, and Ni are present in essentially all of the widely used permanent-magnet materials listed in Table W17.3, either in alloys with each other or with other transition metals, in intermetallic compounds with rare earth metals, or in ceramic compounds. The magnetic anisotropy field H_K for pure Fe is only ≈ 40 kA/m, which eliminates pure Fe as a material for most permanent-magnet applications due to its relatively low coercive field H_c. The precipitation-hardened alloys based primarily on Fe, Ni, Al, and Co, as well as some steels that have permanent-magnet applications, are discussed next.

Precipitation-Hardened Alloys. *Precipitation hardening* in the case of magnetic materials refers to the use of heat treatments to enhance the magnetic hardness of the material by the precipitation of a second phase which can pin domain walls and hence increase H_c. By varying both the specific processing treatments employed and the composition, the alloys known in the United States as Alnico and based on Fe, Al, Ni, Co, and so on, can be prepared with magnetic properties, which have led to their widespread use in permanent magnets. Many other transition metal alloys based on Fe, Co, or Ni can also undergo precipitation hardening for use in permanent magnets.

TABLE W17.3 Properties of Permanent-Magnet Materials

Material	$(BH)_{\max}$ (kJ/m^3)[a]	B_r (T)	H_c'[b] (kA/m)	T_C (K)
Transition Metal Alloys				
Alnico 5[c]: (51Fe, 14Ni, 8Al, 24Co, 3Cu)	35.8	1.25	43.8	1120
Steels[c]				
Cobalt steel (35Co, 0.7C, 4Cr, 5W, bal. Fe)	7.7	0.95	19.1	
Tungsten steel (5W, 0.3Mn, 0.7C, bal. Fe)	2.5	1.03	5.6	
Rare Earth–Transition Metal Intermetallic Compounds				
Nd–Fe–B[d]	200–380	1.0–1.4	700–1000	580
$SmCo_5$[e]	130–180	0.8–0.9	600–670	990
$Sm(Co,Fe,Cu,Zr)_7$[e]	200–240	0.95–1.15	600–900	1070
Ceramics				
$BaO{\cdot}6Fe_2O_3$[d]	28	0.4	250	720

[a]Note that 1 kJ/m^3 = 1 kA·T/m.
[b]The quantity H_c' is the coercive field corresponding to $B = 0$.
[c]Data from D. R. Lide and H. P. R. Frederikse, eds., *CRC Handbook of Chemistry and Physics*, CRC Press, Boca Raton, Fla., 1994, pp. 12–113. The alloy composition is given in weight percent. See the Handbook for methods of fabrication.
[d]Commercial material from Magnet Sales & Manufacturing Catalog.
[e]Data from K. H. J. Buschow, *Rep. Prog. Phys.*, **54**, 1123 (1991). $Sm(Co,Fe,Cu,Zr)_7$ is a two-phase material which can be thought of as a composite of $SmCo_5$- and Sm_2Co_{17}-type phases.

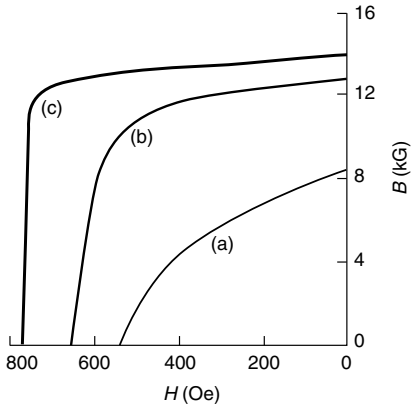

Figure W17.7. Demagnetization curves of an Alnico alloy, 51.8Fe, 7.5Al, 23Co, 3Cu, 0.7Nb in wt %, cooled from $T = 1250°C$ and annealed at $T = 560$ to 590°C: (*a*) randomly oriented grains with no heat treatment in a magnetic field; $(BH)_{max} = 14$ kJ/m^3; (*b*) randomly oriented grains heat-treated in a magnetic field; $(BH)_{max} = 43$ kJ/m^3; (*c*) columnar grains heat-treated in a magnetic field; $(BH)_{max} = 69$ kJ/m^3. [From J. E. Gould, *Proc. I.E.E.*, **106A**, 493 (1959). Copyright 1959, IEE Publishing.]

A typical precipitation-hardened alloy is Alnico 5, which has the composition (in weight percent) 51Fe, 14Ni, 8Al, 24Co, and 3Cu. The extrinsic magnetic properties of Alnico 5 are listed in Table W17.3. Due to their high T_C values of ≈ 1120 K, Alnico 5 and similar alloys have higher maximum operating temperatures than most other permanent magnets. Following quenching from $T \approx 1200°C$ and annealing in the range 500 to 600°C, these alloys consist of highly magnetic rodlike particles of α-Fe embedded in a weakly magnetic matrix of Ni and Al. When cooled slowly from $T = 1200°C$ to below T_C in a magnetic field, the precipitation occurs in such a way that the long axes of the particles become aligned with each other, thus increasing the shape magnetic anisotropy of the material and its coercive field. This is illustrated in Fig. W17.7, where the demagnetization curves for an Alnico alloy are shown following three different types of thermomagnetic treatment.

Alnico alloys have high values of B_r, due to their high Fe contents but have lower coercive fields H_c compared to the other permanent-magnet materials listed in Table W17.3. The magnitude of the coercive fields of Alnico alloys can be attributed to the pronounced shape anisotropy of the magnetic particles. The maximum magnetic anisotropy attainable in these alloys is determined by the difference $(N_\perp - N_\parallel)$ of the demagnetization coefficients of the particles [see Eq. (17.16)]. Even better magnetic properties [i.e., higher B_r, $(BH)_{max}$, and H'_c] can be found in highly [100]-oriented alloys with columnar microstructure obtained by controlled solidification from the melt.

Co is apparently required for the appearance of significant magnetic anisotropy in these alloys, while additions of Nb and Ti can also lead to increased values of H'_c. The physical reasons for these changes are not clear.

Steels. Steels alloyed with W, Cr, and Co have been used extensively as permanent magnets. Given the proper heat treatment, these alloying elements can react with the C in the steel, forming precipitates of carbides of W, Cr, and Co which act to impede the motion of domain walls. Anisotropy effects associated with the shapes of these carbide precipitates are apparently not as strong as in typical Alnico alloys, which

have coercive fields that are higher by a factor of 3 or more. The low values of H_c in steels limit their attainable values of $(BH)_{\max}$.

The martensitic lattice transformations from the FCC γ-phase to the BCC α-phase that occur in these steels upon cooling lead to lattice distortions due to the resulting high internal stresses. The magnetic anisotropy of magnet steels is therefore enhanced by stress-related magnetostrictive effects.

Rare Earth–Transition Metal Intermetallic Compounds. The most attractive materials for current high-performance permanent magnets are the intermetallic compounds based on rare earths and the ferromagnetic transition metals Fe and Co. These materials, sometimes referred to as *supermagnets*, possess the highest-known coercive fields, $H_c \approx 1100$ kA/m, and energy products, $(BH)_{\max} \approx 300$ kJ/m^3. The low-symmetry hexagonal or tetragonal crystal structures of these materials expose the rare earth ions to the high magnetocrystalline anisotropy needed for enhancing the coercive field. The transition metal components keep T_C sufficiently high for practical applications. An important advantage of the rare earth–based permanent-magnet materials is that they can be used to generate the same magnetic fields as iron-core electromagnets, which are 10 times as massive. This feature has made possible miniaturized electrical motors and, in general, smaller and lighter electromagnetic devices and products. Larger magnetic inductions, in the range 3 to 10 T, require the use of superconducting magnets. The important intermetallic compounds $SmCo_5$, Sm_2Co_{17}, and $Nd_2Fe_{14}B$ are discussed next.

$SmCo_5$ and Sm_2Co_{17}. The first permanent-magnet materials, consisting of rare earth–transition metal (RE–TM) intermetallic compounds and based on Sm and Co, were discovered in the early 1960s. These materials have high values of M_{sat}, due to the ferromagnetic coupling of the Sm and Co spins. This is not found to be the case in alloys containing heavy rare earths, such as Gd, where the RE–TM coupling is antiferromagnetic. The substitution of other magnetic 3*d* transition metals, such as Fe, Mn, Cr, or Ni for Co, in these RE–TM compounds has not been successful, due to the resulting low T_C values or low magnetic anisotropies. The high T_C values of these alloys make them attractive for use in applications in which the operating temperature of the magnet is relatively high.

According to the Hume–Rothery rules described in Chapter 12, the fact that the RE ionic radii are much greater than those of the TM ions strongly limits the possibility of the formation of RE–TM solid solutions. Instead, a series of intermetallic compounds are formed. The crystal structure of $SmCo_5$ is hexagonal and that of Sm_2Co_{17} is trigonal (rhombohedral) (Fig. W17.8). In the $SmCo_5$ structure the planes containing the Sm ions and twice as many Co ions lie between adjacent planes containing only Co atoms. The Sm_2Co_{17} structure is derived from the $SmCo_5$ structure by an ordered replacement of one-third of the Sm ions by pairs ("dumbbells") of Co ions that are aligned along the *c* axis.

The overall magnetocrystalline anisotropies of both Sm–Co compounds is uniaxial, with $SmCo_5$ having the largest value observed for any magnetic material, corresponding to an effective magnetic anisotropy field $H_K \approx 3.2 \times 10^4$ kA/m. In the Sm_2Co_{17} structure the dumbbell pairs of Co atoms prefer to have their magnetic moments lying in the basal plane, thereby reducing the overall magnetic anisotropy of the material.

Recently, Fe-based compounds such as $Sm_2Fe_{17}N_{3-x}$ have been developed with high T_C values, up to 749 K, strong uniaxial anisotropy, and high saturation magnetization.

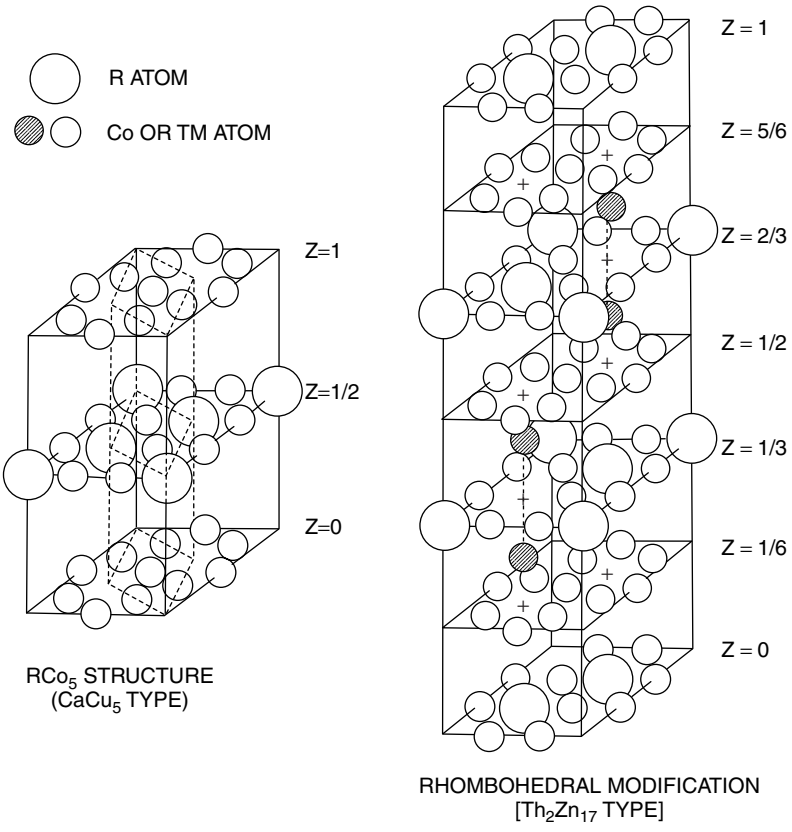

Figure W17.8. Crystal structures of the intermetallic compounds hexagonal $SmCo_5$ and rhombohedral Sm_2Co_{17}. The substituted "dumbbell" Co ions in Sm_2Co_{17} appear crosshatched. (From K. Kumar, *J. Appl. Phys.*, **63**, R13 (1988). Copyright 1988 by the American Institute of Physics.)

The N atoms enter octahedral interstitial sites in the structure. In materials such as $Sm_2Fe_{15}Ga_2C_{3-x}$, C atoms can serve the same purpose. In addition, Ga has been substituted for some of the Fe in order to increase T_C and the uniaxial anisotropy field. The presence of the interstitial N or C atoms expands the structure and apparently has the effect of strengthening the magnetism by supporting the formation of ferromagnetic networks of Fe atoms in these materials.

The best commercially available materials are precipitation-hardened composites consisting of a Sm_2Co_{17}-type phase embedded in a $SmCo_5$-type matrix. These materials combine the high M_{sat} value of Sm_2Co_{17} with the high magnetic hardness of $SmCo_5$. The high observed values of H_c result from the alignment of the easy axes of the particles parallel to each other in the material. These composites have the approximate composition $SmCo_{7.7}$ and also typically contain some Fe, Cu, and Zr atoms replacing some of the Co.

Powder metallurgy techniques are used in the fabrication of these magnets. The elements are first melted together, then ground into micrometer-sized particles. The c axes of the particles are aligned magnetically in a magnetic field. The particles are then densified by sintering. Finally, thermal treatments are utilized for the optimization of H_c.

$Nd_2Fe_{14}B$. The intermetallic compound $Nd_2Fe_{14}B$, discovered in 1984, exhibits the most desirable magnetic properties of all permanent-magnet materials at room temperature (see Table W17.3). Since it is based on Fe, $Nd_2Fe_{14}B$ has the advantage of being less expensive than the Co-based materials discussed earlier. In addition, Nd^{3+} has a larger magnetic moment than Sm^{3+} and couples ferromagnetically to the magnetic moments of the Fe atoms, leading to a higher magnetization. The magnetic coupling between the Nd $4f$ electrons and the Fe $3d$ electrons is believed to be indirect, occurring not via the RKKY interaction through the conduction electrons but instead, through the rare earth $5d$ electrons. The ion Nd^{3+} has an outer electron configuration $4f^3$ and contributes one $5d$ and two $6s$ electrons to the conduction bands. The Fe magnetic moment is $\approx 2.1\mu_B$, close to the value found in pure α-Fe.

$Nd_2Fe_{14}B$ has a complicated tetragonal unit cell with dimensions $a = 0.88$ nm and $c = 1.22$ nm and containing 68 atoms (i.e., four formula units). The crystal structure presented in Fig. W17.9 is essentially a layered one, with sheets of Nd and B atoms

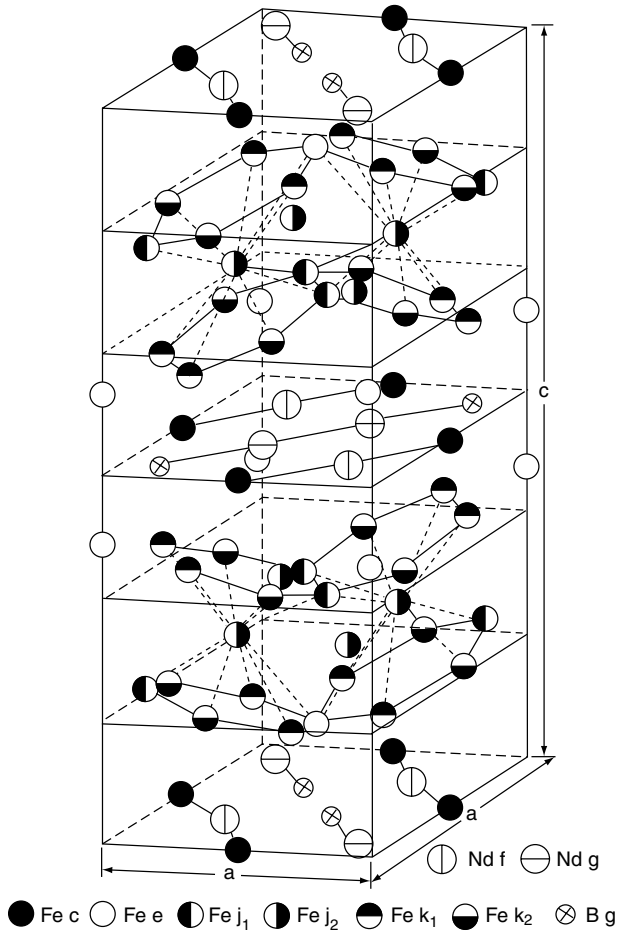

Figure W17.9. Tetragonal unit cell of $Nd_2Fe_{14}B$. The structure is essentially a layered one, with sheets of Nd and B atoms (and some Fe atoms) lying between close-packed double layers of Fe atoms. (From J. F. Herbst, *Rev. Mod. Phys.*, **63**, 819 (1991). Copyright 1991 by the American Physical Society.)

(and some Fe atoms) lying between close-packed double layers of Fe atoms. Six crystallographically distinct positions for the Fe atoms and two for the Nd atoms exist in this structure. The origin of the strong uniaxial magnetocrystalline anisotropy of $Nd_2Fe_{14}B$ is the low symmetry of the Nd sites and, apparently, the interaction of the Nd^{3+} ions with the resulting strong crystal fields.

Despite the crystal-field effects, the Nd^{3+} ions retain their full magnetic moment due to the strong on-site spin–orbit interaction (i.e., the orbital angular momentum **L** is not quenched). In this structure the Nd atoms lie within hexagonal prisms of Fe atoms while the B atoms lie within trigonal prisms of Fe atoms. These trigonal prisms are also a common and fundamental feature of transition metal–metalloid structures such as those found in the FeB and Fe_3C systems. The role of the B in $Nd_2Fe_{14}B$ is to produce a low-symmetry crystal structure without causing an appreciable reduction of the magnetization of the material.

The material $Nd_2Fe_{14}B$ is a uniaxial ferromagnet with a fairly low T_C value of 585 K and with the all Nd and Fe spins aligned at room temperature parallel to the c axis, the easy axis for the magnetization **M**. The resulting saturation magnetization is quite high, $M_{\text{sat}} = 1270$ kA/m, even higher than the value 800 kA/m for $SmCo_5$. As a measure of the strength of the uniaxial magnetic anisotropy, the effective magnetic anisotropy field H_K is about 7200 kA/m.

NdFeB magnet material can be formed by rapid solidification, (i.e., by melt spinning and quenching into ribbon form) or by the pressing and sintering of powder material. The ribbon material has a metastable microstructure that is very sensitive to the quenching rate. The optimum material consists of 20-nm grains of $Nd_2Fe_{14}B$ surrounded by an approximately 2-nm-thick amorphous intergranular phase. The grain boundaries pin the domain walls, thereby impeding their motion and increasing the coercive field. Processing is necessary to transform the brittle ribbon material into the final dense form, with the two-phase microstructure suitable for permanent-magnet applications.

Improvements in the properties of $Nd_2Fe_{14}B$ can be achieved by introducing a variety of alloying elements (e.g., substituting Co for some of the Fe atoms raises T_C, replacing some of the Nd by Dy or Gd atoms enhances the anisotropy, etc.). Currently used NdFeB magnet materials are based on $Nd_2Fe_{14}B$ but actually correspond to a range of compositions and microstructures.

Ceramics. Permanent magnets based on the ceramic compounds barium ferrite, $BaO{\cdot}6Fe_2O_3$ ($BaFe_{12}O_{19}$), strontium ferrite, $SrO{\cdot}6Fe_2O_3$, and their solid solutions have the advantages of very high coercive fields, $H_c \approx 200$ kA/m, due to the strong uniaxial magnetocrystalline anisotropy field of this material, $H_K \approx 1300$ kA/m. They also possess high environmental stability, due to the absence of problems associated with oxidation. The magnetic properties depend critically on the sintering of the ceramic powders to obtain bulk material. The fact that H_c is typically well below H_K may be due to the platelet shape of the particles and the fact that the resulting shape anisotropy opposes the larger uniaxial magnetocrystalline anisotropy. This issue is also mentioned in Section W17.9, where the use of barium ferrite in magnetic recording media is discussed.

These ceramic materials are ferrimagnetic and thus have relatively low values of B_r and M_{sat}. Their high values of H_c and low cost have nevertheless led to widespread applications in permanent magnets and in magnetic recording media. Their high

resistivities, $\rho \approx 10^2$ to $10^7 \Omega \cdot m$, make them useful for high-frequency applications. The flexible magnets consisting of a magnetic powder such as barium ferrite bonded in a flexible binder are an interesting and ubiquitous application of these ceramic materials.

W17.9 Details on Magnetic Recording Materials

Particulate Magnetic Recording Media. The intrinsic shape anisotropy of small, elongated magnetic particles can be a convenient and stable source of magnetic anisotropy for controlling H_c. Particulate recording media therefore often consist of elongated magnetic particles dispersed and embedded (20 to 50% of total volume) in a suitable medium consisting of organic components (polymers or resins), which is then applied as a 0.2 to 10-μm-thick film to a nonmagnetic support (e.g., a tape or disk). For superior recording performance it is clearly desirable to have particles of a fixed length-to-width ratio as well as of a uniform size distribution. Some of the particulate magnetic materials currently used in recording media are discussed next.

Iron Oxides. The iron oxide γ-Fe_2O_3 (maghemite) was one of the first magnetic materials used for recording applications and is still in wide use today, due to its low cost and physical and chemical stability. Figure W17.10 illustrates a transmission electron micrograph of needle-shaped (acicular) particles of γ-Fe_2O_3. These magnetic particles are typically oriented with their long axis, which in this case is also the easy axis of magnetization due to shape anisotropy, parallel to the surface of the film and also parallel to the direction of the motion of the head along the film. In this longitudinal geometry the magnetic properties are optimized with high M_r and with good magnetic squareness. The lengths of the particles are typically 0.2 to 0.4 μm.

Acicular iron oxide particles are magnetically stable since the shape-induced uniaxial magnetic anisotropy is unaffected by changes in temperature and stress, as opposed

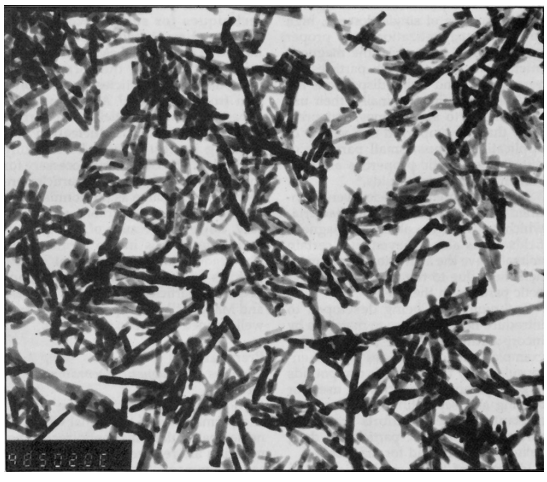

Figure W17.10. Needle-shaped (acicular) particles of γ-Fe_2O_3 (maghemite) used in magnetic recording media are shown in a transmission electron micrograph. The lengths of the particles are 0.2 to 0.4 μm and the aspect ratio is 7:10. (From M. Ozaki, *Mater. Res. Soc. Bull.*, **14**(12), 35 (1989).)

to magnetocrystalline anisotropy, which is often quite sensitive to such changes. The chemical stability of the γ-Fe_2O_3 particles is due in large part to the fact that they are fully oxidized.

The oxide γ-Fe_2O_3 is a ferrimagnet with the cubic inverse spinel crystal structure in which there are vacancies on one-sixth of the normally occupied octahedral Fe^{3+} sites of the Fe_3O_4 inverse spinel crystal structure, described in Section 9.8. The remaining octahedral sites that would normally be occupied by Fe^{2+} in Fe_3O_4 are occupied by Fe^{3+} instead. Due to the partial cancellation of the sublattice magnetizations, the value of $M_{\text{sat}} \approx 400$ kA/m for γ-Fe_2O_3 is well below the corresponding value of 1710 kA/m for pure Fe at $T = 300$ K. The small particles used in recording typically have $M_{\text{sat}} \approx$ 350 kA/m, due to the presence of magnetically inactive surface layers or other defects.

The values of H_c observed for the γ-Fe_2O_3 particles are in the range 24 to 32 kA/m. These are an order of magnitude below the estimate given in Table W17.1 for the case of a magnetic field applied parallel to the long axis of a needle-shaped magnetic particle (i.e., $H_c = H_K \approx N_\perp M_s = 0.5 M_s$). This estimate for H_c corresponds to the reversal of the magnetization by coherent rotation of **M**. In practice the magnetization rotates incoherently (i.e., it begins to reverse direction at much lower fields) due to the fact that the magnetization directions in different parts of the sample do not remain parallel in ways that are influenced by defects or inhomogeneities in the particles.

CrO_2. Needle-shaped particles of the tetragonal transition metal oxide CrO_2 have also found applications in magnetic recording due to their higher coercive fields, in the range 44 to 48 kA/m. The oxide CrO_2 is unique because it is the only transition metal oxide that is ferromagnetic at room temperature. Greater recording densities are possible with CrO_2 since the higher values of H_c make it possible to overcome the effects of the larger demagnetizing fields H_D which occur as the recording density increases. The high coercive fields that are observed result from both the shape and magnetocrystalline anisotropies of the CrO_2 particles.

Iron Oxides Containing Co. The most widely used particulate recording media now employ iron oxide particles whose coercive fields have been enhanced by the addition of cobalt (Co^{2+}). For these cobalt-modified iron oxide particles H_c is typically in the range 32 to 80 kA/m. These materials also allow higher recording densities than do the pure iron oxides discussed earlier. The enhancement of H_c resulting from the addition of Co to the iron oxide structure is due to the increase in the magnetocrystalline anisotropy of the material when Co^{2+} ions experience the octahedral crystal fields of the surrounding O^{2-} ions. Exchange interactions with the next-NN Fe^{3+} ions also contribute to the enhanced anisotropy.

The current practice is to apply Co only to the surfaces of the iron oxide particles. These surface-modified particles show better stability with the Co surface layer enhancing the uniaxial anisotropy and coercive force of the particles.

Metal Particles. Small, needle-shaped particles of ferromagnetic Fe coated with surface oxides for passivation are advantageous for high-density recording because they have higher magnetizations and coercive fields than those of the ferrimagnetic or ferromagnetic oxide particles discussed earlier. While pure Fe has a spontaneous magnetization $M_s = 1710$ kA/m at $T = 300$ K, these Fe particles, which are about 200 nm long and only 20 nm in diameter, have effective values of $M_s \approx$

750–900 kA/m, due to the surface oxides, which can occupy about one-half of the particle volume. These reduced values of M_s are still nearly twice as large as those found for oxide particles. Typical values of H_c are 120 kA/m, also well above the values of H_c for oxide particles. Since the uniaxial magnetic anisotropy of these Fe particles is due to their elongated shape, their coercive fields show little dependence on temperature or stress.

Barium Ferrite. The ferrimagnetic material barium ferrite, $BaO{\cdot}6Fe_2O_3$ ($BaFe_{12}O_{19}$), is unique among recording materials, due to its very high magnetocrystalline anisotropy and hence H_c in the low-symmetry hexagonal *magnetoplumbite* crystal structure. This crystal structure has a unit cell consisting of two formula units and containing two spinel-like regions, each with the formula Fe_6O_8, and two HCP-like regions, each with the formula $BaFe_6O_{11}$, in which an oxygen atom in a close-packed layer is replaced by a Ba^{2+} ion. The crystal structure of $BaFe_{12}O_{19}$ is illustrated in Fig. W17.11, where one half of the hexagonal unit cell is shown. The other half is obtained by a mirror reflection relative to either the top or the bottom plane. The high intrinsic H_c value, 160 to 240 kA/m, of this material is combined, however, with a rather low M_{sat} value of ≈ 300 kA/m. Although barium ferrite particles have the shape of thin hexagonal platelets (Fig. W17.12), the easy direction of magnetization remains along the c axis, which is perpendicular to the plates. This results from the dominance of the magnetocrystalline anisotropy over the shape anisotropy. A perpendicular rather than a longitudinal recording medium results when the barium ferrite platelets are present with their surfaces parallel to the surface of the medium.

The intrinsic coercive field of barium ferrite is actually too high for magnetic recording applications (but not for the permanent-magnet applications discussed earlier), and is usually reduced to ≈ 4 to 10 kA/m by the replacement of some of the Fe^{3+} ions by less magnetic Co^{2+} ions or by nonmagnetic Ti^{4+} ions.

Thin-Film Magnetic Recording Media. In addition to the composite particulate magnetic recording media just described, continuous magnetic thin films are the material of choice for hard-disk applications, due in large part to their potential for higher

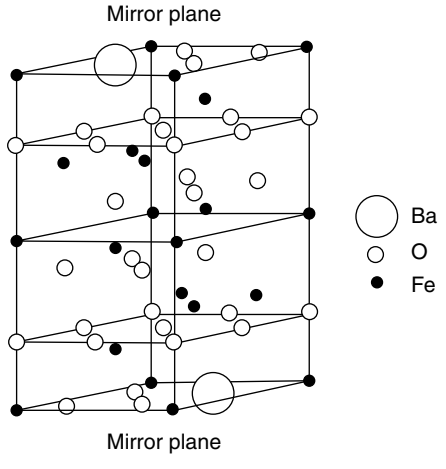

Figure W17.11. Crystal structure of $BaFe_{12}O_{19}$ with one half of the hexagonal unit cell shown.

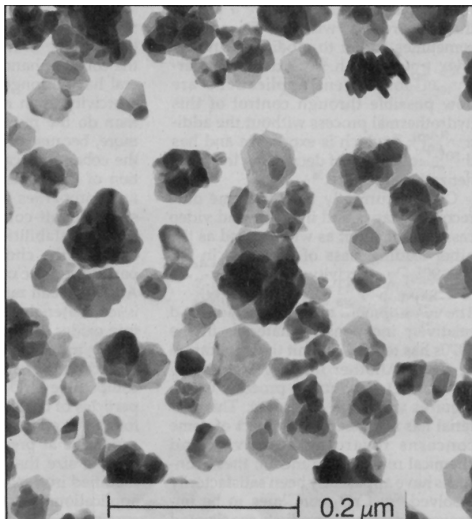

Figure W17.12. Thin platelet-shaped hexagonal particles of barium ferrite, $BaFe_{12}O_{19}$. (From M. P. Sharrock, *Mater. Res. Soc. Bull.*, **15**(3), 53 (1990).)

recording densities than are currently possible in particulate media. The higher densities arise from the higher coercive fields and remanent magnetizations possible in magnetic alloy films. Another advantage is that the magnetic properties of thin films can readily be controlled by varying the composition and the deposition and processing conditions. A significant disadvantage of thin-film media is that they are much less durable than currently used particulate media.

The criteria for continuous thin-film recording media are essentially the same as those for particulate media (i.e., magnetic hardness), with high H_c, high M_r, high coercivity squareness, and low noise. As a result, it is important to control the magnitudes and distributions of the crystalline, shape, and stress anisotropies in thin-film magnetic recording media. Typical thin-film media with thicknesses in the range 10 to 100 nm have values of M_s in the range 5 to 100 kA/m and H_c in the range 40 to 120 kA/m.

The ideal thin-film recording medium should consist of small (10 to 50 nm) magnetically noninteracting crystallites or grains, with as uniform a size distribution as possible. The grains should not be too small or superparamagnetic effects will limit the stability of information storage. The actual magnetic behavior of thin-film recording media can be complicated, as it depends on the interactions between the grains and on the magnetic anisotropy energies, which in turn depend on internal stresses, composition gradients, and properties of the grain boundaries.

The thin films used in longitudinal recording media typically include the ferromagnet Co along with other transition metals, such as Ni, Cr, Ta, Pt, Re, and Zr. A wide range of polycrystalline Co-based alloy films has been prepared via electrochemical deposition and by physical processes such as evaporation and sputtering. A tilted columnar grain structure with strong shape anisotropy is obtained by evaporating the films at an angle of 70° from the normal. The voids that appear between the columnar grains are beneficial because they help to isolate the grains physically and magnetically, thereby reducing noise in the recording. These metal-evaporated tape (MET) media

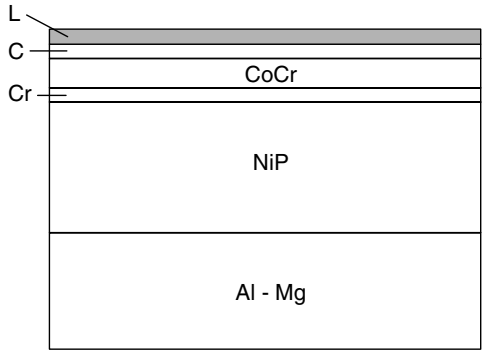

Figure W17.13. Schematic cross section of a magnetic hard disk. Typical thicknesses of the layers are as follows: Al–Mg, 0.6 to 0.8 mm; NiP, 10 μm; Cr, 20 to 100 nm; CoCr, 30 nm; a-C, 10 to 20 nm; L, lubricant, several monolayers. [Adapted from K. E. Johnson et al., *IBM J. Res. Dev.*, **40**, 511 (1996).]

based on Co, CoNi, or CoNiCr can have high coercive fields of 120 kA/m. The wear and corrosion resistance of the films can be enhanced by a surface Co oxide when they are deposited in the presence of oxygen. The desired magnetic isolation of the grains is also improved by the presence of the surface oxide.

The cross section of a typical thin-film magnetic hard disk is illustrated in Fig. W17.13. The mechanical support for the multiple coatings that are utilized is an Al–Mg alloy disk. The disk is plated with an amorphous layer of NiP, which is then textured with grooves to improve the wear characteristics of the disk. The active layer is typically a ferromagnetic film of CoCr containing additional elements, such as Pt and Ta, which control its coercivity. The CoCr-based film consists of magnetic domains that are readily alignable by the applied magnetic field of the write head. It is covered by a protective, hard amorphous carbon (a-C) layer, which in turn is coated with a polymeric lubricant to reduce friction. The CoCr active layer is deposited on an underlayer of Cr, which enhances the deposition of the active layer with high H_c and with its easy axis of magnetization in-plane. The flatness of the outer a-C layer is of paramount importance, since the disk rotates past the read/write head at a speed of about 40 m/s and at a distance of only about 100 nm.

Compositional segregation in the CoCr-based layer can help to minimize intergrain interactions, leading to lower noise. Alloy compositions can be chosen that will undergo a phase change or spinodal decomposition at elevated temperatures to achieve the desired segregation.

Ferromagnetic thin films have also been developed for perpendicular recording applications and have great potential for higher bit densities. Sputtered CoCr alloy films with columnar microstructure can show perpendicular magnetic anisotropy, due to the orientation of the c axis of the grains perpendicular to the plane of the film. The complicated dependencies of the magnetic, structural, and mechanical properties of the films on the deposition conditions present both a considerable challenge and the flexibility needed to prepare films with the characteristics desired. One current approach involves deposition of these Co-based films onto Cr underlying films, which help to enhance the coercive field of the film deposited. This example of the use of surfaces and interfaces to modify the equilibrium bulk properties of magnetic films is typical of

processes that will play an increasingly important role in the continuing development of higher-density, lower-noise magnetic recording media.

W17.10 Details on Magneto-Optical Recording Materials

The magnetic materials currently in use in MO recording media that so far have the best combination of magnetic and MO properties are amorphous alloys of rare earths and transition metals (i.e., RE–TM alloy media) in which the RE ions interact antiferromagnetically with the TM ions. The magnetization of the RE ions dominates at low temperatures, while at higher temperature the magnetization of the TM ions dominates. At an intermediate temperature, known as the *compensation temperature* T_{comp}, the RE and TM magnetizations cancel each other. The temperature T_{comp} can be adjusted by varying the film composition or the deposition and processing conditions.

Examples of amorphous RE–TM alloys include the ternary alloys a-GdTbFe, a-TbFeCo, and a-DyFeCo, which have the required magnetic and MO properties but which have limited chemical stability. Although the source of the perpendicular magnetic anisotropy observed in these amorphous alloy films is not clear, possibilities include stress-induced anisotropy, pair ordering, and single-ion anisotropy. Shape-induced magnetic anistropy in thin films favors an easy axis in the plane of the film (i.e., parallel or longitudinal anisotropy). Typical values of the anisotropy coefficients are $K_u = 10^4$ and 10^5 J/m^3 for the Gd- and Tb-based alloys, respectively.

Figure W17.14 presents a useful summary of the magnetization M_s, coercive field H_c, uniaxial anisotropy coefficient K_u, and Kerr rotation θ_K of an a-$Gd_{24}Tb_1Fe_{75}$ alloy from low temperatures up to its T_C, which is just above 500 K. For this alloy the compensation temperature T_{comp} at which the sublattices of the antiferromagnetically coupled Gd and Fe magnetic moments cancel each other is close to 340 K (i.e., near the typical operating temperature). At T_{comp} the coercive field H_c diverges as $M_s \to 0$ (see Table W17.1). When the magnetization $\mathbf{M}_s$ of a magnetic domain is very low, due

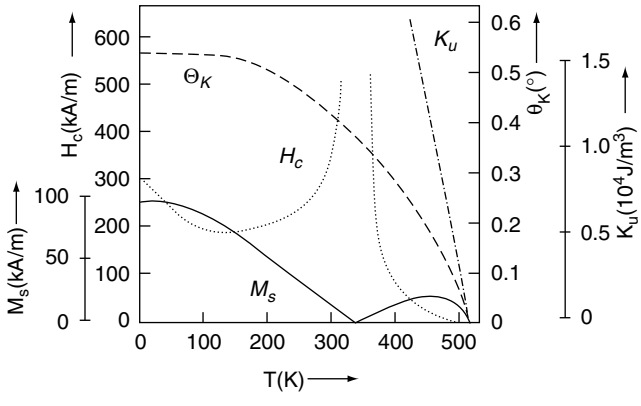

Figure W17.14. Magnetization M_s, coercive field H_c, uniaxial anisotropy coefficient K_u, and Kerr rotation θ_K for an amorphous $Gd_{24}Tb_1Fe_{75}$ alloy from low temperatures up to its T_C. The compensation temperature T_{comp} at which the sublattices of Gd magnetic moments and Fe magnetic moments cancel each other is close to 340 K. (From F. J. A. M. Greidanus and W. B. Zeper, *Mater. Res. Soc. Bull.*, **15**(4), 31 (1990).)

to the compensation effect, very high external fields are required to exert large enough torques to rotate $\mathbf{M}_s$. Thus the H_c required becomes very large in the vicinity of T_{comp}. The Kerr rotation is determined primarily by the Fe spins since the Kerr effect for the RE elements is small.

The intrinsic magnetic properties of these amorphous RE–TM alloys are determined by their compositions and can be controlled by varying the Fe/Co ratio in a-TbFeCo alloys and the Gd/Fe ratio in a-GdTbFe alloys. Film microstructure also plays a critical role in these alloys and is determined by the deposition and processing conditions. The absence of grain boundaries aids in the reduction of noise. The main difficulty with amorphous RE–TM films is their lack of chemical stability.

Promising MO materials for future applications include oxides such as ferrites and garnets and Co/Pt multilayers, all of which can have good chemical stability. In the Co/Pt multilayers the perpendicular magnetic anisotropy may arise from interactions at the interfaces between the Co and the Pt layers.

W17.11 Details on Fe Alloys and Electrical Steels

Pure Fe and Fe–Ni Alloys. The magnetic properties of pure Fe are discussed first as the classic example of a magnetically soft material. As Fe is treated to remove impurities such as C, N, O, and S (typically, by heating in H_2 or in H_2 and H_2O), the permeability μ increases dramatically, H_c decreases steadily, and M_s is hardly affected. In addition, the hysteresis loop narrows considerably and eddy current and other magnetic losses due to irreversible processes are reduced. This behavior is illustrated in Table W17.4 for two grades of Fe and reflects the fact that M_s is an intrinsic property, while μ and H_c are extrinsic, depending on microstructure, impurity content, and so on. Since the impurities listed earlier have limited solubilities in Fe, ≈ 0.01 at %, they tend to form inclusions or precipitates such as Fe_3C, Fe_4N, FeO, and FeS. These precipitates, if present, impede or pin the motion of domain walls. Their elimination thus allows domain walls to move more readily.

TABLE W17.4 Magnetic Properties of Pure Fe and Some Magnetically Soft Fe Alloys and Electrical Steels at Room Temperature

Alloy[a]	μ_r(max)[b]	H_c (A/m)	M_s (10^3 kA/m)
"Pure" α-Fe ($\approx$99%)	$\approx 10^3$	80	1.71
Pure α-Fe ($\approx$99.99%)	2×10^5	0.8	1.71
78 Permalloy (78Ni, 22Fe)	$\approx 10^5$	4	0.86
Supermalloy (79Ni, 16Fe, 5Mo)	$\approx 10^6$	0.16	0.63
Mumetal (77Ni, 18Fe, 5Cu)	2.4×10^5	2	$\approx$0.5
Hipernik (50Ni, 50Fe)	7×10^4	4	1.27
Silicon-iron (97Fe, 3Si) (oriented)	4×10^4	8	1.6
Amorphous $Fe_{80}B_{11}Si_9$	—	2	1.27

Source: Data for $Fe_{80}B_{11}Si_9$ from N. Cristofaro, *Mater. Res. Soc. Bull.*, May 1998, p. 50; remaining data from A. Chikazumi, *Physics of Magnetism*, Wiley, New York, 1964, p. 494.

[a]The compositions of the alloys are given in weight percent unless otherwise stated.

[b]The maximum relative magnetic permeability μ_r(max) is expressed here in units of $\mu_0 = 4\pi \times 10^{-7}$ N/A^2 and corresponds to the maximum value of B/H on the hysteresis loop in the first quadrant taken in increasing field.

Purified Fe can be considered to be one of the very high permeability soft magnetic materials, even though its magnetic anisotropy and magnetostriction are both nonzero. Drawbacks to the widespread use of pure Fe are its relatively low resistivity $\rho \approx 10^{-7}$ Ω·m, a problem when eddy current losses are important, and the expense associated with purification and with other treatments, such as careful annealing to relieve strain. Corrosion of pure Fe is another well-known problem. Fe-based magnetic alloys such as Fe–Ni, Fe–Co, and Fe–Si can have even better properties than those of pure Fe and are also less expensive to produce, being less sensitive than pure Fe to the level of impurities.

The reason that "pure" BCC α-Fe is so sensitive to impurities and defects is related primarily to the fact that its intrinsic magnetocrystalline anisotropy coefficient K_1 and magnetostriction λ are both nonzero, with $K_1 > 0$ and $\lambda_{100} > 0$. By alloying BCC α-Fe with FCC Ni, which has K_1 and λ_{100} both < 0, solid-solution FCC Fe–Ni alloys with compositions near 78 wt % Ni can be produced that have intrinsic magnetic anisotropies and magnetostrictions which are much smaller than found in either of the pure metals. The alloy with 78 wt % Ni is known as 78 Permalloy and is used when maximum permeability is desired. When high values of M_s are more important, the content of Fe atoms with larger magnetic moments ($2.2\mu_B$ versus $0.6\mu_B$ for Ni) must be higher, so 45 to 50 wt % Ni alloys are often used. Examples include 45 Permalloy with 45 wt % Ni and Hypernik with 50 wt % Ni (see Table W17.4).

The advantage of very low magnetocrystalline anisotropy for obtaining magnetically soft materials is that for $K \approx 0$ the domain wall thickness δ is much larger than the typical size of any defect [see Eq. (17.6)]. In this case the interactions of defects such as precipitates or inclusions with domain walls is much weaker, so the effects of pinning are greatly decreased. Low magnetic anisotropy can thus help to minimize the effects of structural imperfections.

The useful FCC Fe–Ni alloys with Ni concentrations greater than 30 wt % have magnetic properties that are usually very sensitive to thermal and mechanical processing treatments and to the presence of impurities. They are ordinarily annealed at high temperatures, above $T = 900$ to 1000°C, and then cooled rapidly to avoid the occurrence of long-range chemical ordering (e.g., formation of the $FeNi_3$ phase). The problem associated with ordering is that the magnetocrystalline anisotropy in the ordered $FeNi_3$ phase is much higher than in the disordered alloys. The disordered FCC phase which is desired can also be retained by the addition of a few at % of transition metal impurities, such as Cu, Cr, or Mo.

Alloys with special properties can be obtained by the addition of elements such as Cu and Mo to Fe–Ni. The alloy Supermalloy, which is obtained by adding Mo to Fe–Ni, corresponds to 79 wt % Ni, 16 wt % Fe, and 5 wt % Mo. Supermalloy has a much higher initial permeability, lower electrical resistivity, and requires simpler heat treatment than do the permalloys. A very useful alloy for magnetic shielding is Mumetal, typically 77 wt % Ni, 18 wt % Fe, and 5 wt % Cu. One of the advantages of adding Cu to Fe–Ni is the increased capability for mechanical working of the resulting alloys.

The 35 at % Ni FCC Fe–Ni alloy known as Invar, with $T_C \approx 250$ to 300°C, has an extremely low thermal expansion coefficient α at room temperature, $\approx 10^{-6}$ K^{-1}, an order of magnitude below the values of α for either pure Ni or pure Fe. This "*Invar anomaly*" associated with a low value for α apparently results from cancellation of the usually positive lattice thermal expansion by a negative magnetostrictive

strain contribution resulting from decrease of the spontaneous magnetization M_s in the temperature range just below T_C. Above T_C the thermal expansion increases to normal values in the paramagnetic state where the magnetostriction is small.

At the same time that the Invar anomaly or effect occurs, an anomaly in the spontaneous volume magnetostriction $\Delta V/V$ is also observed in these alloys. It is believed that a magnetic moment–volume instability may play an important role in the Invar effect. It has been predicted that in FCC γ-Fe there can exist two different ferromagnetic states, one a high-spin state with large magnetic moment and large volume and another a low-spin state with low magnetic moment and low volume. In Invar the energy separation between the high spin–high volume state and the low spin–low volume state lying at higher energy is not large, and therefore the low spin-low volume state is thermally accessible. In this way a negative magnetic contribution to the normally positive thermal expansion can appear.

A wide variety of 3*d* transition metal alloys show Invar-type behavior.[†] They have found important applications due to their dimensional stability, including in precision instruments, springs, glass-to-metal seals, and bimetallic applications. Alloys with exceptional elastic stability (e.g., the Fe–Ni alloys known as Elinvar with 40 to 45 at % Ni), find applications in springs, electronic instruments, tuning forks, and so on. Additional elements such as Be, Mn, Mo, Si, and Se are often added to these alloys for hardening purposes and to prevent aging effects.

Fe-Co alloys are also of interest as soft magnetic materials, with useful materials including Permendur (2% V–FeCo) and Hiperco (65Fe, 35Co). In Permendur, vanadium is added to the equiatomic FeCo alloy to increase the resistivity and the ease of fabrication, both of which are low in FeCo, due to the tendency for an order–disorder transition to occur as this alloy is cooled or even quenched. Hiperco has the highest M_s in the alloy series, as can be seen in Fig. 17.17.

Fe–Si Alloys. Although the Fe–Ni alloys just discussed can be prepared with a wide range of magnetic, mechanical, and thermal properties suitable for many applications, Fe-Si alloys are often used in their place — primarily for economic and not physical reasons. The addition of 1 to 4 wt % Si to Fe leads to desired increases in the permeability, the electrical resistivity, and the stability of the magnetic properties as well as a decrease in the coercive field. Drawbacks to the use of Si as an alloying element in Fe include a decrease in the magnetization, essentially a dilution effect associated with the addition of a nonmagnetic element, and an increase in brittleness. The primary benefit related to the addition of Si is the reduction of eddy current losses.

The preferred Fe–Si alloys contain only 1 to 4 wt % Si since alloys having higher Si contents are too brittle to be worked into the desired sheet form. Improved magnetic properties in these low-Si-content alloys can be achieved by the proper mechanical and thermal treatment. Hot rolling and annealing can be used to obtain a desired mechanical texture in polycrystalline sheets. When the resulting texture is (110) [001] [i.e., having the (110) plane parallel to the surface of the sheet with the grains having their [001] directions preferentially aligned parallel to each other], the grain-oriented sheets can be more readily magnetized into a uniform state. This is possible because the [001] direction corresponds to one of the easy axes of magnetization in α-Fe. The oriented

[†] For a useful recent review of Invar, see E. F. Wassermann, Chapter 3 in K. H. J. Buschow and E. P. Wohlfarth, eds., *Ferromagnetic Materials*, North-Holland, Amsterdam, 1990.

Fe-Si alloy thus obtained has magnetic properties which are much superior to those of an unoriented alloy.

The 6.4 wt % Si alloy actually has superior magnetic and electrical properties compared to the alloys with lower Si contents. The problem with brittleness at this high Si content can be overcome if additional Si can be incorporated into an existing 3 wt % Si sheet which requires no further mechanical treatments. This can be accomplished by deposition of Si onto the surface of the sheet followed by thermal treatments to diffuse and disperse the surface layer of Si into the bulk.

A metallic glass based on Fe and containing both Si and B (i.e., a-$Fe_{80}B_{11}Si_9$) has lower losses and a lower H_c than grain-oriented Fe-3.2 wt % Si steel. Even though the amorphous metal has a lower T_C than the Fe–Si alloy, 665 K as compared to 1019 K, its thermal stability is sufficient for many applications in electrical equipment. The lower losses in a-$Fe_{80}B_{11}Si_9$ are due to its higher electrical resistivity and lower H_c. The lower H_c results from the disordered structure and the resulting lack of defects such as grain boundaries and dislocations that would impede the magnetization and demagnetization processes through the pinning of domain walls.

W17.12 Details on Materials for Read/Write Heads

Magnetic materials that are currently in use in recording heads include the Fe–Ni alloys known as permalloys, Sendust (an Fe–Al–Si alloy), Mn–Zn ferrites, amorphous alloys, and, most recently, thin films in the form of magnetic multilayers or superlattices. The use of the magnetic multilayers is based on the recently discovered giant magnetoresistance effect discussed in Section W17.4.

The permalloys, discussed earlier for their applications in electromagnetic devices, are Fe–Ni alloys that have low magnetic anisotropy and low magnetostriction, both of which contribute to the high permeabilities observed. The permalloy $Fe_{19}Ni_{81}$ is the most widely used material for inductive heads. In addition, $Fe_{19}Ni_{81}$ shows a magnetoresistive effect of about 4%. Susceptibility to corrosion and high wear rates are limitations of the permalloys.

The Fe–Si–Al alloy known as Sendust, with approximately 85 wt % Fe, 10 wt % Si, and 5 wt % Al, has K_1 and λ both equal to zero and, as a result, can be prepared with $\mu_{\max} = 1.2 \times 10^5 \mu_0$. This alloy is very brittle and its fabrication into useful forms involves the use of compressed powders.

Mn–Zn ferrites (i.e., $Mn_{1-x}Zn_xFe_2O_4$ with $0.25 < x < 0.5$) are insulating and have the high mechanical hardness necessary for applications as head materials. Since they are ferrimagnetic, they have relatively low values of M_s. The addition of Zn to $MnFe_2O_4$ lowers T_C, which actually results in higher values of the permeability at room temperature. Adding Zn from $x = 0$ up to 0.5 also leads to an increase in M_s. This results from the fact that $ZnFe_2O_4$ is a normal spinel, while $MnFe_2O_4$ is the more usual inverse spinel. Therefore, the added Zn atoms displace Fe^{3+} ions from the tetrahedral to the octahedral sites that were formerly occupied by the now-missing Mn^{2+} ions. As a result, complete cancellation of the spins of the Fe^{3+} ions in octahedral sites by the oppositely directed Fe^{3+} spins in tetrahedral sites no longer occurs and M_s increases. Due to their high permeability and insulating properties, $Mn_{0.5}Zn_{0.5}Fe_2O_4$ ferrites are also used in transformers and inductors.

Magnetic multilayers have recently been incorporated into magnetic read-head structures since they exhibit sensitivities to magnetic fields of 100 to 1000 A/m (i.e., a few